UNIVERSIDAD DE INVESTIGACIÓN DE TECNOLOGÍA EXPERIMENTAL YACHAY

Escuela de Ciencias Físicas y Nanotecnología

TÍTULO: Interphase analysis of viscous flow in porous media to enhance oil recovery

Trabajo de integración curricular presentado como requisito para la obtención del título de Físico

Autor:

Dalena Romina León Fon Fay

Tutor:

PhD. Ernesto Medina Dagger

Co - Tutor:

PhD. Camilo Zamora

Urcuquí, abril 2021

SECRETARÍA GENERAL
(Vicerrectorado Académico/Cancillería)
ESCUELA DE CIENCIAS FÍSICAS Y NANOTECNOLOGÍA
CARRERA DE FÍSICA
ACTA DE DEFENSA No. UITEY-PHY-2021-00011-AD

A los 10 días del mes de junio de 2021, a las 16:00 horas, de manera virtual mediante videoconferencia, y ante el Tribunal Calificador, integrado por los docentes:

Presidente Tribunal de Defensa	Dr. COSENZA MICELI, MARIO GIUSEPPE , Ph.D.
Miembro No Tutor	Dr. RAMIREZ VELASQUEZ JOSE MANUEL , Ph.D.
Tutor	Dr. MEDINA DAGGER, ERNESTO ANTONIO , Ph.D.

El(la) señor(ita) estudiante **LEON FONFAY, DALENA ROMINA**, con cédula de identidad No. **1205976879**, de la **ESCUELA DE CIENCIAS FÍSICAS Y NANOTECNOLOGÍA**, de la Carrera de **FÍSICA**, aprobada por el Consejo de Educación Superior (CES), mediante Resolución **RPC-SO-39-No.456-2014**, realiza a través de videoconferencia, la sustentación de su trabajo de titulación denominado: **Interphase analysis of viscous flow in porous media to enhance oil recovery**, previa a la obtención del título de **FÍSICO/A**.

El citado trabajo de titulación, fue debidamente aprobado por el(los) docente(s):

Tutor	Dr. MEDINA DAGGER, ERNESTO ANTONIO , Ph.D.

Y recibió las observaciones de los otros miembros del Tribunal Calificador, las mismas que han sido incorporadas por el(la) estudiante.

Previamente cumplidos los requisitos legales y reglamentarios, el trabajo de titulación fue sustentado por el(la) estudiante y examinado por los miembros del Tribunal Calificador. Escuchada la sustentación del trabajo de titulación a través de videoconferencia, que integró la exposición de el(la) estudiante sobre el contenido de la misma y las preguntas formuladas por los miembros del Tribunal, se califica la sustentación del trabajo de titulación con las siguientes calificaciones:

Tipo	Docente	Calificación
Miembro Tribunal De Defensa	Dr. RAMIREZ VELASQUEZ JOSE MANUEL , Ph.D.	10,0
Presidente Tribunal De Defensa	Dr. COSENZA MICELI, MARIO GIUSEPPE , Ph.D.	10,0
Tutor	Dr. MEDINA DAGGER, ERNESTO ANTONIO , Ph.D.	10,0

Lo que da un promedio de: **10 (Diez punto Cero)**, sobre 10 (diez), equivalente a: **APROBADO**

Para constancia de lo actuado, firman los miembros del Tribunal Calificador, el/la estudiante y el/la secretario ad-hoc.

Certifico que *en cumplimiento del Decreto Ejecutivo 1017 de 16 de marzo de 2020, la defensa de trabajo de titulación (o examen de grado modalidad teórico práctica) se realizó vía virtual, por lo que las firmas de los miembros del Tribunal de Defensa de Grado, constan en forma digital.*

LEON FONFAY, DALENA ROMINA
Estudiante

Dr. COSENZA MICELI, MARIO GIUSEPPE , Ph.D.
Presidente Tribunal de Defensa

Firmado electrónicamente por:
MARIO GIUSEPPE COSENZA MICELI

Dr. MEDINA DAGGER, ERNESTO ANTONIO , Ph.D.
Tutor

Firmado electrónicamente por:
ERNESTO ANTONIO MEDINA DAGGER

Dr. RAMIREZ VELASQUEZ JOSE MANUEL , Ph.D.
Miembro No Tutor

CIFUENTES TAFUR, EVELYN CAROLINA
Secretario Ad-hoc

AUTORÍA

Yo, **DALENA ROMINA LEÓN FON FAY**, con cédula de identidad 1205976879, declaro que las ideas, juicios, valoraciones, interpretaciones, consultas bibliográficas, definiciones y conceptualizaciones expuestas en el presente trabajo; así cómo, los procedimientos y herramientas utilizadas en la investigación, son de absoluta responsabilidad de el/la autora (a) del trabajo de integración curricular. Así mismo, me acojo a los reglamentos internos de la Universidad de Investigación de Tecnología Experimental Yachay.

Urcuquí, abril 2021.

_____
Dalena Romina León Fon Fay
CI: 1205976879

AUTORIZACIÓN DE PUBLICACIÓN

Yo, **DALENA ROMINA LEÓN FON FAY,** con cédula de identidad 1205976879, cedo a la Universidad de Tecnología Experimental Yachay, los derechos de publicación de la presente obra, sin que deba haber un reconocimiento económico por este concepto. Declaro además que el texto del presente trabajo de titulación no podrá ser cedido a ninguna empresa editorial para su publicación u otros fines, sin contar previamente con la autorización escrita de la Universidad.

Asimismo, autorizo a la Universidad que realice la digitalización y publicación de este trabajo de integración curricular en el repositorio virtual, de conformidad a lo dispuesto en el Art. 144 de la Ley Orgánica de Educación Superior

Urcuquí, abril 2021.

_____
Dalena Romina León Fon Fay
CI: 1205976879

Dedication

To my family and friends.

To my family, that in despite of not understanding the purpose of my career, have always supported me. This goes to my parents, that taught me to be perseverant, to be willing to improve myself, to be kind, and work hard to reach my dreams.

To my friends, that made me enjoy every day at Yachay. To Katy, Kimi, Mishu and Yoshi. You were the best roommates, thank you for all the support, the laughs, the tears. To Romi and Emy, for all the days of study, for all the victories, and all the tragedies. To Daniel, for all the moments. This thesis goes to all you that were a primordial part of my life through all these years, for all the memories we have had, and all the time we have spent. Thank you all for being there.

Acknowledgement

More than a research work, this thesis is a compendium of all the steps I have gone through my life at Yachay Tech. I am so grateful to each of the professors that formed me as a scientist. To all of those who made me belief in myself and let me realize that there are no limits to reach your dreams. I owe an special acknowledgement to Juan Lobos, professor and friend that guided me through my first steps in science. Also, to my advisor Ernesto Medina, who has guided me along this process. His guidance made this research thesis possible, given that at Yachay Tech we do not study fluid dynamics, but he was willing to support me in a totally unknown field for me.

I owe this thesis to all of those to have gave me the opportunity to grow as a scientist. Thanks to Professor Chil-Min Kim, from my stance at DGIST, who trusted on the capacities of a girl from a third world country to work on a highly technological research laboratory. To Professor Cladio Falcón from University of Chile, who taught me that working on fluid dynamics is not easy, but the excitement of understanding it is worthless.

To all of those who have made me who I am now, thank you.

Resumen

La inestabilidad de Saffman-Taylor es un problema de gran relevancia en la industria petrolera. Este problema aparece cuando un fluido menos viscoso desplaza a uno más viscoso, como proceso de extracción de petróleo por inyección de agua. Esta inestabilidad da como resultado el desarrollo de estructuras de dedos en el frente de desplazamiento. Estas estructuras disminuyen la eficiencia de la recuperación de petróleo, lo que genera pérdidas económicas y de recursos. Este trabajo de investigación tiene como objetivo establecer los fundamentos teóricos, experimentales y computacionales para abrir una nueva línea de investigación en la Universidad Yachay Tech. Esta línea de investigación tiene como propósito estudiar el comportamiento fluidodinámico de los procesos de extracción de petróleo para proponer métodos de estabilización que permitan mejorar la recuperación de hidrocarburos.

A través de medios teóricos se desarrolló un criterio de estabilidad cuasi-2D. Para complementar el estudio, se revisa la correspondencia del ancho del dedo con el parámetro de control de estabilidad, y el tiempo de inestabilidad característico. Adicionalmente, se discute una breve propuesta de la derivación de un criterio de estabilidad basado en el efecto tridimensional de la curvatura transversal de la interfaz.

Se construyó un montaje experimental para visualizar los patrones desplazamiento en una celda de Hele-Shaw. Los experimentos realizados fueron los puntos de referencia para analizar la eficiencia de los criterios de estabilidad propuestos y desarrollar un modelo computacional en COMSOL Multiphysics que reproduzca los resultados experimentales.

Al unir los tres enfoques, los experimentos y el modelo computacional mostraron una buena concordancia y consistencia, con algunas diferencias en los umbrales de estabilidad. Los experimentos tienden a alcanzar inestabilidades más rápidamente que las simulaciones debido a las contribuciones de la curvatura transversal de la interfaz y otros efectos físicos ignorados en las simulaciones. El criterio de estabilidad resultó ser preciso para predecir el comportamiento de la interacción entre fluidos que departan estrictamente de interfaces planas.

Palabras clave: Saffman-Taylor, COMSOL Multiphysics, criterio de estabilidad.

Abstract

The Saffman-Taylor instability is a problem of high relevance in the oil industry. This problem shows up when a less viscous fluid displaces a more viscous one, like in the water-flooding stage of the oil extraction process. This instability leads to finger structures in the displacement front. These structures decrease the efficiency of oil recovery, leading to economical and resource losses. This research work aims to address the theoretical, experimental and computational foundations to open a new research line at Yachay Tech University. This research line has as purpose to study the fluid dynamical behavior of oil extraction processes to propose stabilization methods that allow to enhance oil recovery.

Through theoretical means, a quasi-2D stability criteria is developed. To complement the theoretical study, it is analysed the finger width correspondence to the surface tension parameter, and the characteristic instability time. Additionally, it is discussed a brief proposal of the derivation of a stability criteria based on effect of the 3D contribution of the interface's transverse curvature.

An experimental set-up was built to visualize the flow patterns of interacting fluids in a Hele-Shaw cell. The experiments performed were the reference points to analyse the efficiency of the stability criteria proposed, and to develop a computational model in COMSOL Multiphysics that reproduces the experimental results.

Joining the three approaches, the experiments and the computational model showed good agreement and consistency, with some differences in stability thresholds. The experiments tend to reach instabilities faster than the simulations due to the contributions of the transverse curvature of the interface and other physical effects neglected in the simulations. The stability criteria turned out to be accurate in predicting fluid behavior of flows that depart strictly from flat interfaces.

Key words: Saffman-Taylor, COMSOL Multiphysics, stability criteria.

Contents

List of Figures

List of Tables

Chapter 1

Introduction

When talking about interface analysis, we implicitly introduce the well-known two-phase flow in physics. This phenomenon is of scientific and technological relevance due to its applications in many fields of study[2]. It can occur in chemical, biological and industrial processes[2], just to mention a few. This work is focused on water-flooding processes in oil recovery. The goal of this procedure is to extract a relatively large portion of the oil trapped in the reservoirs once the natural pressure can no longer drain it from the ground. The problem with injecting water to displace oil relates to the ensuing instabilities, mainly due to high viscosity ratios that lead to finger structures in the displacing front, and the interaction between water/rock that causes oil trapping due to wetting effects[3]. Our study will focus on viscous finger formation, which is a critical limiting factor to enhanced oil recovery[3]. As a consequence of these instabilities there is poor sweep efficiency caused by physical interactions in the interface[3]. Our aim is to set up a model test system to assess control strategies for these instabilities in order to improve oil recovery. That way, oil reservoirs can be exploited more fully and efficiently, bearing in mind environmental issues[4].

The importance of this study is emphasized by the use of hydrocarbons and their limited availability as a non-renewable resource. Petroleum has shown to be a cheap and energy rich source of fuel for most kinds of transportation. Many highly useful derivatives are also obtained from oil[5]. Indeed, oil has become an essential natural resource to keep our current standard of living. Unfortunately, it is a non-renewable

natural resource (at least for our lifetime) meaning that it has a time limit for us to count on it. According to British Petroleum (BP) there are 1.65 trillion barrels of proven oil reserves on the planet, which at our current rate of consumption represents around 47 years[6]. Because of the complex porous structure and the displacement instabilities in the recovery process, using the existing methods, only an average of 30% of the oil can be extracted[3]. By stabilizing the displacement front, up to a 20% more oil can be acquired[3]. This, in consequence, would lengthen the useful life of oil reservoirs and increase the amount of oil available for our use.

Interface stabilization studies began around the 60s, when the boom of nuclear boiling water reactors (BWR) appeared as new efficient energy source[2]. It is ironic that when new renewable energy systems emerged, scientist also began to research ways to improve oil extraction. This is mainly due to the high costs related to transition from hydrocarbon based fuel to renewable energies, and the oscillation of the oil prices[7]. Even nowadays, it is still a challenge to move completely to renewable energies. The Institute of Energy Research (IER) points out that for the United States the costs of transition to a 100% renewable electric system ranges from 4.5 trillion to 5.4 trillion dollars[8]. In fact, it is known that the cost of energy production related to fossil fuels is higher than the cost of most of the renewable sources[9], but given that fossil fuels dominate the market, as technology is adapted to that energy source, it is hard to adapt our current way of living to alternate energies. Furthermore, the importance of oil does not only consist on its function as raw material for fuel production, but it also has an important role in derived products like asphalt, petrochemical feedstocks (plastic, wax, cosmetics, textiles...), lubricating oils, etc[5]. Around 13% of the oil extracted in The USA is used to produce petrochemical feedstocks, and the other 87% is used to produce fuel (gasoline, Diesel, jet fuel)[5]. In the same way, in Canada the 21% of oil extracted is used in the production of asphalt and petrochemicals, while the rest of its production is used to generate fuel[10]. Hence, even though fuel is the major component derived from crude oil, the other products have also a high impact in our daily lives. This means that even if we move to an energetic system that does not depend on crude oil, there is a large amount of products, that we use very commonly, that depend on petroleum, reason for why it is important to keep looking for ways to increase its availability.

This work focuses on the stage of oil extraction involving water injection. In the petroleum industry,

there are usually three stages. The first stage stands for natural depletion, the second stage stands for water-flooding, pressure maintenance or gas injection, and the third stage implies the use of miscible gases, chemicals or thermal processes[11]. According to Green *et al.*[11], nowadays water-flooding is synonymous to a secondary process, given that it is the most common procedure present in the extraction process. This kind of processes lead to several instabilities. We will focus on the Saffman-Taylor instability which corresponds to the formation of finger structures as a consequence of the viscosity difference between a less viscous fluid displacing and more viscous one[12]. The problem with instabilities is that "under unstable operation conditions, the efficiency of a two-phase systems can rapidly decrease" (Ruspini, 2013)[13]. In oil extraction, this lack of sweep efficiency directly affects the recovery rate, leading to an economical impact. Many proposals to solve the problem have converged on the use of more viscous fluids to extract oil, but it turns out to be economically unfavorable[11]. Other stabilization techniques include studies related to the pore distribution[14], addition a lubricating layer[15], addition of surfactants and polymers to water[3], flow geometry control by variable channel thickness[16], electric field interaction[17], structured porous media[18] and many other alternatives.

Experimental tests to assess strategies to control unstable two-phase flow can be time consuming and expensive, reason for why it is advantageous to count on analytical and computational tools[13]. Our study includes a dimensional analysis, a theoretical analysis based on Bensimon's *et al.*[12] review about Saffman's work in a quasi-2D system[19], a 3D extension of the analysis in 2D[12], a discussion of the finger width in relation to a stability parameter proposed by McLean and Saffman[20] and the discussion of the critical time that it takes for the instabilities to appear. The dominant parameter to study in this research is the surface tension parameter. A dimensionless parameter derived from Darcy's law that establishes the required relations between the variables that influence the stability of the front[12]. This parameter determines the conditions at which the system is stable or unstable, allowing to look for a stability map. Experimental and computational approaches are introduced to compare with our theoretical discussions. The computational model is meant to coincide with the experimental results. If so, it can be used in future researches to predict behaviors before constructing a proposed experimental set-up. Using the obtained structures through computational and experimental models, we analyse the finger patterns in relation to the

finger width and stability region proposed. Also, we discuss the importance of three-dimensional physical effects like wettability and transverse front curvature, that should be considered to obtain more accurate results in the computational model and the stability criteria.

The main objective of this research is to determine a stability criteria and develop a computational model to predict fluid behavior in a Hele-Shaw cell. Once that we are able to design the experimental set-up to generate the desired perturbations in our displacement front, we can proceed, in future work, to study the behavior of the system in order to stabilize it. There is a large set of research proposals that can be derived from the results of our analysis. Some of the proposals include the stabilization of viscous fingering using nano-particles to increase the viscosity of the displacing fluid, studying the behavior of viscous fluids interacting with a defined shape of porous media, introduction of time dependent velocity patterns to analyze the role of accelerated input in the finger onset and shape, analysis of the stability of the system under actual 3D considerations, among others.

This thesis project is meant to be the basis for a new research field at Yachay Tech University. Basically, we will set the theoretical foundations that determine the stable/unstable conditions of the system, and evidence it through experimental and computational approaches. This will allow other researchers to join the project and develop further advances that contribute to the oil industry in Ecuador.

1.1 Problem Statement

Petroleum is a limited resource that powers most of our transportation system and provide daily life products derivatives. It is necessary to improve the recovery process to extend its availability. In oil recovery processes the goal is to extract as much oil as possible from the reservoirs. Given that the water-flooding stage implies the immiscible interaction between water and oil, poor sweep efficiency and thus low recovery rates are expected because of the viscosity ratio between fluids. The behavior of the system can change according to the flow conditions and fluid properties. A stability criteria allow to define regions where the initial conditions of the system could lead to a stable or unstable behavior in despite of the viscosity ratio.

The reservoir engineer is confronted with the problem of stabilizing the displacement front by modifying the properties of the displacing fluid and the interface. In this research we identify and play with the possible variables that directly influence the stability of the system. Through theoretical means like the Raleigh algorithm (dimensional analysis) we determine a dimensionless parameter in terms of these variables, so that we can define stabilization regions. A low-cost micro-model injection system built at Yachay Tech University allows to actually evidence the instabilities proposed theoretically. Following the literature, the main variables to address are viscosity, surface tension, cell width, cell depth, and input velocity among other rheological properties of the two fluid system[12].

Because of the COVID-19 pandemic, the development of the experimental set-up has been limited. In order to propose new micro-models to assess more accurate experimental instabilities, we rely on computational simulations of the fluid flow using the CFD module of COMSOL Multiphysics. The whole research is meant to define the regions of stability/instability to control the behavior of a system. Once the basic tools for instability analysis are set, this project opens the opportunity for a new research field to emerge in Ecuador in order to improve the oil extraction system.

1.2 General and Specific Objectives

The general objective is to settle a stability criteria to predict the behavior of a quasi-2D two-phase flow of a less viscous fluid pushing a more viscous one. In order to achieve it, our specific objectives are:

- Develop a theoretical stability analysis based on Darcy's law. Analyze which parameters affect the stabilization of the system.

- Determine stability regions according to a dimensionless control/stabilization parameter.

- Complement the theoretical analysis by studying the finger width and characteristic time expected for the Saffman - Taylor instabilities.

- Build an experimental set-up to visualize the displacement patterns and compare them with the ones proposed by the theoretical analysis.

- Build simulations in COMSOL Multiphysics. Reproduce the experimental set-up in order to build a predictive computational model.

- Confirm the accuracy of the stability criteria by comparing the results of the theoretical, experimental and computational approaches.

1.3   Outline of the thesis

In order to accomplish our goals, the thesis will be divided into seven chapters. The first two chapters (this one and the one that follows) are considered to be the introductory part. Here, the main concepts and problems are explained. Chapters 3 - 5 correspond to the methods used to perform our studies, beginning by a theoretical analysis and complementing it with experimental-computational approaches that verifies the proposed behavior. The last chapters review the results obtained and a meticulous discussion. We end with the conclusions and discuss future work that can be undertaken based on our work.

- Chapter 1 (**Introduction**): This chapter introduces the problem of viscous flows instabilities and the purpose of this research thesis to deal with these problems.

- Chapter 2 (**Theoretical Background**): This chapter reviews the necessary concepts to understand the physics behind a two - phase flow fluid, its interaction with a porous media, the instabilities produced in this kind of systems, and the main methods of enhanced oil recovery.

- Chapter 3 (**Theoretical Stability Analysis**): This chapter shows the detailed description, derivation and discussion of the parameters proposed to study the stability of the system. This includes a dimensional analysis based on Rayleigh algorithm, the study of the surface tension parameter through quasi-2D and 3D approaches, finger width relation to surface tension parameter, and instability characteristic time.

- Chapter 4 (**Experimental Stability Analysis**): This Chapter exposes the construction, operation and specifications of the experimental set-up. It includes an overview of the pumping system, the

micro-model cells where the experiments are carried out, data acquirement, and an insight of relation between the experiments and the stability maps developed from the theoretical analysis.

- Chapter 5 (**Computational Model**): In this chapter we see a description of the Software used to develop the simulations (COMSOL Multiphysics), a brief introduction of the modules used, and a description of the conditions and parameters established to replicate the experimental model.

- Chapter 6 (**Analysis and Results**): This chapter provides general results of the experiments/simulations in relation to the theory.

- Chapter 7 (**Conclusions & Outlook**): In this chapter, a summary of the result is provided. Also an outlook to future works that can be derived from this research.

Chapter 2

Theoretical Framework

This chapter contains a complete overview of the concepts required to understand the research project. Here we presented basic insights on how immiscible fluids interact, define a porous medium, and the influence of the porous medium on the two fluid system. A description of enhanced oil recovery in terms of water - oil interplay, and a review of previous works that have contributed to the development of this topic.

2.1   Two-phase flow systems

The study of two-phase flow began around the 50's, given to its possible relevance to biological systems, enhanced oil recovery, boilers, nuclear reactors, condensers, air conditioning systems, refrigeration equipment, desalination plants, and many others[2]. Two-phase flow implies any interaction between fluids in any state of matter: gas, liquid or solid. Some of the most common interactions are gas-liquid, liquid-liquid, gas-solid, solid - liquid[21]. Depending on the type of interaction, different behaviors at the interfaces arise. The interactions can be grouped between miscible or immiscible interfaces. The miscible fluids mix at any proportion forming a homogeneous solution[22]. Instead, immiscible fluids do not mix by definition, and a strong boundary (interface) is created between them[22]. These terms are normally used to describe liquids

interacting, but both cases can actually occur in any phase interaction. For example water-sugar (liquid - solid)[23], CO_2 - crude oil (gas - liquid)[24] are miscible fluids and they do not have to be necessarily liquids. Also solid-solid interactions with Rayleigh-Taylor instabilities occur, making features of the earth's mantle in geology[25].

Classical fluid flows are described by Navier-Stokes Equation (NSE):

$$\mu\nabla^2\mathbf{v} = \rho\left(\frac{\partial\mathbf{v}}{\partial t} + \mathbf{v}\cdot\nabla\mathbf{v}\right) + \nabla P - \rho\mathbf{g}, \tag{2.1}$$

where μ is the viscosity of the fluid, $\mathbf{v}$ is the velocity vector field, $\mathbf{P}$ is the pressure, ρ is the density, and $\mathbf{g}$ is gravity. This equation is a form of Newton's second law $\mathbf{F}$= m $\mathbf{a}$. It is presented in units of Force per unit volume. The driving force of this equation is given by the pressure gradient and acceleration[26]. The term between parenthesis is a representation of the total acceleration, and the left hand side is the dragging force due to viscosity[26]. This equation relates the pressure and the three coordinate velocities, and needs to be complemented with the continuity equation to fulfill the mass and energy conservation equations[26].

2.1.1 Immiscible fluid flow

Two interacting immiscible fluids do not mix. They can be classified in *disperse* and *separate* flows. The former corresponds to flows in which one of the fluids behaves as if it were particles, like bubbles, droplets, dispersed in a second fluid[27]. On the other hand, the latter flow considers the study of streams of different fluids separated by a well defined interface between them. What allows two fluids to be immiscible is the surface tension[28]. This parameter can be explained in terms of inter-molecular forces. In the bulk of a liquid, the force on a molecule is the same in all directions. On the other hand, at the interface, the molecules are attracted to the centre of the fluid[29]. Hence, the surface tension not only accounts for separating distinct fluids, but also for the rounded shape at the interfaces defining a radius of curvature. Also, when two immiscible fluids are in contact, a pressure jump across the interface is generated due to the surface tension[3].

In oil recovery water-flooding is an immiscible process. Oil and water do not mix, enabling water to

push on the oil thanks to the effect of surface tension. Some other industrial uses include disperse flows, liquid extraction processes and co-extrusion flows[21]. In disperse flows, droplets are commonly used. A droplet is a bubble shaped fluid flowing within another fluid, forming emulsions important in drug delivery and bio-sensing[30]. In liquid extraction, the immiscible property of two fluids can be used to separate a solute dissolved in one of the fluids by contact of the interacting fluids[21]. In the polymer industry it is required to maintain superior mechanical properties. The co-extrusion principle is to inject immiscible layers of polymers in a mold to obtain a material with specific properties[31]. The task in these flows is to keep a stable interface[21].

2.1.2   Two - phase immiscible viscous flow interactions in porous media

In a porous medium, the interaction between two viscous fluids is complex since it becomes a fully *multiphase* flow[32]. There is a solid - liquid and liquid-liquid interactions, which adds several effects to the behavior of the flow at pore and reservoir scale. At the pore-scale, physical phenomena like wetting films, wetting behavior, contact angles, capillarity, slip or no-slip conditions on the walls, trapping, among others show up due to the interaction of fluids with the rock[32 3]. Actually, at microscopical scales there is always a degree of slip close to the surface, but it can be neglected on a large scale continuum description. According to M. Blunt (2017)[26], the pressure drop across a pore is insignificant in comparison to the one of the whole reservoir, so that a constant density can be surmised (even for gases). Nevertheless, the physics at the pore scale cannot always be ignored since the fluid-rock interaction is responsible of oil trapping caused by interfacial effects[3].

From a macroscopic point of view (i.e. the reservoir) the poor oil sweep is related to "permeability heterogeneity, channeling or thief, fracture zones, and a viscous ratio" (Alvarado & Manrique, 2010)[3].

Darcy's law is used to consider the effects of flow in a porous media from a macroscopic point of view or continuum description. This relation is derived from Navier-Stokes equation using the following assumptions:

- In an average porous media, there is no turbulent flow. Thus fluid flow occurs at low Reynolds

number[a], that leads to the suppression of the inertial term $\mathbf{v} \cdot \nabla \mathbf{v}$[26][32].

- Constant density along the reservoir[26].

- The fluids to consider are in-compressible viscous liquids, then the divergence of the velocity in NSE vanishes and the Laplacian of pressure is zero[12].

- The tangential and normal components of the fluid velocity with respect to the rigid solid walls are also zero[26]. This is called a no-slip condition.

- Permeability is the parameter that relates Fluid velocity $\mathbf{v}$ with the driving forces $(\nabla P(x, y) - \rho_i\, g)$

$$\mathbf{v}(x, y) = -\frac{K_i}{\mu_i}\left[\nabla P(x, y) - \rho_i\, g\right] \tag{2.2}$$

It is important to remark that $\mathbf{v}$ is not an actual velocity, but it is called *Darcy velocity*. It is a volume average (or coarse graining) of the flow field. According to Blunt, "it is not a real velocity, but the volume of fluid flowing per unit area of the porous medium (and this area includes both solid and void)" (Blunt, 2017)[26]. This equation allows to introduce the interaction of the porous media with the fluid by permeability K_i. At reservoir scales, this parameter is associated to instabilities caused by channeling or thief zones, fracture networks, viscous ratio[3]. Permeability is defined as the "volume of a fluid of unit viscosity passing through a unit cross section of the medium in unit time under the action of a unit pressure gradient" (Wool, 2005)[33]. In other words, it is the property of a material to let a fluid pass through it.

To replicate studies of a flow in porous media, the opaque property of the system is a drawback. Hence, most of the studies are carried on a Hele-Shaw cell: An experimental set-up conformed by two transparent parallel plates of length **L** separated by a negligible distance **b**[32]. Even though a Hele-Shaw cell has three dimensions, the thickness of separation is very small compared to the other cell dimensions and thus can be neglected (quasi-two dimensional system). The cell is not exaclty a porous media, but has an associated permeability given by $K_i = b^2/\mu$. The analogue of a porous media by a Hele-Shaw cell is

---

[a]Reynolds number: ratio between inertial and viscous forces in the flow[26]. Re<2300: laminar flow, Re>4000: turbulent flow

a good approximation, but it is not very accurate for immiscible flows[32] and neglects wetting effects[20]. Recalling the extra physical contributions that the porous structure adds to the fluid interaction (contact angles, trapping, rock wetting, etc), a Hele-Shaw cell can not replicate them either[32].

Porous media

In order to have a deeper understanding of the behavior of a liquid within a porous media, it is important to know the basic physical elements that affect its motion. A porous medium is a material with voids in its volume. Depending on the packing and material of the matrix, it has different properties that will affect macroscopically and microscopically to a fluid moving through it. The most important macroscopic properties of porous materials are the porosity, permeability and displacement capillary pressure[34].

- Porosity "is the fraction of the bulk volume of the porous sample that is occupied by pore or void space" (Dullien, 1991), so that it says how much void space there is in the sample for the fluid to be in.

- Capillary pressure refers to the pressure difference between two interacting phases, which is needed for one phase to push other[26].

A porous media can be described in terms of the pores themselves and throats, as seen in Fig.2.1. The pores constitute the main void spaces, and the throats are the connections between them. When a fluid is present, we can operationally define throats and pores by the fact that the capillary pressure, is a local maximum at throats, given that they are "the smallest regions of the pore space with the smallest radii of curvature" (Blunt, 2017)[26]. On the other hand the capillary pressure is a local minimum at the center of the pores.

2.1.3   Instabilities

In this section, we will briefly review the possible instabilities that could appear in a two phase flow within a porous media. The main instability we consider are the Saffman-Taylor instability, snap-off and
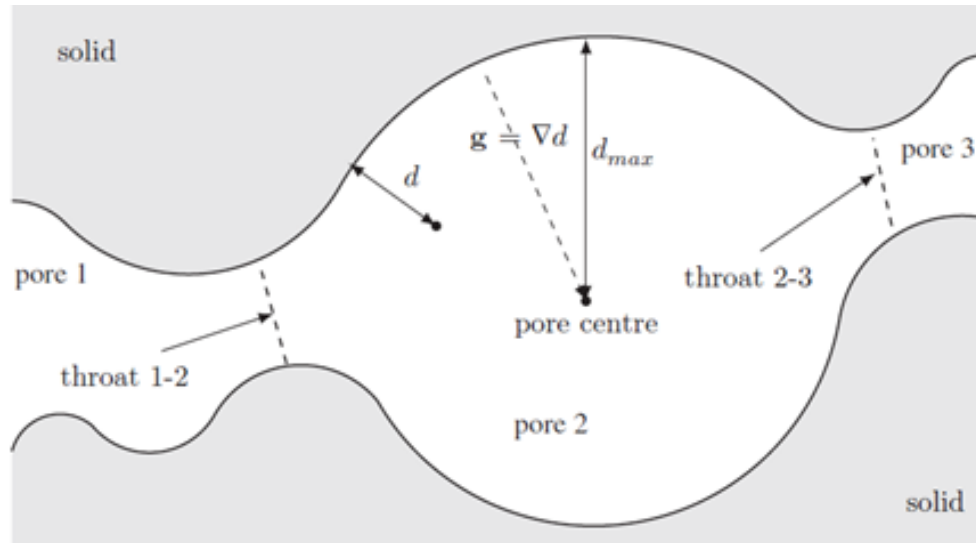
Figure 2.1: Pore Structure (Blunt, 2017)[26]

channeling. The Saffman-Taylor instability also known as viscous fingering is the one that we will focus in this research.

Saffmann – Taylor instability

The Saffman-Taylor instability was first described in a Hele-Shaw cell[12], shown in Fig 2.2. Viscosity is the property of fluids that indicates the resistance to flow. The higher the viscosity, the harder it is for a fluid to flow[35]. It plays a fundamental role in this study. When working with immiscible fluids, the viscous contrast between the displacing and the displaced liquid is the source of the instability. At the interface, a surface tension exists that describes the border between both fluids[12]. With a low surface tension, a less viscous fluid, acting as the displacing one, can break into the other (the displaced one) due to its facility to move, as compared to the more viscous one. If the fluids exchange roles, a fluid with higher viscosity has a higher resistance to move than a less viscous one, so that the more viscous will not break into the displaced one and no instability occurs. In general high viscosity of the displacing fluid and high surface tension allows to have stability in the displacement front, while otherwise a less viscous fluid breaks into

the displaced one creating growing fingering patterns in the front .

This behavior can also be explained in terms of the mobility ratio or viscosity ratio. Let the viscosity of displaced fluid be μ_d and the viscosity of the injected fluid μ_i. The mobility ratio would be $M = \mu_d/\mu_i$. The front will be stable (flat interface) for M<1, given that the injected fluid is more viscous and has a higher pressure drop than the displaced one, leading to the suppression of any perturbation growth[26]. The opposite case M>1 is unstable given that the pressure drop at the injected fluid is less than the displaced one, meaning that any perturbation will grow because the injected fluid will move faster than the more viscous fluid that surrounds it[26].
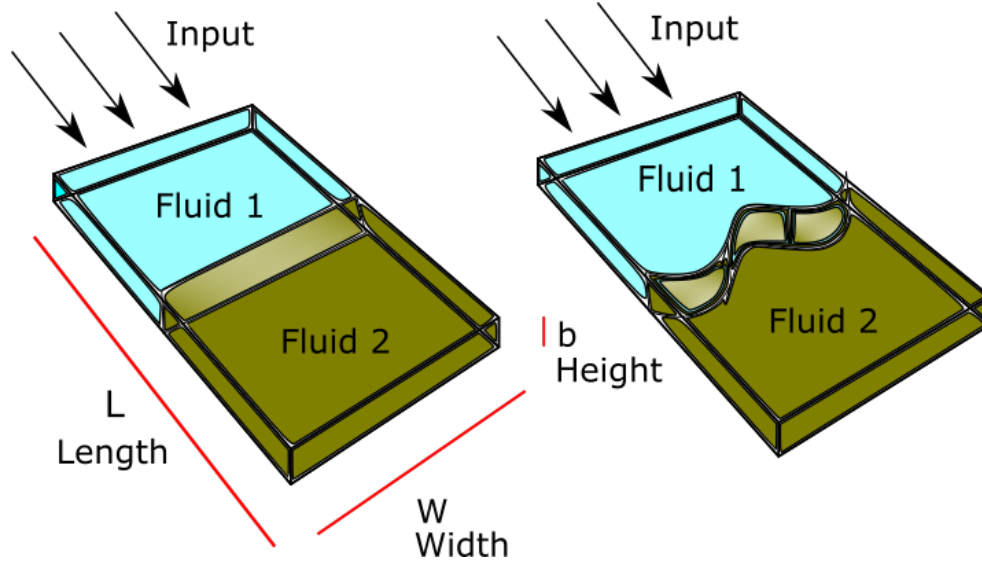
Figure 2.2: Stable / unstable fluid flow. The displacement on the left has a flat interface, meaning that it is stable (M>1). The displacement on the right has a perturbed interface (M<1).

The perturbation of the flat interface leads to finger-like structures. We will see ahead that there are several levels of instability for these systems. The first instability corresponds to the growth of a single finger given by the pressure difference along the interface[32]. Recalling the fact that the interface gets a curvature due to surface tension, the pressure difference is the one that makes this round structure displace and grow towards the more viscous fluid[32]. This process is called *shielding*. Depending on the conditions

of the system, the more unstable it gets, the thinner the finger becomes. In most of the studies, the ratio between the finger width and the cell width converges at $\lambda \rightarrow 1/2$ [19] [20] [12]. This is the limit at which we can evidence a single finger, from that point ahead, the finger does not get thinner anymore, but starts *splitting* at the tip [32]. The physical explanation for this instability was given by Bensimon (1986) [12]: "...(the instability)... lies in the geometry of the moving interface". For a fixed pressure difference along a channel, the larger gradients in pressure appear at the end of the largest perturbations, making them move faster with respect to the other points at the interface. In that way, "the entire system is destabilized by the motion" (Bensimon, 1986) [12].

The stability of the system can be characterized in terms of the capillary number or the surface tension parameter, both very similar. There is actually no concrete description of the stability/control parameter [12], but the most general one is the capillary number [32]. The first parameter mentioned is dimensionless and act as a control parameter [12]. The second parameter is the relative contribution between viscous and capillary forces [21] and plays a critical role in the stability of a two phase flow immiscible system. The single finger-like structures are the first level of instability, for relatively small capillary numbers [36]. In here, surface tension plays an important role that prevents or stabilize smaller perturbations to grow [36]. Then, in a more unstabilized system, as capillary number grows and surface tension is not enough to stabilize the system, splitting begins to occur in a periodic manner, this is called a *dendritic finger*. Finally, a much more unstabilized system where capillary number is really high, and the mobility ratio is too low, the instability is such that a finger is not even able to grow, but there is just a "continuous joining and merging of finger branches leads to no distinct finger formation" (Guan, 2003) [36], these structures are known as *coalescent fingers*. The behaviors described can be evidenced in Fig 2.3.
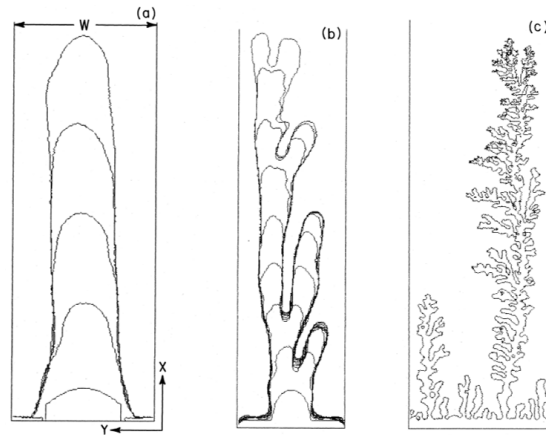
Figure 2.3: Unstable modes observed in random walk simulations, from Liang (1986)[37]. Time evolution seen from bottom to top. a) A finger-like structure b) Dendritic fingers c) Coalescent fingers[12]

Oil trapping

Two main situations of interest can occur as trapping; in the first one, there is swelling snap-off, and in the second case we have bypass phase trapping.

Oil trapping or snap-off refers to the residues of oil trapped within water in the reservoir after the primary drainage. Basically, due to wettability and capillary effects, a blob of oil is left enclosed by water at a pore[3]. According to Alvarado (2010)[3], wettability is the "relative ability of one fluid to wet a solid surface (pore surface) in the presence of a second one". This property next to capillary pressure and surface tension governs oil snap-off. As mentioned previously, the curvature of the interface is created because of surface tension and capillary pressure. The curved interface interacting with the pore structure through wetting effects make the displacing fluid to adhere to the walls of the pore, advancing and trapping oil inside[3], as seen in Fig 2.4. In the interaction between fluids, depending on which one has higher wettability to the pore, there will be a different distribution of the fluids in the matrix. "The type of wettability controls the distribution of fluids within the rock pore space and framework" (Schön, 2015)[38]. So that depending on the material of the pore structure, the system can be water-wet, oil-wet or intermediate. In a water-wet system, water coats the rocks and oil occupies the central position at the pores. In oil-wet systems, the

roles of oil and water are exchanged[38].
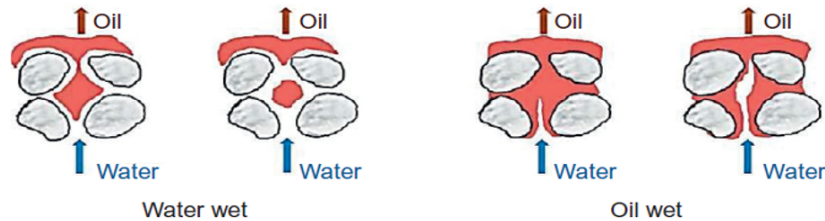
Figure 2.4: "Wettability types: oil displacing in water and oil-wet reservoirs during water-flooding" Schön, (2015)[38].

In contrast to the stabilization of viscous fingers, snap - off can be stabilized by adding surfactants to water in order to reduce surface tension and capillary number[3]. If surface tension is smaller, the curvature of the interface will be less, decreasing the wettability of displacing fluid.

In bypass phase trapping it is preferable to talk about wetting or non-wetting phases. In presence of a solid phase, one of the immiscible fluids interacting has higher attraction to the walls, that one is the wetting phase[11]. In a bypass or alternate pathway in a porous network, the wetting phase tends to invade first smaller pores due to higher capillary pressure, then leaving the larger pathway filled with the non-wetting phase (oil), trapping it in the bypass[39]. This phenomena can be evidenced at Fig. 2.5.

Figure 2.5: Imbibition process with trapping in the thicker throat. Kantzas, (n.d.)[39].

2.2 Enhanced oil recovery

The oil recovery process can be reduced into three main phases: primary recovery/natural depletion, secondary recovery/pressure maintenance, tertiary recovery/enhanced oil recovery (EOR)[3][11]. A brief description of these stages: The first one refers to the drilling of a well that reaches the reservoir and allows

the natural energy to extract oil without external work[3]. This natural energies could be solution gas drive, natural water drive, fluid and rock expansion, and gravity drainage[11]. Once the natural processes in the reservoir are not strong enough to support oil production, the second stage is reached and the operator must inject a liquid or gas to increase the pressure in the reservoir and drain it further. The use of immiscible gases in the second stage used to be more popular in earlier times, nowadays water-flooding is the most common procedure due to higher sweep efficiency[11]. According to V. Alvarado (2010), in the first two stages a maximum recovery of 30-40% of the total content can be achieved[3]. Green (2018) also reports a recovery efficiency of 35-50% in the first two stages[11]. The final stage, EOR, finally arrives where various strategies are implemented to boost oil extraction and enlarge the lifetime of a reservoir.

The EOR methods commonly used are chemical injection, solvent injection and thermal injection. The enhancement of oil production by these procedures will allow an increase in recovery up to a 20% more[11]. All these procedures are basically fluid injection under different conditions. In general, EOR stands for methods that allow the increase of the sweep efficiency of the in-place fluid[3]. As will be seen below, this improved recovery can be achieved by increasing the mobility ratio between injected and in-place fluids or reducing the capillary and interfacial forces in order to reduce oil saturation in soil[3].

Green (2018)[11] defines a classification of EOR processes in 5 categories: mobility control, chemical, miscible, thermal, and others.

- Mobility - control: The aim is to increase the mobility ratio, such that polymers are used to thicken water, or foams are used to reduce the mobility of gas[11]. Usually, in a water-flooding process there is an unfavorable mobility ratio that leads to water fingers crossing across the oil reservoir as seen in Fig. 2.6. Polymer - water-flooding improves the recovery given that the mobility of the polymer solution is less than the one from water[11] as evidenced in Fig. 2.6. This process mainly enhances the macroscopic sweep rather than microscopic at the pore scale.

- Chemical: It implies the use of surfactants or alkaline agents to reduce the interfacial tension to displace oil. In some cases, chemical processes are also considered mobility control processes, due to the change in mobility that the chemicals produce. Depending on the reservoir, sometimes it is

required to increase surface tension to avoid fingers formation, but in other cases it is necessary to decrease surface tension to displace oil blobs produced by trapping[11].

- Miscible: The injection of fluids that are miscible to oil like CO_2. A miscible section replacing a clear interface leads to the mobility of oil drops caused by trapping.

- Thermal: Injection or generation of thermal energy to the system. For example injecting steam or oxygen combustion at the reservoir. This process enhances the efficiency by provoking viscosity reduction, oil swelling and steam stripping. The disadvantage of this method is that the heated fluid is less dense than oil and water, so it moves to the top of the reservoir, ignoring a large part of oil in the reservoir[11].
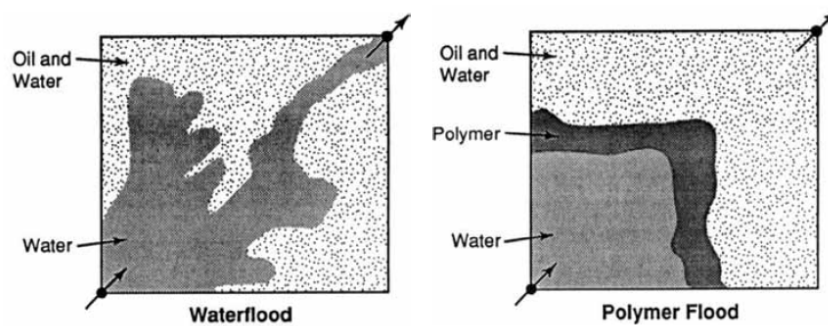
Figure 2.6:   Water-flooding process and polymer injection to water-flooding.

Chapter 3

Theoretical Stability Analysis

This project involves the study of fluid dynamical systems. Specifically, we are dealing with a displacement instability that changes over time. In this chapter we will compile some analysis based on Darcy's law to study the time development of a perturbation in a quasi two-dimensional interface.

Stability theory addresses the solutions of differential equations and of trajectories of dynamical systems under small perturbations given an initial condition[40]. A simple wavelength dependent perturbation is imposed on an otherwise flat interface and a solvable linear equation reflects whether the perturbation grows or decays. The analysis can be applied to non-linear differential equations to which we don't know the solutions and we are not concerned with the long time behavior. Once one has the onset of the instability, it is assumed that the behavior continues into a non-linear regime.

Here we begin by a dimensional analysis based on Buckingham theorem aiming to find a simplified expression of all the variables that could affect to the stability of the system. As a consequence, it is obtained a control parameter that simplifies the study of this phenomena. Then, it is discussed the study of the two dimensional flow in a Hele-Shaw cell, based on the control parameter derived by Bensimon *et al.*[12]. Following, it is derived the finger width correspondence to the stability parameter based on the research work of McLean and Saffman[20]. Later, it is derived and discussed the characteristic time of the instabilities. These studies provide the opportunity to understand and predict the behavior of the system

and compare them with the studies developed by computational and experimental models. There is an additional study that will not be contrasted experimentally, but will allow to provide further predictions of the stability of the systems. This is the study of the behavior of the three dimensional case and the assessment of its impact on the Hele-Shaw cell results.

3.1   Dimensional analysis for stabilization criteria

The equations of motion for fluids are non-linear and full analytical solutions, especially in the dynamical regime, are difficult to come by[41]. The crux of dimensional analysis is to identify the important dimensional quantities involved in the phenomenon. This is a mix between trial and error, and intuition. To perform dimensional analysis we will use the Rayleigh algorithm and Buckingham π theorem[42] to build the important dimensionless control parameter.

These methods allow to reduce the number of variables to study. The Rayleigh's Algorithm is used to find a dimensionless expression out of the model's variables[42]. The Buckingham Pi Theorem uses the Rayleigh algorithm to set groups of new dimensionless variables in terms of the original ones[42].

Theorem 1. Let $q_1, q_2, q_3...q_n$ be the main variables inter-related by a set of equations. These can be related into a single function of the form

$$F(q_1, q_2, q_3...q_n) = 0 \quad \text{or equivalently} \quad q_1 = f(q_2, ..., q_n)$$

Let k be the number of fundamental dimensions, and n be the number of variables. Then $j = (n - k)$ are the number of dimensionless variables or Π groups that will describe a reduced functional compact form:

$$\Phi(\Pi_1, \Pi_2, \Pi_3...\Pi_{n-k}) = 0 \quad \text{or equivalently} \quad \Pi_1 = \phi(\Pi_2, ..., \Pi_{n-k})$$

The set of parameters obtained is not unique, but what matters is that they form a complete and independent set[43].

3.1.1 Derivation of dimensionless parameter

Darcy's equation governs fluid flow under a pressure gradient or gravitational field in a system with Darcy velocity $v(x, y)$, permeability K_i, fluid viscosity μ_i, pressure $P(x, y)$, density ρ_i, and gravity g.

$$v(x, y) = -\frac{K_i}{\mu_i} \left[\nabla P(x, y) - \rho_i \, g \right].$$

(3.1)

In our studies we will not consider gravity, given that we will work in a horizontal displacement, then

$$
\begin{aligned}
v(x, y) &= -\frac{K_i}{\mu_i} \left[\nabla P(x, y) \right], \\
&= -\frac{b^2}{12\mu_i} \left[\nabla P(x, y) \right],
\end{aligned}
$$

(3.2)

where we have used the well known result $K_i = b^2/12$ for a cell of depth $b << W$, the channel width. First of all, we must set our main variables in terms of the fundamental units [M,L,T], which stand for mass, length and time respectively. Beginning by the pressure, which can be expressed in terms of the interfacial tension τ over length (we will consider τ to be surface tension to avoid confusions with time T) , we get

$$
\begin{aligned}
[P] &= \frac{M}{LT^2}, \\
&= \frac{[\tau]}{L},
\end{aligned}
$$

(3.3)

$$[\tau] = \frac{M}{T^2},$$

(3.4)

$$\left[b^2 \right] = L^2,$$

(3.5)

$$[v(x, y)] = \frac{L}{T},$$

(3.6)

$$[\mu] = \frac{M}{TL}, \tag{3.7}$$

where the square brackets denote the dimensions of the arguments. Darcy's law in terms of its fundamental units would go as follows, and given that the left hand side and the right hand side should agree in their dimensions, it follows that can follow that

$$\frac{L}{T} = \frac{L^2}{M/TL}\frac{1}{L}\frac{M}{LT^2}. \tag{3.8}$$

Now, using the Rayleigh algorithm and the Buckingham theorem we will find the appropriate relation for the variables involved in the stability of the system. Here we add a variable that is not included among the previous ones, but also affects to the stability of the system, the width, W, of the channel where the fluid goes through. Also, lets replace the velocity v by U. Power law dependencies to be found determine combinations of dimensionless quantities obeying

$$W^\alpha b^\beta \tau^\gamma \mu^\delta U^t = C. \tag{3.9}$$

The fact that we are stating the equality between power of our variables and a constant, sets the condition for the dimensionless property. Now, replacing our variables with their corresponding fundamental units, lets find out the powers required to fulfill this property.

$$L^\alpha L^\beta \left(\frac{M}{T^2}\right)^\gamma \left(\frac{M}{TL}\right)^\delta \left(\frac{L}{T}\right)^\epsilon = C' \tag{3.10}$$

The constant C is required to be dimensionless, thus on the right hand side, the sum of the exponents of

T, L, M should be zero, leading to the following set of equations

$$
\begin{cases}
L : \alpha + \beta + \epsilon - \delta = 0, \\
M : \gamma + \delta = 0, \\
T : -2\gamma - \delta - \epsilon = 0,
\end{cases}
\tag{3.11}
$$

so

$$
\begin{cases}
\gamma = -\epsilon = -\delta, \\
\alpha = -\beta.
\end{cases}
\tag{3.12}
$$

Now, simplifying we arrive at

$$
W^{-\beta} b^{\beta} \left(\frac{\tau}{\mu U} \right)^{\gamma} = C.
\tag{3.13}
$$

It is evident that we have a product of two dimensionless terms, these are the Π terms described previously in the Buckingham theorem

$$
\left(\frac{b}{W} \right)^{\beta} \left(\frac{\tau}{\mu U} \right)^{\gamma} = C,
\tag{3.14}
$$

or

$$
\left(\frac{b}{W} \right)^{\beta/\gamma} \left(\frac{\tau}{\mu U} \right) = C'.
\tag{3.15}
$$

Finally, we see dimensional analysis cannot give us the ratio β/γ, so we have a family of combinations of the dimensionless quantities. Below we will see that the controlling dimensionless combination corresponds to $\beta/\gamma = 2$. We thus have an already have a compact dimensionless expression that will allow us to study analytically the behavior of the system controlled by Darcy's law in a Hele-Shaw configuration.

$$
\left(\frac{b}{W} \right)^{2} \left(\frac{\tau}{\mu U} \right) = C'.
\tag{3.16}
$$

3.1.2 Discussion

The parameter obtained provides an idea of the appropriate form that a relation that contains the possible variables that affect the stability of the system. The first term in the left hand side is know as *aspect ratio*, while the second term is the *capillary number*. This means that in general, the most summarized relation of the instability of the system depends on these two parameters. It is good that now there is an idea of the form that stabilization criteria should have, save for numerical prefactors[42]. Thus, using this constant, we will try to find a more explicit relation for the instability in the upcoming sections.

3.2 Stability analysis of 2D perturbed interface

A topical review by Bensimon et al.[12], introduces the study of the Saffman-Taylor instability in a Hele-Shaw cell. The review contains experiments, computational simulation and a theoretical analysis of a two dimensional framework. The study of this system by way of stability analysis will be our major interest in this section, so that we can guide our study to find the most suitable parameters to understand viscous fingers. With Darcy's law and pressure jump equation, Saffman and Taylor derived an expression to find the parameters that directly contribute to the growth or reduction of a perturbation. It turns out that this expression coincides with the expression derived by dimensional analysis in section 3.1. It also provides a numerical value for the ranges of stability in terms of the control parameter.

Stability analysis begins by considering a flat interface exposed to a small perturbation A(t) of a certain wavelength. These perturbations can lead to finger structures that can grow or be damped. Hence, the analysis consist on finding the interplay between relevant physical parameters that govern the evolution of the interface.

3.2.1 Perturbation of the flat interface

Consider a 2D (x,y) flat interface located along y, where the fluids displace in x direction at a velocity U, where *t* is time.

$$x(y) = Ut, \tag{3.17}$$

A small perturbation or deviation from flatness A(t) →0 is introduced in the displacement

$$x(y) = Ut + A(t)\cos(qy), \tag{3.18}$$

where q is the wavenumber of the perturbation imposed in the y direction. In absence of the perturbation A(t), the velocity of the fluid motion is produced by a pressure gradient $\frac{U}{b^2/12\mu}$ as can be derived from Eq. 3.1. By Darcy's law, the following expression is obtained, where the displacement front is $(x - Ut)$,

$$P(x, y) = P_0 - \frac{U}{(b^2/12\mu)}(x - Ut), \tag{3.19}$$

where P_0 is an integration constant with dimensions of pressure. Thus, we can add a perturbation term to this expression, due to the deviation from flatness $A(t)$

$$P(x, y) = P_0 - \frac{U}{(b^2/12\mu)}(x - Ut) + B(x, t)\cos qy, \tag{3.20}$$

where $B(x, t)$ will be found self consistently. A small parenthesis regarding to the shape of $B(x, t)$ must be done here. Remember that we are working with incompressible fluids, so that pressure follows Laplace's equation. For an incompressible fluid $\nabla^2 P = 0$[12]. This means that the special solution of $B(x,t)$ must vary as e^{qx} or e^{-qx}. Note this implies that length scales for x, y behavior is dominated by $1/q$. Obviously, as the pressure values are finite and values of x are positive, so that as $x \to \infty$, the first proposed solution is discarded. The last expression is then

$$P(x, y) = P_0 - \frac{U}{b^2/12\mu}(x - Ut) + B(t)e^{-qx}\cos qy, \tag{3.21}$$

meaning that

$$\nabla P(x, y) = -\frac{U}{b^2/12\mu} - B(t)qe^{-qx}\cos qy. \tag{3.22}$$

The wavenumber q can be conveniently defined as $q = \frac{2\pi n}{W}$, in terms of the width of the cell W. Differentiating the equation of position over time, we obtain an expression for interface velocity with a small perturbation

$$U_n = U + \dot{A}(t)\cos qy. \tag{3.23}$$

Now, by expanding the pressure gradient equation 3.22 and inserting it into Darcy's law, we obtain

$$U_n = U + \frac{b^2}{12\mu}qB(t)\cos qy. \tag{3.24}$$

Later, stating an equality between Eq. 3.23 and Eq. 3.24, an expression to relate both perturbation coefficients $A(t)$ and $B(t)$ is obtained.

$$\dot{A}(t) = B(t)\frac{b^2}{12\mu}q \quad \rightarrow \quad B(t) = \dot{A}(t)\frac{12\mu}{qb^2} \tag{3.25}$$

Bensimon *et al.* actually aim to obtain a full description of $\dot{A}(t)$, to state which parameters are the ones that affect the perturbation the most. Departing from Eq. 3.20, an equation for pressure jump can be obtained in terms of coefficients A and B, by replacing x(y) (Eq. 3.18) into it

$$\Delta P(y) = \left(\frac{U}{b^2/12\mu}A - B\right)\cos qy. \tag{3.26}$$

Pressure jump $\Delta P(y)$ follows classical Gibbs-Thompson equations[12]. The use of the following expression is tricky given that it is specifically for 2D frameworks. Another relation for the pressure jump across the interface is given by

$$\Delta P(y) = -\tau\kappa \approx -\tau\frac{d^2}{dy^2}x(y) \tag{3.27}$$

$$\Delta P(y) = -\tau Aq^2\cos qy, \tag{3.28}$$

where τ is the surface tension at the interface, and κ is the curvature experienced at that specific *(x,y)* position and we have used Eq.3.18. Finally, relating Eq. 3.26 and 3.28, and replacing $B(t)$ (Eq. 3.25) into this relation, we obtain the expression that enables us to talk about the stability of the perturbation of the interface is finally obtained.

$$\left(\frac{U}{b^2/12\mu}A - B\right)\cos qy = -TAq^2 \cos qy, \tag{3.29}$$

$$\left(\frac{U}{b^2/12\mu}A - \left[\dot{A}(t)\frac{12\mu}{qb^2}\right]\right)\cos qy = -TAq^2 \cos qy. \tag{3.30}$$

Finally, algebraically rearranging the terms, we get the description of $\dot{A}$ in terms of the basic parameters that will affect the stability of the system. It that tells us how $A(t)$ changes for short time scales in the linear regime depending on the sign of the quantity in parenthesis. For positive values, the perturbation grows, for negative values, the perturbation is damped or not allowed to grow.

$$\dot{A} = A\left(\frac{U}{b^2/12\mu} - Tq^2\right)\frac{b^2}{12\mu}q, \tag{3.31}$$

3.2.2 Derivation of surface tension parameter d_0

The rate of change of the perturbation from a flat interface provides the stabilization coefficient d_0, mostly known as the *surface tension parameter*. According to equation 3.18, A is the perturbation's amplitude from the flat interface. Hence, for $\dot{A} > 0$ the perturbation increases, while for $\dot{A} < 0$ the perturbation decreases. In the description of equation 3.31, the terms responsible for the sign of the equation is between the parenthesis. From here, the dimensionless parameter d_0 is obtained after some algebraic operations. Using the parameter found by dimensional analysis in section 3.1, we will try to obtain the stabilization criteria looking for the shape of the parameter described previously.

Lets begin by setting the condition for instability:

$$\left(\frac{U}{b^2/12\mu} - \tau q^2\right) > 0. \tag{3.32}$$

substituting $q = \frac{2\pi n}{W}$ we arrive at

$$\left(\frac{U}{b^2/12\mu} - \tau \left(\frac{2\pi n}{W} \right)^2 \right) > 0. \tag{3.33}$$

Multiplying by unity $12\mu U/12\mu U$ and rearranging the terms we get

$$\left(\frac{3W^2 U\mu - Tb^2 n^2 \pi^2}{3W^2 U\mu} \right) \frac{12\mu U}{b^2} > 0. \tag{3.34}$$

It is easy to see two terms, the left one will turn into 1, and the right term will define d_0

$$\left(1 - d_0 n^2 \right) \frac{12\mu U}{b^2} > 0, \tag{3.35}$$

such that

$$d_0 = \frac{\pi^2}{3} \left(\frac{b}{W} \right)^2 \frac{\tau}{U\mu}, \tag{3.36}$$

which, save for the prefactor is the combination obtained using dimensional analysis. Considering $n = 1$ to define the limiting wavelength between a stable and an unstable regime, a much simpler stabilization criteria based on the dimensionless surface tension parameter is obtained where

$$\begin{cases} d_0 > 1, & \text{stable}, \\ d_0 < 1, & \text{unstable}, \end{cases} \tag{3.37}$$

This criteria only defines a very general stable/unstable regime. To incorporate the wavelength of the fingers/perturbation the criterion is

$$\begin{cases} d_0 > \frac{1}{n^2}, & \text{stable}, \\ d_0 < \frac{1}{n^2}, & \text{unstable}, \end{cases} \tag{3.38}$$

where n corresponds to the boundary condition of the wavelength l constrained by the width of the cell W. Considering that the relation between the wavelength and wavenumber $l = 2\pi/q$, then, $l = W/n$. This n defines the size of the discrete perturbation, as seen in Fig 3.1.

3.2.3 Discussion

The results of this analysis arrive at the following differential equation

$$\dot{A} = A \left(\frac{U}{b^2/12\mu} - \tau q^2 \right) \frac{b^2}{12\mu} q, \tag{3.39}$$

where

- U: interface displacement velocity

- b: cell depth

- q: perturbation's wave vector

- τ: surface tension

- μ: viscosity

This expression leads to a simple conclusion, in an instability, the perturbation will grow if the parenthesis coefficient result a positive number, and it will be stable if the coefficient is less than zero. In terms of the velocity, Bensimon *et al.*. suggest three cases

1. Small U: Few bumps are seen that later flatten or stabilize.

2. Intermedia te U: Present bumps that grow into stable fingers.

3. Large U: Chaotic behavior is evidenced by branching and splitting of fingers.

In their analysis, they introduce the surface tension parameter (d_0) as a dimensionless control parameter, which is inversely proportional to interface velocity

$$d_0 = \frac{\pi^2}{3} \frac{b^2}{W^2} \frac{\tau}{\mu U}. \tag{3.40}$$

So those parameters seem to correctly describe the behavior of the perturbed system. To be more specific, we shall talk about the perturbations in terms of the length of the perturbation in the interface. This can

be done thanks to this new parameter introduced. From the simplified expression we can extract very powerful expectations for the front behavior. Prediction of different wavelength instabilities can be derived from the differential equation

$$\dot{A} = A\left(1 - d_0 n^2\right) U q, \tag{3.41}$$

where the minimum value of q is given by n=1/2 (that depicts a perturbation of the size of the cell width). Hence, we can sum up everything into the following conclusions:

1. The flat interface will be perturbed by **any** wavelength long as $d_0 < 4$.

2. The flow patterns will be unstable and lead to thin finger formations as long as $d_0 < 1$.

3. The criteria $d_0 < 1/n^2$ is a more general form to study instabilities in terms of the amplitude of the perturbation: A=W/2n.

4. For a very long interface, the system will be unstable for perturbation of wavelengths $l < W \sqrt{d_0}$ or amplitude $2A < W \sqrt{d_0}$.

5. For very small surface tensions, the system becomes highly unstable, easy to be perturbed even for very short wavelength perturbations.

In Fig. 3.1 we depict a simple way to understand how **n** is related to the size of the perturbation A, described by d_0. Basically, if $d_0 < 1/n^2$ for n=1, $d_0 <1$ implies that the interface will be perturbed by amplitudes of size A=W/2 or smaller. Thus, the same for the higher order perturbations.

Thanks to this criterion, we can now guide our studies by taking into account the possible instabilities that could emerge regarding the conditions of the experiment.
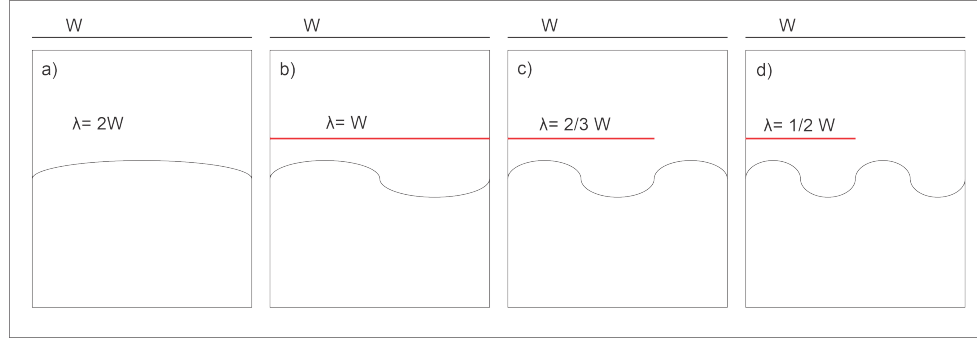
Figure 3.1: Displacement patterns. The displacement patterns can be defined by the wavelength, where $l = W/n$. The size of the perturbations (fingers) will be half the wavelength. Thus, it can be related to the cell width through $A = l/2$, leading to $A = W/2n$. Where A is the amplitude discussed in the instability derivation.

3.3   Finger width correspondence to surface tension parameter

In the Saffman and Taylor approach discussed in section 3.2, it was not established a mathematical relation between the surface tension parameter and the finger width. Following the work developed by McLean and Saffman[20] (MS) we look for a mathematical relation between the parameters of interest mentioned. This derivation, is also based on a quasi-2D system that neglects the contribution of a transverse curvature produced by the cell depth b. Here, we only take in account surface tension effects due to lateral curvature to integrate the dependence of the finger width.

Based on Darcy's law, and the pressure jump between both fluids at the finger's interface, MS derived the steady equations for a finger flowing in a channel. From these equations, a dimensionless parameter for the surface tension can be extracted, but this time including finger width contribution.

Beginning with pressure jump equation, where R is the radius of curvature of the finger's tip, and χ is the contact angle of the meniscus (which is considered to be 0) we have

$$p_0 - p = \frac{\tau}{R} + \frac{2\tau}{b} \cos \chi. \tag{3.42}$$

Setting boundary conditions to the harmonic velocity potential of Darcy's law, we have the following

expression, where ϕ is the velocity potential, and θ is the angle between the tangent vector to the finger q and the direction of movement of the finger (see MS)[20].

$$\begin{cases} \frac{\partial \phi}{\partial y} = 0, & \text{if } y = \pm a, \\ \frac{\partial \phi}{\partial n} = U \sin \hat{\theta}, & \text{if on the finger,} \end{cases} \tag{3.43}$$

where $a = W/2$. The conjugate of ϕ defines a streamline function ψ. The relation between them depends on the velocity, such that

$$v_x = \frac{\partial \phi}{\partial x} = \frac{\partial \psi}{\partial y}, \tag{3.44}$$

and

$$v_y = \frac{\partial \phi}{\partial y} = -\frac{\partial \psi}{\partial x}. \tag{3.45}$$

Now, through Darcy's law, we can find the relation between the functions ϕ and ψ, and their coordinates x and y, obtaining

$$\psi = Uy, \quad \phi = Ux. \tag{3.46}$$

We introduce λ to describe the ratio of the finger width to the cell width, and it is introduced in order to study the behavior. The motion of the finger will be in $x+$ direction, so that the velocity field behind the finger will tend to 0. The following boundary conditions are expected

$$\phi \sim 0 \text{ as } x \to -\infty, \quad \lambda a < |y| < a,$$
$$\phi \sim U\lambda x \quad \text{as} \quad x \to \infty, \quad -a < y < a, \tag{3.47}$$

In order to study the interface, it is much more convenient to work in dimensionless quantities and a moving frame with respect to a origin set at the tip of the finger. In order to do that, McLean and Saffman introduced $a = W/2$ and $(1 - \lambda)U$ to make our variables dimensionless

$$\hat{x} = (x - Ut)/a, \quad \hat{y} = y/a, \quad \hat{R} = R/a, \tag{3.48}$$

and

$$\hat{\phi} = \frac{\phi - Ux}{(1-\lambda)Ua}, \quad \hat{\psi} = \frac{\psi - Uy}{(1-\lambda)Ua}. \tag{3.49}$$

By using the visual representation of our system, we can find a relation between the radial component $\hat{R}$, angular component $\hat{\theta}$ and $\hat{\phi}$, and the vector $\hat{q}$

$$\frac{1}{\hat{R}} = \frac{d\hat{\theta}}{d\hat{S}} = \frac{\partial\hat{\theta}}{\partial\hat{\phi}}\frac{\partial\hat{\phi}}{\partial\hat{S}} = \hat{q}\frac{\partial\hat{\theta}}{\partial\hat{\phi}}, \tag{3.50}$$

Now we need an equation for the motion of the finger with respect to the tip, in terms of $\hat{q}$ and $\hat{\theta}$. This expression can be derived using equations 3.50, 3.42 and 3.43. Using the definition of $P = -\frac{12\mu\phi}{b^2}$ and the relation from the dimensionless radial component in the equation 3.42, we get

$$p_0 + \frac{12\mu\phi}{b^2} = \frac{\tau}{\hat{R}a} + \frac{2\tau}{b}, \tag{3.51}$$

where we can introduce the Eq.3.50. It is important to notice the difference between dimensionless and dimensional terms in this derivation

$$p_0 + \frac{12\mu\phi}{b^2} = \frac{\tau}{a}\hat{q}\frac{\partial\hat{\theta}}{\partial\hat{\phi}} + \frac{2\tau}{b}. \tag{3.52}$$

Putting all variables in terms of the dimensionless expressions described previously,

$$p_0 + \frac{12\mu}{b^2}\left(\hat{\phi}(1-\lambda)Ua + Ux\right) = \frac{\tau}{a}\hat{q}\frac{\partial\hat{\theta}}{\partial\hat{\phi}} + \frac{2\tau}{b}. \tag{3.53}$$

Replacing x=$\hat{x}/a$ and $p_0 = \frac{2\tau}{b}$, we obtain

$$\hat{\phi} = \frac{\tau b^2}{12\mu Ua^2(1-\lambda)}\hat{q}\frac{d\hat{\theta}}{d\hat{\phi}} - \frac{\hat{x}}{(1-\lambda)}. \tag{3.54}$$

To differentiate with respect to the dimensionless arc-length along the interface $\hat{S}$ we have to consider:

$$\cos\theta = \frac{d\hat{x}}{d\hat{S}}, \quad \frac{d\hat{\phi}}{d\hat{S}} = \hat{q}, \quad \frac{d\hat{\phi}}{ds} = -\frac{1}{\pi s}, \quad \frac{ds}{d\hat{S}} = -\hat{q}\pi s \tag{3.55}$$

Differentiating along the interface to obtain a second relation between $\hat{q}$ and $\hat{\theta}$

$$\frac{d\hat{\phi}}{d\hat{S}} = \frac{\tau b^2}{12\mu U a^2 (1-\lambda)} \frac{d}{d\hat{S}}\left(\hat{q}\frac{d\hat{\theta}}{d\hat{\phi}}\right) - \frac{d\hat{x}}{d\hat{S}}\frac{1}{(1-\lambda)} \tag{3.56}$$

Using the relations described in Eq. 3.55

$$\hat{q} = \frac{\tau b^2}{12\mu U a^2 (1-\lambda)} \frac{d}{d\hat{S}}\left(\hat{q}\frac{d\hat{\theta}}{d\hat{\phi}}\right) - \frac{\cos\theta}{(1-\lambda)}, \tag{3.57}$$

where

$$\cos\hat{\theta} = \frac{\tau b^2}{12\mu U a^2} \frac{d}{d\hat{S}}\left(\hat{q}\frac{d\hat{\theta}}{d\hat{\phi}}\right) - \hat{q}(1-\lambda). \tag{3.58}$$

Solving for the only derivative on the left, which is in terms of a multiplication of dependent variables

$$
\begin{aligned}
\frac{d}{d\hat{S}}\left(\hat{q}\frac{d\hat{\theta}}{d\hat{\phi}}\right) &= \frac{d\hat{q}}{d\hat{S}}\frac{d\hat{\theta}}{d\hat{\phi}} + \hat{q}\frac{d}{d\hat{S}}\left(\frac{d\hat{\theta}}{d\hat{\phi}}\right), \\
&= \frac{d\hat{q}}{d\hat{S}}\left(\frac{d\hat{\theta}}{d\hat{S}}\frac{d\hat{S}}{d\hat{\phi}}\right) + \hat{q}\frac{d}{d\hat{S}}\left(\frac{d\hat{\theta}}{d\hat{S}}\frac{d\hat{S}}{d\hat{\phi}}\right), \\
&= \frac{d\hat{q}}{d\hat{S}}\left(\frac{1}{\hat{q}}\frac{d\hat{\theta}}{d\hat{S}}\right) + \hat{q}\frac{d}{d\hat{S}}\left(\frac{1}{\hat{q}}\frac{d\hat{\theta}}{d\hat{S}}\right), \\
&= \frac{d\hat{q}}{d\hat{S}}\left(\frac{1}{\hat{q}}(-\hat{q}\pi s)\frac{d\hat{\theta}}{ds}\right) + \hat{q}\frac{d}{d\hat{S}}\left(\frac{1}{\hat{q}}(-\hat{q}\pi s)\frac{d\hat{\theta}}{ds}\right), \\
&= -\pi s\frac{d\hat{\theta}}{ds}\frac{d\hat{q}}{d\hat{S}} - \hat{q}\frac{d}{d\hat{S}}\left(\pi s\frac{d\hat{\theta}}{ds}\right), \\
&= -\pi\frac{d}{d\hat{S}}\left(\hat{q}s\frac{d\hat{\theta}}{ds}\right), \\
&= \pi^2 \hat{q}s\frac{d}{ds}\left[\hat{q}s\frac{d\hat{\theta}}{ds}\right].
\end{aligned}
\tag{3.59}
$$

Thus, our equation becomes

$$\cos\hat{\theta} = \frac{\tau b^2}{12\mu U a^2}\pi^2 \hat{q}s\frac{d}{ds}\left[\hat{q}s\frac{d\hat{\theta}}{ds}\right] - \hat{q}(1-\lambda). \tag{3.60}$$

The boundary conditions for our system goes as follows, where $s = 0$ corresponds to a point in the tail of the finger, and $s = 1$ a point at the nose of the finger

$$\left.\begin{aligned}\hat{\theta}(0) &= \pi, & \hat{q}(0) &= 1/(1-\lambda),\\ \hat{\theta}(1) &= \pi/2, & \hat{q}(1) &= 0,\end{aligned}\right\} \tag{3.61}$$

Using the boundary conditions, we can say

$$\theta = \hat{\theta} - \pi, \quad q = (1-\lambda)\hat{q} \tag{3.62}$$

These expressions allow us to write an equation that is not explicitly dependent on λ, such that

$$\cos(\theta+\pi) = \frac{\tau b^2}{12\mu U a^2}\pi^2\left(\frac{q}{1-\lambda}\right)s\frac{d}{ds}\left[\frac{q}{1-\lambda}s\frac{d\hat{\theta}}{ds}\right] - q, \tag{3.63}$$

By considering the trigonometric property $\cos(\theta+\pi) = -\cos\theta$ and rearranging some terms we finally obtain

$$-\cos\theta = \frac{\tau b^2\pi^2}{12\mu U a^2(1-\lambda)^2}qs\frac{d}{ds}\left[qs\frac{d\hat{\theta}}{ds}\right] - q, \tag{3.64}$$

where the surface tension parameter is the dimensionless factor located in the first term of the right hand side

$$\kappa = \frac{\pi^2\tau b^2}{12\mu U a^2(1-\lambda)^2}, \tag{3.65}$$

replacing a=W/2:

$$\kappa = \frac{\pi^2 b^2\tau}{3W^2\mu U(1-\lambda)^2}, \tag{3.66}$$

leading to a final expression

$$-\cos\theta = \kappa qs\frac{d}{ds}\left[qs\frac{d\hat{\theta}}{ds}\right] - q.$$
(3.67)

3.3.1   Discussion

The parameter κ enables us to set a relation between the stabilization criteria and the finger width. In general, it is a good approximation to the behavior of the finger. The problem with this approximation is that it does not consider some physical contributions. For example, it considers as if the displacing fluid totally pushes the displaced fluid. This assumption excludes the addition of a layer of displaced fluid in the plates due to wettability [12]. Actually, according to Tabeling *et al.* (1987)[44] the film plays a crucial role in the stability of the system, but by now we will neglect it as well.

Regarding the superficial conditions considered, this study actually brings important conclusions

- There is a dependence between the finger width and the capillary number.

- The dependence is not only based on the capillary number, but on the aspect ratio W/b describing the same shape of the relation under a different magnitude.

- Convergence of the finger width to $\lambda \to 1/2$ as the $\kappa \to \infty$.

3.4   Characteristic time for instability development

We have already talked about the instability conditions for our system and the width the fingers should have depending on whether they are stable or not. Now, we must also consider that the formation of an instability is not immediate, so that there should be a characteristic time for the instability to show up. Lets keep working on the quasi two-dimensional case. Then, the study of section 3.2 should provide us the information we need.

The instability criteria of equation 3.31 refers to the growing rate of a perturbation of amplitude A. In the previous study we determined whether the instabilities tend to grow or dampen. In this study, we will use the same equation to determine the characteristic time for the instability to appear or disappear.

3.4.1 Derivation of characteristic time

Recalling the equation for the growth/dampening of an instability

$$\dot{A} = A\left(\frac{U}{b^2/12\mu} - \tau q^2\right)\frac{b^2}{12\mu}q. \tag{3.68}$$

The equation can be used to determine how fast the perturbation A grows/dampens. But given that $\dot{A}$ is a velocity, whose dimension would be L/T (length over time) and in the right hand side we have A (length) multiplied by another factor. This factor should be of dimension $1/T$. This time determines how fast A will grow or decrease depending on the sign of t_{char}

$$\dot{A} = \frac{A}{t_{char}}, \tag{3.69}$$

where

$$t_{char} = \frac{12\mu}{qb^2}\frac{1}{\left(\frac{U}{b^2/12\mu} - Tq^2\right)} \tag{3.70}$$

Using the same procedure than the one described in the derivation of the control parameter d_0 at subsection 3.2.2, we can reorganize this term in terms of the surface tension parameter.

$$t_{char} = \frac{1}{(1 - d_0 n^2)}\frac{W}{2\pi n U}. \tag{3.71}$$

3.4.2 Discussion

The characteristic time determines the time required for the instability to occur under the conditions provided. Thus, now we have enough information not only to know under which conditions is the system unstable, but how long will take the instability to show up. The characteristic time t_{char} determines what is known as *critical slowing down* in critical phenomena where the dynamics develops ever more slowly as we approach a phase boundary. In Eq. 6.1 we see the same stability criteria than in Eq. 3.68, which indicates the stability of the system. Hence, for the characteristic time we will also see positive and negative

values. The negative values imply that the system is already stable, and it will never reach the perturbation amplitude defined by **n**, which comes form A= W/2n, as described in sec. 3.2. For positive values, the system is allowed to grow fingers of amplitude A=W/2n or smaller. Positive values will determine the time that a perturbation takes to grow from a flat interface.

This is an important parameter given that using this we can decide whether the conditions of the experimental set-up are unstable enough to produce the instability within the cell, or if we need a longer cell to let the instability develop over time.

Even more importantly, it helps to avoid wrong conclusions. If the used cell does not allow the fingers to develop in the expected time, then we could think that there is no instability under the conditions but actually we did not let the system enough time to develop.

3.5   Stability analysis of 3D perturbed interface

The stability analysis of the interface in a two dimensional case is important to give an idea of the behavior of the system, and is a good approximation if the aspect ratio (W/b) is big enough. However, the Hele-Shaw cell where experiments are performed is actually three dimensional and it is important to consider what conclusions from realistic situations can be drawn from quasi two-dimensional systems and which cannot. Until now, we have only considered the radius of curvature of the displacement front in the plane of motion, but what about the interface's other curvature transverse to the direction of the flow?[12]. This curvature tends to be $b/2$ and actually provides a much higher contribution to the pressure jump than the radii R of the finger. Recall that the pressure jump is in charge of the motion of the finger. It is important to use a correct approximation for this equation[12]. Thus, instead of using Eq. 3.19, the following pressure jump is suggested on Bensimon *et al.*

$$\Delta P = \frac{\tau}{b/2}\left[1 + 3.80\left(\frac{\mu v_n}{\tau}\right)^{2/3}\right] + \frac{\pi}{4}\tau\kappa. \tag{3.72}$$

The derivation follows the same procedure than the one described for the 2D system in section 3.2. The equations differ in the use of a pressure jump that considers 3D contribution.

3.5.1 Perturbation of the flat interface

In the same way that we described in section3.2, using Darcy's equation and the 3D pressure jump, we obtain

$$\dot{A} = \left(\frac{U - \frac{\pi}{4}\tau q^2 \frac{b^2}{12\mu}}{1 + 0.42 qb \left(\frac{T}{\mu U}\right)^{1/3}} \right) qA. \tag{3.73}$$

3.5.2 Derivation of 3D surface tension parameter d_1

Analogously to the derivation for the 2D interface, the stability of the system depends of the terms within the parenthesis. Hence, for $\dot{A} > 0$ the perturbation increases, while for $\dot{A} < 0$ the perturbation decreases.

$$\left(\frac{U - \frac{\pi}{4}T q^2 \frac{b^2}{12\mu}}{1 + 0.42 qb \left(\frac{T}{\mu U}\right)^{1/3}} \right) > 0. \tag{3.74}$$

From this expression the denominator can only affect the sign depending on the movement of the interface, U>0 or U<0, in order to simplify the expression, we can multiply by the unity U/U to obtain

$$\left(1 - \frac{\pi}{4} T q^2 \frac{b^2}{12\mu U} \right) \frac{U}{1 + 0.42 qb \left(\frac{T}{\mu U}\right)^{1/3}} > 0, \tag{3.75}$$

and

$$\left(1 - \frac{\pi}{4} T \left(\frac{2\pi n}{W}\right)^2 \frac{b^2}{12\mu U} \right) > 0. \tag{3.76}$$

Thus, again we obtain a expression for the dimensionless surface tension parameter. In order to avoid confusions with the control parameter of the 2D case, lets call it d_1.

$$\left(1 - d_1 n^2 \right) > 0, \tag{3.77}$$

where

$$d_1 = \frac{\pi^3}{12} \left(\frac{b}{W} \right)^2 \frac{\tau}{\mu U}. \tag{3.78}$$

3.5.3   Discussion

Once again, the control parameter will determine the limit between a stable or unstable behavior. The difference in this new control parameter is that it reaches an unstable behavior faster than the 2D case. Actually, both cases can be related through:

$$d_1 = \frac{\pi}{4} d_0, \tag{3.79}$$

The $\pi/4$ factor comes from the contribution of the transverse curvature of the finger. Then, we would expect that a real 3D system reaches the instability faster than a two dimensional one.

Chapter 4

Experimental Procedure

In this chapter we will see the experimental set-up built to evidence the behavior deducted by the theoretical analysis previously described. The experiment is based on the procedure suggested by Saffman and Taylor[19], where a less viscous fluid displaces a more viscous one, generating finger-like structures. Our aim is to replicate those structures in order to evidence the instabilities desired.

In the upcoming sections we will see how the experimental set-up works, which are the most relevant characteristics of our experiments, the available conditions that our set-up allows us to use, the procedure, and the method for data collection.

4.1 Experimental set-up

4.1.1 Injection system

The injection system was built in the workshop at Yachay Tech University. It is based on the Open-source syringe pump library[45]. The device consists on making a platform controlled by a motor-actuated rotating screw that moves toward a syringe to inject its contents into the micro-model. Given that the platform crosses the lead-screw perpendicularly, it moves along with the rotation (as a nut in a bolt)[45]. The pumping velocity will depend on the velocity of rotation of the motor, and the size of the screw's thread. Thicker

threads are more distanced between them, so that those screws move the platform faster than those of thin threads. In Fig 4.1 we can see the parts of the set-up.
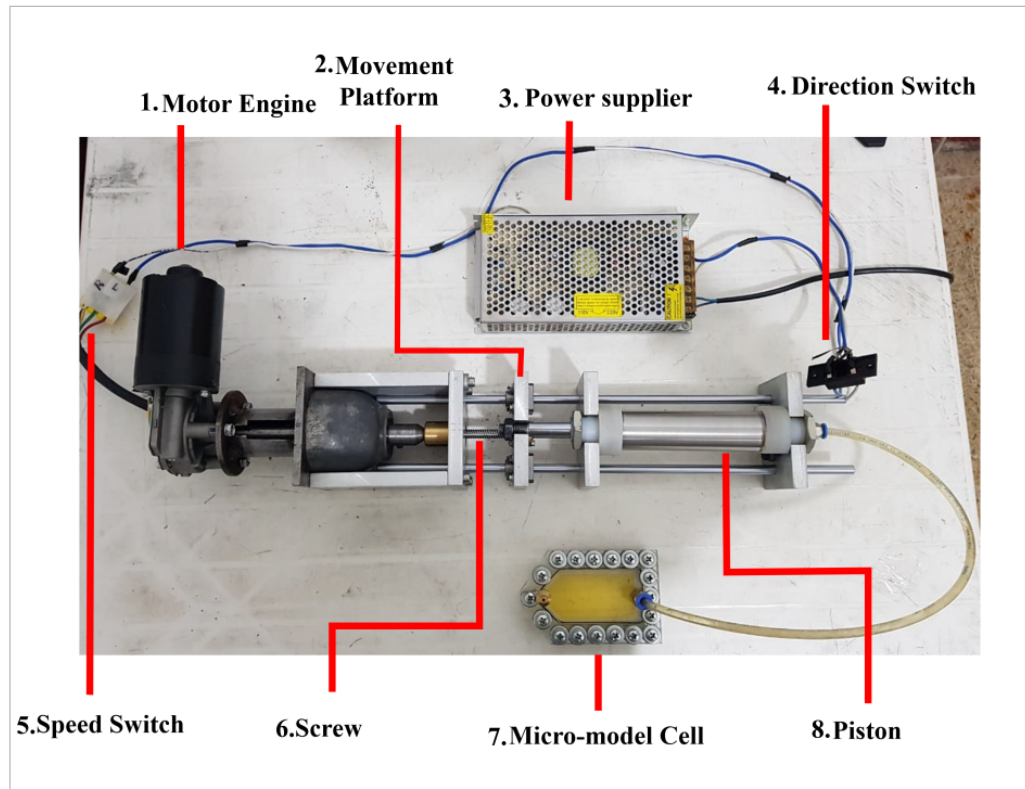
Figure 4.1: Experimental set-up.

The injection system itself is composed by:

1. **Electrical Motor**. The motor provides the torque in order for the screw to displace the platform.

2. **Movement platform**. This platform is screwed on the rotating screw. It pushes or pulls the piston's tail, making it expel or absorb content into it.

3. **Power supply**. This part provides energy to the motor. The power supply used has an output of 12V and 10A.

4. **Direction switch**. The motor used has the option of rotating in two directions. Then, the direction switch allows to configure the motor to make the system move forward or backwards.

5. **Speed switch**. The engine used has two possible settings for rotation velocity. This switch allows to set if we want to work at the high or low speed.

6. **Screw**. This is the lead-screw that is attached to the rotating motor. As the screw rotates, the platform that passes through it displaces according to the movement of the screw.

7. **Micro-model cell**. This cell is where the fluid is injected and the experiment is performed. It is made of Plexiglas and is sealed to contain liquids at a pressure higher than the atmospheric pressure.

8. **Piston**. The piston is made from stainless steel. Its inner radii is 27.5mm. It is kept still by two fixed platforms and the tail is allowed to move with the action of the movement platform. In that way, the content is displaced as desired. The head of the piston is connected to a hose that drives the fluid to the micro-model.

The set-up is composed by two pistons, in each of them we add either reference fluid 1 or fluid 2. There are three screws available that give us different velocities to push the piston. The engine allows to set two velocities of rotation per screw, then we should have 6 different velocities to push the piston's content. In Fig. 4.2 we can see the screws available to be used in the injection system.
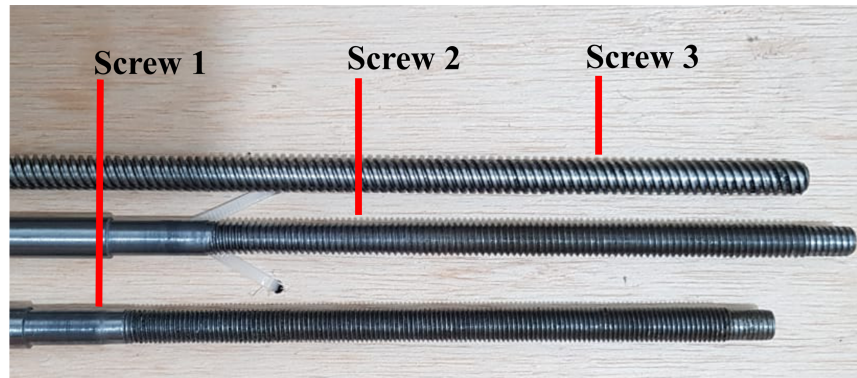
Figure 4.2: Lead-screws. The thread of the screw determines, along with the rotation speed of the electrical motor, the speed of injection. Screw thread 1 is the thinnest while screw 3 is the coarsest i.e. screw 1 will drive the slowest fluid injection while screw is used for the fastest injection rates.

To determine the velocity of displacement of the pushing platform we let the screws rotate at the two available velocities of the motor. Then we measured the distance displaced in a minute. In Table 4.1 we can see the results of the velocities measured for each screw available in the pumping system. The thickness of the lines in the screws are the ones that define their velocities. We will talk about the *Screw 1* as the thinnest (slowest), the *Screw 2* has an intermediate size and velocity, and the *Screw 3* is the thickest (fastest). It is evident that there is a velocity repeated between the screws 1 and 2, meaning that we actually have only five different displacement velocities for the pistons.

Table 4.1: Screw velocities

Screw	Velocity [m/s]	Piston's Caudal [m^3/s]
1	0.000019	1.2 x10^{-8}
	0.000025	1.5 x10^{-8}
2	0.000025	1.5 x10^{-8}
	0.00037	2.2 x10^{-8}
3	0.000082	4.9 x10^{-8}
	0.00017	9.9 x10^{-8}

4.1.2   Micro-models

In order to see Saffman-Taylor instabilities, we designed micro-models based on Hele-Shaw cells geometries. The structure of the cells were based on the experiment performed by Guillen *et al.*[46]. The micro-model geometry permits to study a specific configuration, the one that will directly affect to the fluid flow. In the previous section we have already talked about the parameters that affect the stability of the system. The dimensions of the cell will allow us to play with the width W and depth b of the channel in which the interaction between the fluids occur. Setting different cell depths will let us evidence how the system changes from a stable to an unstable regime depending on its conditions.

In Fig. 4.3 the structure of the micro-models can be seen. The three layers are constructed of transparent Plexiglas. The thickness of the bottom and top layer is always fixed at 3mm to make them resistant to the pressure of the system. The thickness of the middle layer is fundamental, given that this is the one that determines the dimension of the cell depth b. We propose to work with the cell depths of $b = 3$mm, $b = 2$mm, $b = 1$mm. The white circles are the perforations where we insert a set of screws that join the three parts together into a single piece. Due to the clamping of the screws, we do not need additional o-rings to prevent leaking, but the system is capable of working at the pressures required.

The case of the micro-model of depth $b = 1$mm seen in Fig. 4.4 is a special case. Given that there were no sheets of 1mm Plexiglas at the local market, we use a 2mm layer and carved it with a laser cutter. Then, for this prototype we have only two layers. The top layer will have the input and output entrances, and the bottom layer contains the carved out shape of the cell at thickness $b = 1$mm.

Based on the prototype of Guillen *et al.*[46], the shape of the micro-models have a triangular input and output channels that enhances the recovery of the fluid. The dimensions of the system proposed are fixed to 35mm in width. The length of the channel does not affect to the stability of the system, so we propose two micro-models, the first of length 75mm, the other of length 90mm as evidenced in Fig 4.5.
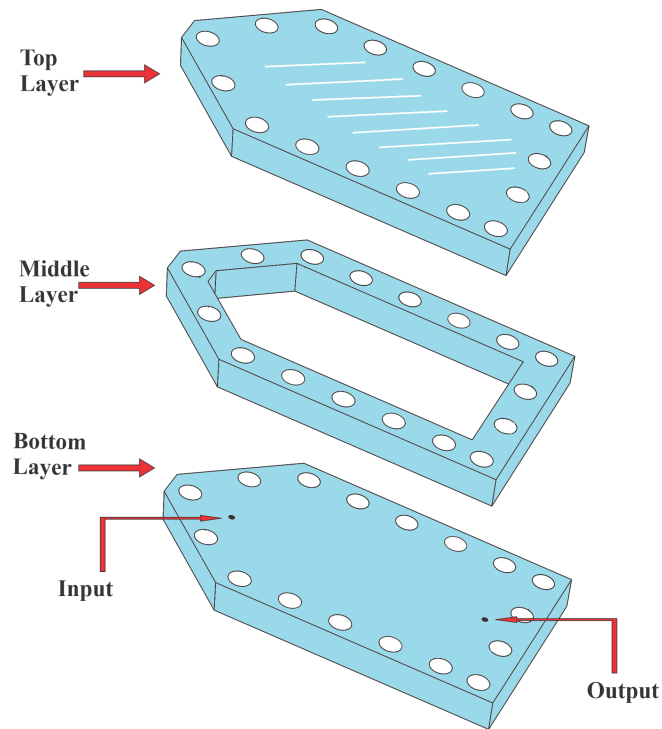
Figure 4.3: Micro-model cell design. The micro-models are composed of three layers, the top and bottom layers seal the system, with the bottom one having input an output perforations. The middle layer determines the boundary geometry for fluid injection. The material depicted as light blue is made of transparent acrylic that allows to observe the behavior within the cell.
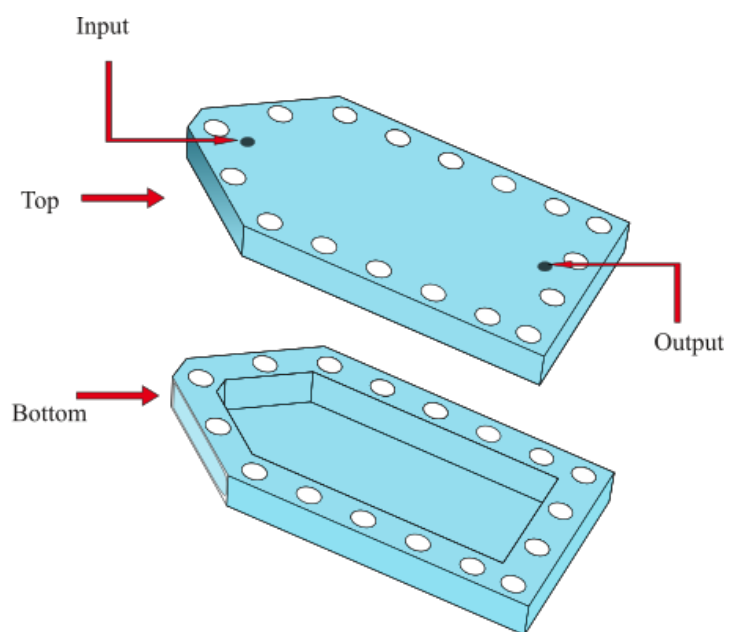
Figure 4.4: Micro-model cell design.
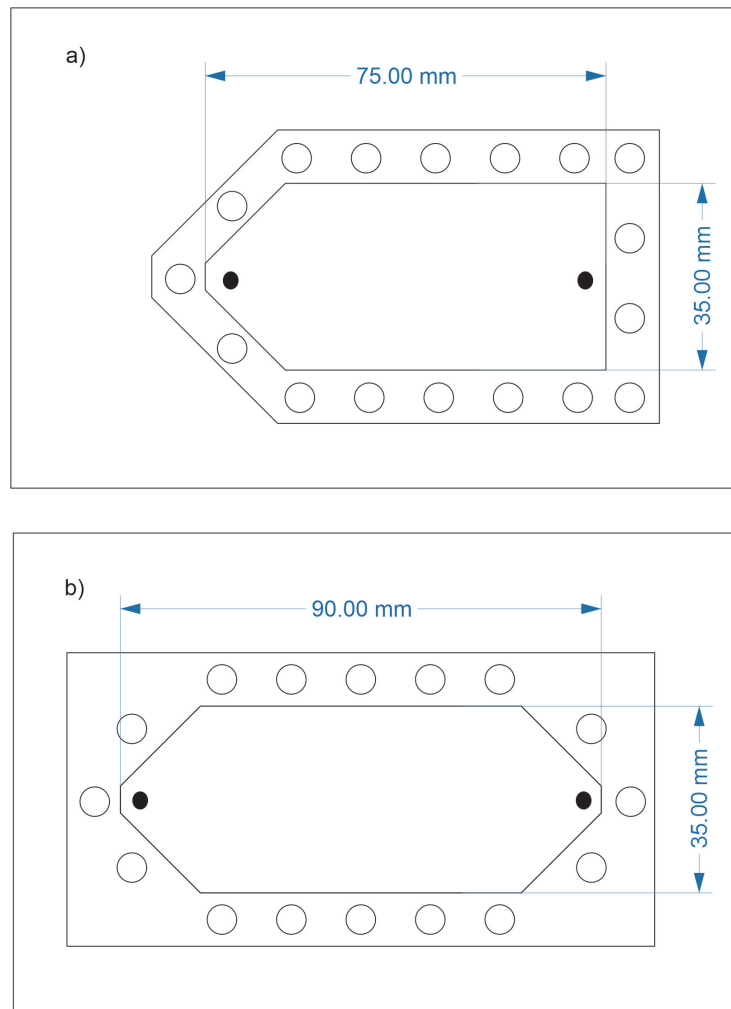
Figure 4.5: Micro-model cell design. a) The micro-model is of smaller dimension but allows to examine the input from different front geometries, a flat one and one influenced by varying width. b) The second micro-model is longer, it provides more time to evidence the instabilities.

4.2 Experimental Procedure

In this experiment we expect to visualize finger instabilities in the micro-models proposed. First we need to input the more viscous fluid to the cell, then we displace it by introducing the less viscous fluid. We have to be careful with some details at the moment of inserting the displacing fluid into the cell. If the procedure is not carried on carefully, unexpected behaviors like droplets, air intrusion or bubbles can appear. The ideal procedure goes as follows:

1. Ensemble the injection system with the screw that performs the desired velocity.

2. Select the micro-model desired ($b = 1mm$, $b = 2mm$, $b = 3mm$).

3. Fill each piston with fluid 1 and fluid 2 depending on assay.

4. Configure the initial position of the displacement platform so that it has enough distance for the piston's tail to fit in.

5. Place the piston that contains fluid 1 in the injection system.

6. Connect the piston to the micro-model through a pipe.

7. Select the configuration of the speed switch. (Do you want the fast or low configuration of the motor?)

8. Make sure the direction switch is on the *forward* configuration.

9. Turn on the motor.

10. Stop the motor when the micro-model is full of fluid 1.

11. Set the direction switch to the *backwards* configuration to move the displacement platform to the initial position.

12. Place the piston that contains fluid 2 in the injection system.

13. Take the micro-model and drain it slightly until there is no more fluid in the port of input.

14. Turn on the motor and let the fluid fill the pipe.

15. Connect the pipe of the piston to the micro-cell.

16. Let fluid 2 displace fluid 1.

17. Stop the motor before fluid 2 arrives to the output port.

18. Photograph the obtained pattern.

19. Repeat all the steps for the different micro-models.

If the steps are followed strictly as indicated, there won't be any inconsistencies in the experiment. The steps 12, 13 and 14 are crucial to obtain good results. When we first inject fluid 1 into the micro-model, the connector port between the pipe and the micro-model is partially filled with the fluid. If we connect the pipe of fluid 2 to the port while it still has some remnants of the other fluid, it is possible that the pipe inject some of fluid 1 into the cell. So, we will not be pushing fluid 1 as desired, given that we would be actually injecting fluid 2 inside of the other, leading to undesired bubbles or droplets that interfere with our system.

Bubbles of air or water can show-up. If any of them touches the interface of displacement, a forced instability appears, such as splitting of the interface. The air bubbles are easy to handle. If any air bubble appears, before letting the fluid 2 displace fluid 1, put the micro-model vertically with the output at the top, so that the density will take the bubble to the top wall and it won't interfere with the displacement. However, if a water bubble appears, frequently it combines with the water finger. Most frequently, the bubbles will be small and their interface is strong, so they do not combine with the main water body injected and it will interfere with the displacement. In that case, if a water bubble is visible, we must place the micro-model vertically, with the output port at the bottom and the input at the top. Then, inject fluid 1 again until the water bubble goes out of the system.

4.3 Fluid displacement velocities

The velocities discussed in the previous sections correspond to the displacement of the piston and the volume of liquid displaced. By the flow rate equation and continuity conditions, the flow will remain constant, while the displacement velocity will depend on the transverse area[47]. Then, in our case, the velocity of the fluids will depend on the cell we are using because we are working with different depths that lead to different transverse areas. The width of the micro-models is fixed at W = 35mm, while the depth b changes depending on the cell. Then, the transverse area, where the displacement front occurs is A = 0.035 x b m^2. In the same way, the transverse area of the input is given by A = 0.002 x b m^2, where 0.002m is the width of the input port.

In the Table 4.1, we already have the flow rates (Q) of fluid moved by the pistons. Using the flow rate equation (4.1) and the condition of continuity for incompressible fluids, we can use the flow to determine the input velocity and front velocity. The input velocity will be useful for the simulations performed, while the front velocities are required to study the stability of the system.

The input velocity is given by the simple relation

$$v = \frac{Q}{A}.$$
(4.1)

In Table 4.2, there are 5 front velocities available for each micro-model. Of course, the higher the area, the slower the displacement velocity. In terms of instability, we need the fastest velocities to generate fingers. Still, slower velocities are useful to prove that we are working on different regimes depending on the conditions used.

Table 4.2: Cell dimensions and available injection velocities for injection

Cell depth [m]	Screw	Input Velocity [m/s]	Front Velocity [m/s]
b=0.001	1	0.0057	0.00034
	2	0.00748	0.00043
		0.01096	0.00063
	3	0.02461	0.00141
		0.04963	0.00283
b=0.002	1	0.00287	0.00017
	2	0.00374	0.00021
		0.00548	0.00031
	3	0.01230	0.00070
		0.02482	0.00142
b=0.003	1	0.00191	0.00011
	2	0.00249	0.00014
		0.00365	0.00021
	3	0.00820	0.00047
		0.01654	0.00094

4.4   Data acquisition

In this section, we will see what the conditions are and methods used to obtain the data we will analyze. In order to study the stability of the system, we want to use the surface tension parameter to plot stability maps. Then we need to determine the values of the variables involved in the surface tension parameter. As mentioned before: viscosity, surface tension, cell depth, cell width, front velocity. The cell depth and cell width are fixed variables, we already talked about the way to compute the front velocities. The surface tension is in general, a value extracted from the literature, and we need to calculate the viscosity of the fluids. The other data required to perform the stability analysis is the finger to cell width ratio. This parameter will allow us to quantify the level of instability and compare it with the stability map.

4.4.1 Viscosity calculation

First of all, we need to differentiate between kinematic and dynamic viscosity. As claimed by Soares (2015)[48] "dynamic viscosity is the resistance to movement of one layer of a fluid over another", while the kinematic viscosity is the dynamic viscosity over density. It is actually a ratio between viscous and inertial forces[48].

In our studies we work with dynamical viscosity. This parameter is dependent on temperature, so it is not enough to look for the viscosity value at the literature. Also, we are working with motor oils, so that the properties of the oils differ between companies. this means that the viscosity of oil 15W40 is not the same for Gulf and Amalie. Therefore, we must be specific when looking for the information. In this study we will work with Gulf TEC Plus 20W50 and Amalie Imperial Turbo 15W40.

In oil data sheets we can usually find the kinematic viscosity at 100°C and 40°C, the density at a given temperature, and the viscosity index. In order to calculate the viscosity at a different temperature we need the viscosity of the fluid at two temperatures, or the viscosity at a given temperature and the viscosity index. Using the Andrade Correlation[49] we can determine the kinematic viscosity at room temperature 25°C.

Following the method proposed by Van *et al.* (1972)[49], the viscosity is calculated by:

$$\mu = a e^{\frac{b}{T}}, \tag{4.2}$$

where μ is viscosity, T is temperature, b and a are the factors of correlation. First we find b as a function of the temperature and viscosity of the fluid at 40°C and 100°C respectively

$$b = \frac{\ln \mu_{40} - \ln \mu_{100}}{\frac{1}{T_{40}} - \frac{1}{T_{100}}}. \tag{4.3}$$

In order to find a we use

$$\ln a = \ln \mu_{40} - \frac{b}{T_{40}}, \tag{4.4}$$

Then we can replace the values in the initial expression and obtain a value for the kinematic viscosity at the desired temperature. Now, using the density of the fluid, we obtain the dynamic viscosity of the fluids. This data is obtained from the correspondent data sheet[50][51]. The results for the oils to consider are evidenced in Table 4.3.

Table 4.3: Oil data sheet

Oil	Kinematic Viscosity @100°C [cSt]	Kinematic Viscosity @40°C [cSt]	Kinematic Viscosity @25°C [cSt]	Density [Kg/m3]	Dynamic Viscosity @25°C [Pa*s]
15W40	15	118	262.57	881.13	0.2313
20W50	17.5	157.65	371.68	879.1	0.3267

4.4.2   Finger - cell width ratio

The finger to cell width ratio will allow us to compare the stability of the experimental patterns captured by the displacement of oil with water. The size of the finger will give us a notion of the wavelength of the perturbation that predominates in the system, the same that can be compared to the stability proposed by the surface tension parameter.

The data is extracted from the pictures taken from the displacement of the fronts at different velocities and cell depth in the micro-models. From the pictures taken, the measurements of the width are done using *Inkscape*, an open software for image editing. We recall that the images imported are not to scale, that is the reason why we have to measure both, the cell width and the width of the finger. Using the *measurement tool* we can obtain a precise value of the size of these parameters. In the case of the width of the finger, in Fig. 4.6 it is evident that the width of the finger varies as it displaces along the *x axis*. This variable width is caused by the interaction of the fluids with the walls at the entrance. After the displacement front does not interact with the walls anymore, it tends to take its stationary shape. Then, we have to measure the finger width at a distance approximately the size of the radius of curvature of the tip.

Once we make the corresponding measurements, we are not really interested on the net values, but
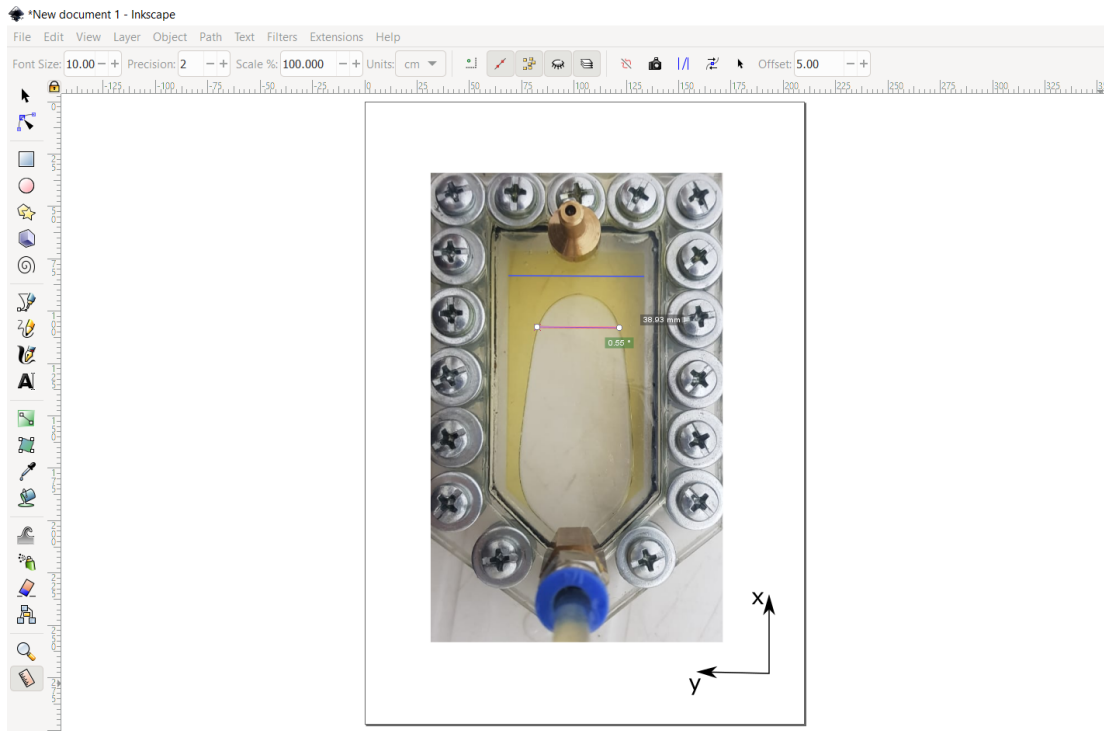
Figure 4.6: Measurement of finger to cell width ratio. This is a screenshot of the software Inkscape. In the cell, the blue line is the width of the cell we have to measure, while the red line corresponds to the width of the finger.

on the relative size of the finger width with respect to the cell width. Then, we will be talking about the relative finger width λ. The results of the measurements can be seen in Table 4.4. The errors related to these measurement are portrayed in the results. The calculation of the errors of propagation are seen in Appendix B.

Table 4.4: Relative Finger Width

Cell depth [m]	Screw	Front Velocity [m/s]	Cell Width [px]	Finger Width [px]	Rel. Finger Width lambda
0.001	1	0.000327514	295	290.35	0.62
	2	0.000427143	293	287.75	0.6087
		0.000626543	296.5	282.57	0.6
	3	0.00140615	296.88	236.77	0.546
		0.00283623	296.88	212.64	0.521739
0.002	1	0.000163757	296.7	259.1	0.9778
	2	0.000213571	297.25	252.14	0.9565
		0.000313271	296.6	227.28	0.951219
	3	0.000703077	296.88	192.2	0.8148
		0.00141811	296.5	176.58	0.6818
0.003	1	0.000109171	296.01	194.24	0.999
	2	0.000142381	294.81	187.3	0.9787
		0.000208848	295.66	181.57	0.95833
	3	0.000468718	296.07	173.8	0.81405
		0.00094541	295.66	167.65	0.660131

4.5 Stability Maps

A stability map is used to plot regions that show different behaviors according to the values of the parameters in the system. In order to make the stability plot, we have selected W vs U in order to identify the zones of stability. This configuration was selected because it will allow us to evidence each case of instability with more detail. We need to evidence the cases specially in terms of the viscosity of the displaced fluid and the thickness of the cell. Hence, by setting them as constants and plotting the interaction between W and U it is easier to evidence the regions of stability. We are not evaluating how the width changes with the velocity, but how stable the system is as the velocity and cell width vary. Other configurations can be more compact and allow us to see all of our cases in a single plot, but unfortunately, it will not be clear to evidence in detail the possible instabilities of the system. By now, relating W and U through a constant number and using the 2D stability criteria suggested by Saffman and Taylor, the surface tension parameter

d_0, we can provide a prediction for the stability of the system by mapping

$$W = \sqrt{\frac{\pi^2 b^2 T}{3\mu d_0}}\sqrt{\frac{1}{U}}. \tag{4.5}$$

According to our 2D analysis, described in section 3.2, the limit between a stable and unstable regimes depends on the critical value $d_0 = 1$. Then, fixing this parameter we can already divide our plot in two regimes, stable or unstable. By the shape of the surface tension parameter, we know that W and U have both an inverse contribution to d_0. This means that as W and U grow, d_0 decreases. From our analysis, we also concluded that $d_0 < 1$ stands for an unstable regime. Thus, on the top of our line plot the zone will be unstable, while below the line plot, the system will be stable.
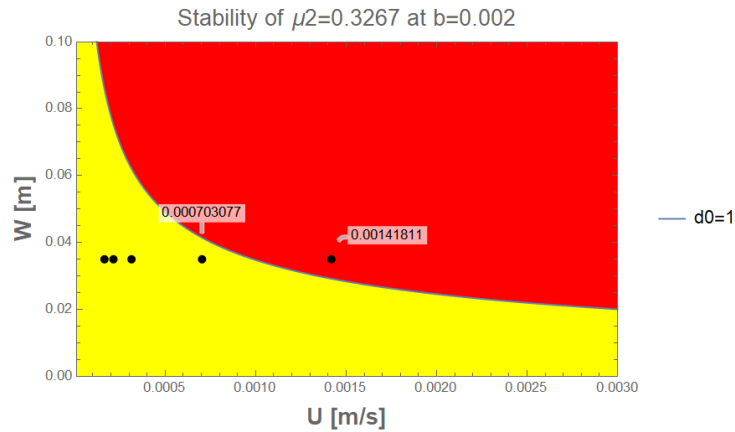
Figure 4.7: W - U stability diagram of $\mu=0.3267$ Pa·s and $b = 2$mm. The line separating both regions depicts the equality in Eq.4.5 for $d_0 = 1$. The yellow region is the stable zone, meaning that there are flat fronts or fingers of amplitude A> W/2. The red region implies instabilities, or finger formation that converges at A=W/2 or smaller amplitudes as the points get deeper into the instability region. The black dots are the experimental values at fixed width of $W = 35$mm, and front velocity determined by the injection system. Most of the dots hit the yellow region, it implies that should be wide fingers or a flat interface evidenced. Instead, the last point is in the red region, meaning that there is already the formation of a finger.

The Figure 4.7 is a clear example of how the stability plot works. It is important to mention that the

deeper a point is in the unstable zone, the more unstable it gets and the faster it converges to its stationary behavior. In order to study instabilities in more detail, we can use the more general form of the control parameter d_0 obtained from the 2D stability analysis performed in section 3.2, where $d_0 < 1/n^2$. This definition extends the analysis in order to see what kind of instabilities can be developed. As previously mentioned, the order of the instability can be discussed in terms of the wavelength of the perturbation. The wavelength of the perturbation can be discretized according to the boundary conditions of the micro-model walls. In general, the wavelength is $l = W/n$ where the values of n are fixed at: n= 1, 3/2, 2, 5/2, etc. Remember that actually, we are interested on the size of the perturbation, the one that is given by $A = l/2$, or $A = W/2n$. In the following table 4.5 we can see a summary of these relations, that now will allow us to talk about the instabilities in terms of the size of the perturbations.

Table 4.5: Influence of **n** into surface tension parameter

n	d0	A
1	1	W/2
3/2	4/9	W/3
2	1/4	W/4

In analogy to the stability map shown in Fig. 4.7, we can study higher instabilities in the same way. In Tab. 4.5 we can see the amplitudes of the perturbations that could appear according to the control parameter d_0. As previously discussed in section 3.2, the interpretation of $d_0 < 1/n^2$ implies that the system will be unstable for perturbations equal or smaller than A=W/2n. To illustrate this argument, the case where $d_0 = 1$ is just the case of $n = 1$. If we replace it into A, the amplitude of the expected perturbation would be $A = W/2$. Then, for $d_0 > 1$ we expect the width of the fingers to be greater than half cell width. For points where $d_0 < 1$ the system is said to be unstable for perturbations equal or smaller than A=W/2, which will lead the fingers to converge at those amplitudes. The same for the other instabilities, lets say that we plot the stability line for n=3/2, then the higher amplitude allowed to perturb the system would be A=W/3. In the plot, the points that hit the region above the line will tend to converge at amplitudes equal or smaller than W/3, while the points bellow the stability line must be of higher amplitudes. Now, lets say that an

experimental point hits an intermediate region as seen in Fig. 4.8. In the case of the given examples, the point would be expected to converge at an amplitude between (W/2 > A > W/3). However, it is important to mention that the fact that an experimental value hits in a region of instability does not necessarily means that the finger will already have that amplitude. It just means that it will tend to converge to that state, this will also depend on the time that the system will take to converge to the stationary state at that point.
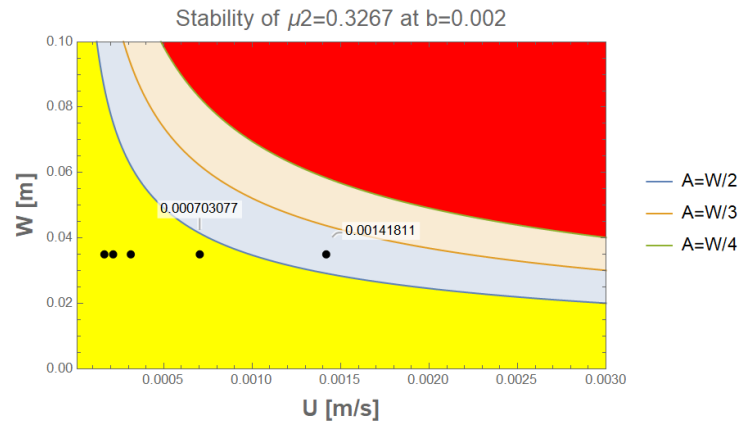
Figure 4.8: W - U stability diagram for μ=0.3267 Pa·s and b = 2mm at different instability levels. The blue line is the limit where a finger starts to develop and tends to converge to $\lambda \rightarrow 1/2$. Departing from the orange region, instabilities that tend to converge at $\lambda \rightarrow 1/3$, and so on.

According to Saffman and Taylor[19], and Saffman and McLean[20], fingers converge at $\lambda \rightarrow 1/2$ and there are no higher order perturbations. Of course, these studies were developed when the field was just emerging. Nowadays, we know that actually the system can converge into smaller amplitudes through front splitting[52].

4.5.1 Choosing the right oil

The aim in this research is to experimentally evidence instabilities and compare the results with the diagrams of stability. This study is made with the purpose of studying crude oil behavior under a water-flooding extraction process. In Appendix A, there is a table containing the data of the most common crude oils extracted around the world. There, we can see that the dynamic viscosities cover a range from 2.4cp

to 693.8cp[1]. This means $0.0024Pa \cdot s$ to $0.6938Pa \cdot s$. The dynamic viscosity of our displacing fluid (water) at room temperature is approximately $0.00084Pa \cdot s$. We need a viscous contrast high enough to evidence instabilities, but not so high to break our micro-models. Analyzing the case between two engine oils 15W40 and 20W50, whose dynamic viscosities are μ=$0.2313Pa \cdot s$ and μ=$0.3267Pa \cdot s$ as seen in Table 4.3. With help of the stability maps, we can evaluate the most appropriate oil to use.

By comparing the performance of both oils, it would be preferable to work with oil 20W50. At $b = 3$mm there is no great difference between the behavior of the fluids, but at $b = 2$mm the less viscous oil does not present many changes in its behavior, given that it is still in the stable regime. Instead, the more viscous fluid at least hits an instability region at $b = 2$mm. Finally at $b = 1mm$, the oil 15W40 already hits the some possible instabilities but none hits the orange region. Instead, with oil 20W50, we could expect to reach all the desired instabilities faster than in the other case because the experimental points are further from the instability lines.
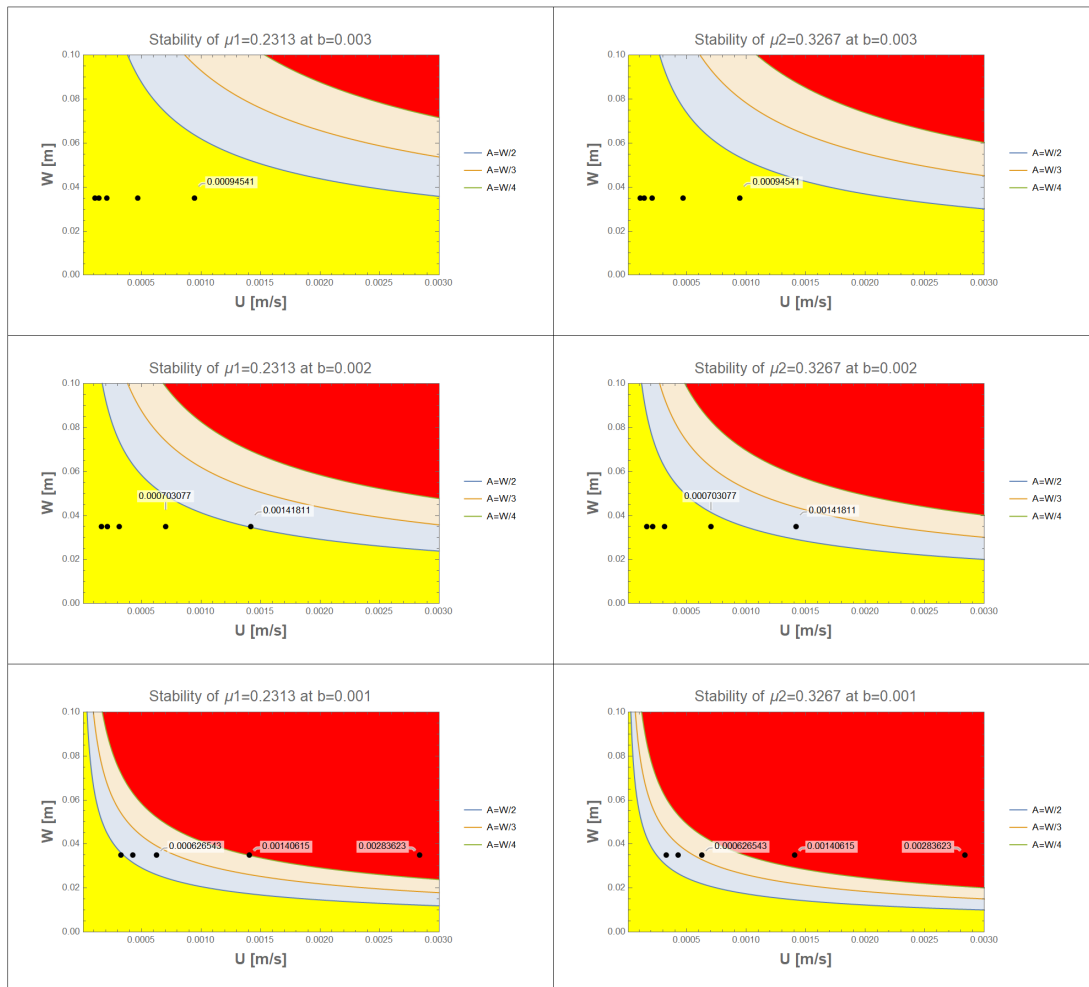
Figure 4.9: Stability diagram summary. The first column corresponds to the stability of oil 15W40 $\mu = 0.2313Pa \cdot s$, the second column corresponds to the stability of oil 20W50 $\mu = 0.3267Pa \cdot s$. These are the fluid candidates to be displaced. It is evident that under the same circumstances, as expected, oil 20W50 is more unstable.

Chapter 5

Computational Approach

In this chapter we will review the computational approach carried on in this research. The experiments are very often limited by the resources available. In our case, with a pandemic, the development of the experimental set up has being limited by the conditions. The computational approach aims to replicate the finger structures obtained in the experiments. Once that we are able to reproduce our experimental results, we can use the computational model to propose new micro-models, study fluid behaviors before performing experiments. In general, this approach will be a resource saving procedure that will prevent us from building micro-models that do not show the desired behavior.

In this chapter we will briefly review the general features of the software COMSOL Multiphysics, describe the method used by COMSOL to simulate a two phase flow, and explain the modules, characteristics and specific conditions set to model our system.

5.1 COMSOL Multiphysics

COMSOL Multiphysics is a powerful simulation software. It can be used for "modeling designs, devices, and processes in all fields of engineering, manufacturing, and scientific research" (COMSOL INC.)[53]. This software counts on several modules including electromagnetics, structural mechanics and acoustics,

fluid flow and heat transfer, chemical engineering, multipurpose, interfacing products. Of course, we are interested on the *Fluid flow and Heat transfer module*. Specifically, we require the *computational fluid dynamics* (CFD) module to perform our simulations to reproduce the experiments proposed. The advantage of COMSOL is that it allows to perform powerful simulations from a personal computer. Furthermore, its friendly interface allows to develop simulations without previous programming skills. Still, it also has modules that link the software to other programming software like CAD, MATLAB, EXCEL, and many others.

At Yachay Tech University, we obtained the licence for COMSOL Multiphysics through the contest **CEPRA** financed by **CEDIA** with the proyect:

> CEPRA XIV: FLUIDOS DE PERFORACIÓN BASADOS EN BIOPOLÍMEROS Y OBJETOS 2- DI-MENSIONALES PARA APLICACIONES EN PROCESOS DE EXPLORACIÓN Y PRODUCCIÓN DE HIDROCARBUROS "BIOFLUID2D"

The software was purchased to support the work in this thesis, and the results obtained here will be reported to CEDIA as part of the achievements of the approved funding.

5.1.1   CFD module

The CFD module included in COMSOL Multiphysics is quite extensive. It is useful for predicting, understanding and designing fluid flows in open or closed systems[54]. Its applications are so wide that it can simulate from laminate, multi-phase or turbulent flows under stationary or time dependent problems in two or three dimensional spaces. The simulation provided by this module is not restricted to the visualization of the fluid flow, but there are several measurable variables that can be selected to quantify the obtained solution. "It gives accurate estimates of flow patterns, pressure losses, forces on submerged objects, temperature distributions, and variations in fluid composition within a system" (COMSOL INC.)[54].

The simulation of fluid dynamical processes is based on the solution of partial differential equations that define the model. In order to have good estimations of the model, it is needed to introduce the right specifications, initial and boundary conditions of the system. The user does not introduce the equations,

but the module already suggests the equations to be solved according to the libraries used to perform the simulation. However, the software also let the user to personalize the equations if it is required. The equations are solved based on stabilized finite element formulation for fluid flow, combined with damped Newton methods[54]. For time-dependent problems, it uses different time-dependent solver algorithms.

In simple words, the workflow of this module consists on:

- Defining the geometry: We have to build the shape of our system where the fluid will flow.

- Select the fluids to be modeled: The libraries of COMSOL have a *material* section, where we can choose predetermined fluids with their correspondent properties. However, we can also change some properties of the fluids in order describe our actual materials.

- Select the type of flow: The CFD module has many kinds of flows that can be simulated, such as reacting flows, reacting flows in porous media, multiphase flow, nonisothermal flow, among others. Each of this kind of flows can also be subdivided in laminar, turbulent and many others.

- Define boundary and initial conditions.

- Define the mesh: The mesh is a discretization of the whole geometry in smaller elements[55]. COMSOL has several ways to deal with the mesh building. You can either construct your own mesh, or use a Physics-controlled mesh.

- Select a solver: The solver is the method used to solve the set of equations. COMSOL group the solvers into *studies* according to the physics of the system. The most general studies are *stationary* or *time-dependent*[56].

- Visualize the results: The result node shows the data-sets, derived values, tables, and plots of the solutions[56].

The CFD module has several physic interfaces, each with specific features to build a model. These features include the input of the fluid properties, initial conditions, boundary conditions and possible

constraints [54]. The interfaces are based on the physical laws of conservation of mass, energy, and momentum of the fluids. Translating these laws into partial differential equations, the system can be solved using the initial and boundary conditions.

The CFD module has the following physic interfaces:

- Chemical species transport

  - Laminar flow

  - Reacting flow (laminar flow, turbulent flow)

  - Reacting flow in porous media (transport of diluted species, transport of concentrated species)

- Fluid Flow

  - Single - Phase Flow (creeping flow, viscoelastic flow, laminar flow, turbulent flow, etc.)

  - Multiphase flow (two phase flow level set, two phase flow phase field, bubbly flow, turbulent bubbly flow, mixture model, turbulent mixture model, euler-euler model, etc)

  - Porous media and subsurface flow (brinkman equations, multiphase flow in porous media, two phase Darcy's law, etc)

  - Nonisothermal flow (laminar flow, turbulent flow, large eddy simulation)

  - High march number flow (High Mach Number flow, compressible Euler equations, etc)

  - Thin-Film flow (Thin-film flow shell, thin-film flow domain, thin-film flow edge)

  - Shallow water equations

- Heat transfer

  - Conjugate heat transfer (laminar flow, turbulent flow).

For our purposes, we are interested in the *two-phase flow, level set* component. This will allow us to compute the interaction between two fluids neglecting wetting effects with the walls. There is the option to

use the *Multi-phase flow in porous media*, this option adds the influence of the solid phase corresponding to the rock, meaning fluid-rock interactions. Nevertheless, by now we want to maintain the study based only on the fluid-fluid interaction.

5.1.2 Laminar Two-Phase flow, level set

For two-phase flow systems can be modeled through level set interface, phase field interface, moving mesh interface methods. These methods are specifically for two fluids separated by an interface. The level-set method tracks the interface using fixed mesh[57]. This method is very efficient because it focuses only on tracking the interface between immiscible fluids. We can use either a laminar flow or a turbulent flow. The laminar flow faithfully models for low Reynolds numbers, while the turbulent flow better describes the high Reynolds number regime. The model accepts incompressible or compressible fluids. This study is necessarily conducted through a time-dependent solver, given that the interface will be constantly changing position over time[57]. This method considers the differences between the viscosities and densities of the fluids including surface tension and gravity. The module uses the Navier-Stokes equations for two fluids:

$$\rho\frac{\partial \mathbf{u}}{\partial t} + \rho(\mathbf{u} \cdot \nabla)\mathbf{u} = \nabla \cdot \left[-p\mathbf{I} + \mu\left(\nabla\mathbf{u} + \nabla\mathbf{u}^T\right)\right] + \mathbf{F}_g + \mathbf{F}_{st} + \mathbf{F}_{ext} + \mathbf{F}, \tag{5.1}$$

and

$$\nabla \cdot \mathbf{u} = 0, \tag{5.2}$$

In this equation, ρ is density, $\mathbf{u}$ is the Darcy velocity, p is pressure, I is the identity matrix, μ is viscosity, $\mathbf{F}_{st}$ is the force contribution due to surface tension, $\mathbf{F}_g$ is the contribution of gravity, $\mathbf{F}_{ext}$ is a force that arises due to an external free energy. All the forces are actually force contributions over volume. The level set equation is used to track the interface along the geometry. With γ being the re-initialization parameter, ϵ is the interface thickness controlling parameter, which is usually half of the maximum element size[57].

$$\frac{\partial \phi}{\partial t} + \mathbf{u} \cdot \nabla\phi = \gamma\nabla \cdot \left(\varepsilon\nabla\phi - \phi(1-\phi)\frac{\nabla\phi}{|\nabla\phi|}\right), \tag{5.3}$$

Also, the density and dynamic viscosity are in terms of the level set function ϕ, where $\phi < 0.5$ stands for fluid 1, and $\phi > 0.5$ for fluid 2:

$$\rho = \rho_1 + (\rho_2 - \rho_1)\,\phi, \tag{5.4}$$

$$\mu = \mu_1 + (\mu_2 - \mu_1)\,\phi. \tag{5.5}$$

5.2 Simulation of Stable viscous finger in Hele-Shaw cell

In order to create a model that helps us to computationally replicate the experiments performed, we used the Two-Phase Flow (level Set). In this section we will discuss the geometry, materials and initial conditions used in our simulation.

First of all, the **geometry** of our system is based on the micro-models described in Chapter 4. For the simulation we will be working in a 2D geometry, which is close to our experimental model because the aspect ratio W/b allows us to consider a quasi 2D experiment.
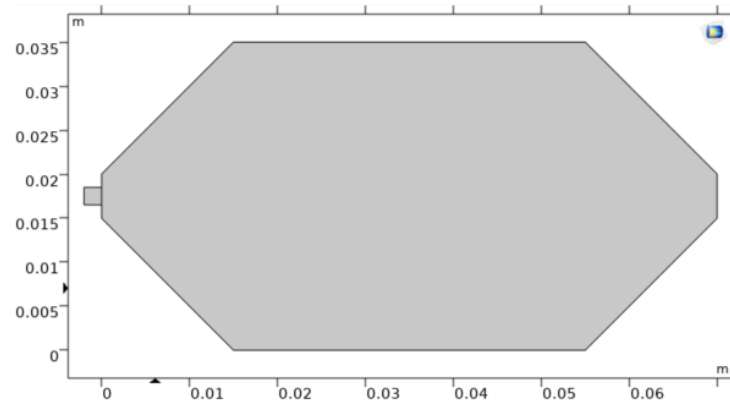

Figure 5.1: Geometry. The shape and dimensions of the geometry are based on the micro-models proposed. It is composed by two parts, a small square and a chambered rectangle. The square on the left represents the fluid input end.

The **materials** used were extracted from the materials library of COMSOL Multiphysics. We used water and engine oil. COMSOL has the option of customizing our fluids, so we set the density and viscosity of the engine oil we used in the experiments. As initial conditions we set water to be at domain 1 (square), and engine oil at domain 2 (polygon). The displacement of the simulation will be from left to right, letting water displace oil.

From the *level set* package we define: no flow at the walls, inlet and outlet properties. From the *laminar flow* configurations, we do the same. Specify the inlet and outlet and activate the *shallow channel approximation*, which will allow to consider a transverse thickness for the channel. The input velocities go according to the ones described in Table 4.2.

Regarding to the **mesh**, we used a *Physics-controlled mesh* with element size *Finer*. This is a predetermined kind of mesh built by COMSOL to create the most suitable elements according to the physic interfaces used.

Table 5.1: COMSOL Simulation parameters

Parameter	Symbols	Value
Length of the domain	L	90mm
Width of the domain	W	35mm
Viscosity of oil	μ_2	0.3267 Pa $\cdot s$
Density of oil	ρ_2	879.1 kg/m^3
Viscosity of water	μ_1	From Library
Density of water	$\rho 1$	From Library
Surface Tension	T	0.03 N/m
Injection speed	U_0	From Tab. 4.2
Channel thickness	b	1mm 2mm 3mm

The **solvers** were chosen according to a *Time Dependent* study, given that we require to track the position of the interface. The **result** desired from the simulation is the *Volume Fraction of Fluid*. These results plots the position of the interface along time. Thus, it is a visualizer for the fluid flow.

Chapter 6

Results & Discussion

In this Chapter, we will review the results according to the theoretical, experimental and computational approaches. The discussion is based on whether our experimental results coincide with our theoretical predictions previously described. We will join our experimental and computational results with the stability maps by comparing the behavior of the system under different experimental conditions. Also, we will analyze the displacement behavior in terms of the finger width and characteristic time for each aspect ratio W/b available. According to McLean and Saffman[20], the control parameters (d_0, d_1, κ) are dependent on two main variables, the capillary number, and the aspect ratio. Then, for different aspect ratios (different cell depth), there are different stability conditions expected. That is the reason why we have divided the results according to this parameter in different sections. Later, we will compare the results between the experimental and computational simulations, in order to decide under which conditions our simulation works better in order to use it for further predictions. Finally, we present the simulation of the behavior expected for the ideal situation where the fluid displacement begins from a initial flat interface.

Our experiments were developed using, as displaced fluid, *motor oil* 20W50, whose viscosity is $\mu = 0.3267$ Pa s, and displacing fluid, *water*, whose viscosity is $\mu = 8.90 \times 10^{-4}$ Pa s. Both, the simulation and the experimental set-up were equally configured. The viscosity, density, cell width and surface tension remain the same for the different aspect ratios. The experimental conditions are specified in Chapters 4 and

5, but can be also seen in Tab. 6.1. Then, what differs is the cell depth used, and the input velocity. The shape of the micro-models proposed in Fig. 4.5 are basically the same in terms of stability, they only differ on the recovery rate. The straight wall at the output of the micro-cell 1 retains oil at the corners, while the micro-cell 2 has a triangular shape at the output, which allows it to displace oil better than the other. Nevertheless, in this study we will make all measurements before the finger reaches the output. Given that by now we are just interested on the shape of the displacement, there is no difference in the resulting flow patterns of both micro-models.

As described in Chapter 4, section (4.3), there are 15 cases available to experiment. There are 5 velocities and 3 different micro-model depths. First we have to choose the micro-model depth we want to use. Then we set the desired velocity in our pumping system (choose the right displacing screw). Once we have all set, we input the most viscous fluid to be displaced (oil) into the cell. Finally, we displace the fluid with water and stop the system before the water arrives to the output hole. Within the study of each cell depth separately, each velocity used is distinguished by the name of **Plot case**, where the case (a) is the slowest and (e) is the fastest configuration.

6.1   Stability analysis according to cell depth

In this section we will study the stability of our experimental and computational simulations in comparison to the correspondent stability maps. The aim is to discuss whether our 2D theoretical analysis can predict the kind of patterns seen in our experiments or not. This stability analysis is complemented with the finger width and characteristic time of the patterns obtained.

For each cell depth studied in the following sections we will find: a table with the initial conditions for each experiment, a stability map that compares the expected flow patterns with the actual results of experiments and simulations, a table with the quantitative results of the flow patterns (surface tension parameter, relative finger width), and a table with the characteristic instability time. The stability map and the table for finger widths represent the same study, but the first is based on qualitative analysis, and the table allows to analyze the results from a quantitative perspective.

Table 6.1: Experimental conditions

Parameter	**Symbols**	**Value**
Cell Length	L	75mm
Cell Width	W	35mm
Viscosity of oil	μ_2	0.3267 Pa s
Density of oil	ρ_2	879.1 kg/m^3
Viscosity of water	μ_1	8.9×10^{-4} Pa s
Density of water	$\rho1$	997.77 kg/m^3
Surface Tension	T	0.03 N/m
Injection speed	U_0	From Tab. 4.2
Cell depth	b	1mm 2mm 3mm

Our interest is to compare the resulting patterns to the surface tension parameter d_0. Remember that this parameter is the one that tells us about the behavior of the system. Not only that, but more specifically, this parameter tells us about the amplitudes of the perturbation to which the system could converge according its conditions. In the section 4.5 we already mentioned that experiments where $d_0 > 1$ implies a stable front (yellow region), $d_0 < 1$ is perturbed by amplitudes A≤W/2 (blue region of the stability map). For $d_0 < 4/9$ ($d_0 < 0.444$) we can expect a tip splitting due to the perturbation of the front by amplitudes equal or smaller than $A = W/3$ (orange region of the stability map). For $d_0 < 1/4$ ($d_0 < 0.25$), perturbations of amplitude $A = W/4$ could appear (red region of the stability map), meaning that we could expect tip splitting, where each tip is of size $\lambda = 1/4$.

Table 6.2: Experimental conditions for b=3mm.

Cell depth [m]	Screw	Input Velocities [m/s]	Front Velocities [m/s]	Plot Case
b=0.003	1	0.0019105	0.000109171	a
	2	0.00249167	0.000142381	b
		0.00365483	0.000208848	c
	3	0.00820257	0.000468718	d
		0.0165447	0.00094541	e

6.1.1   Results for cell depth b=3mm.

The black dots plotted in Fig.6.1 are the experimental values corresponding to the cell width W=35mm and the front velocities seen in Table 6.2. In Fig. 6.1, there is a summary of the flow patterns obtained from the experimental and computational approaches. There, we can see a qualitative comparison between the three approaches. The stability map shows the possible patterns that we expect to evidence as explained in section 4.5. In Table 6.2, we see that the surface tension parameter is $d_0 > 1$ for all the experiments. Then, all the experimental values hit the yellow zone, which means that stable fronts are expected for all the displacements.
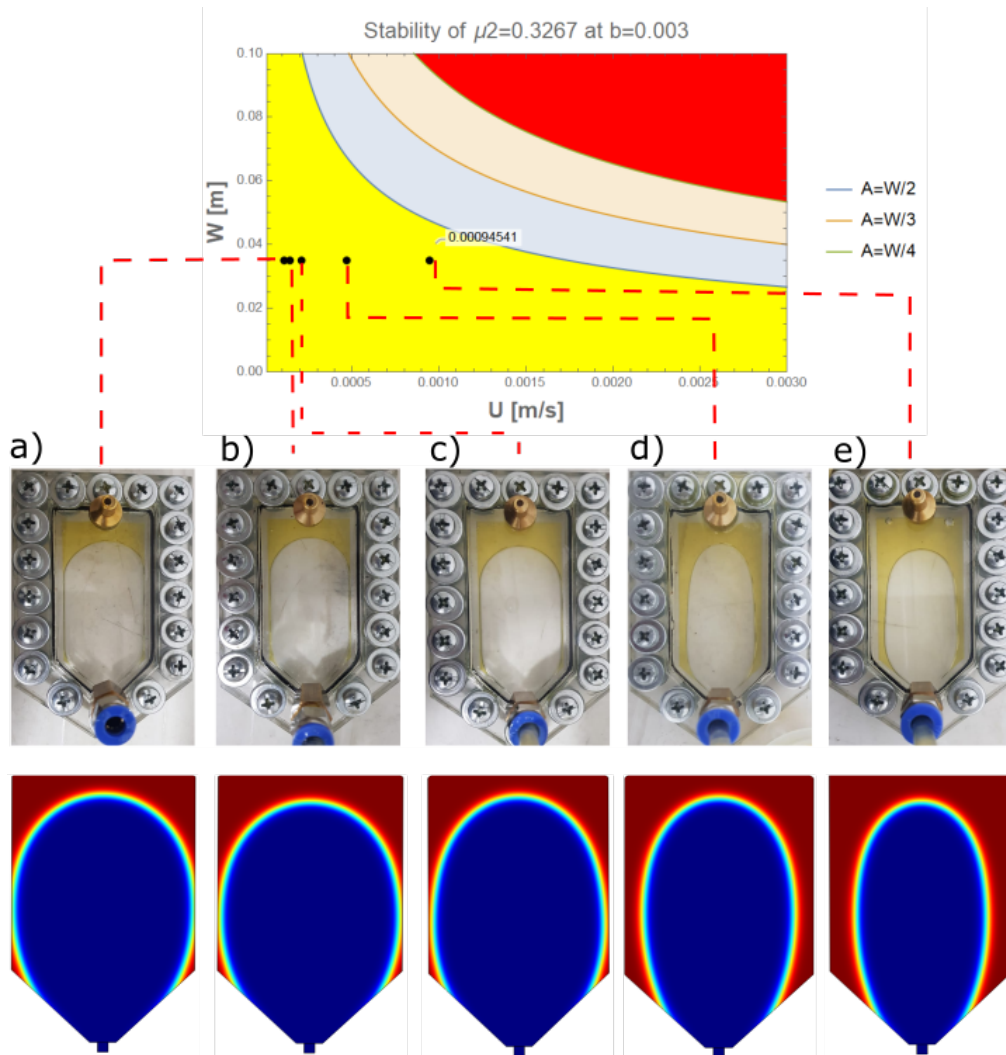
Figure 6.1: Experimental results for b=3mm cell. The dots are the experimental values used, these are mentioned in Table 6.2. The graph corresponds to the stability map of b=3mm. The first row under the stability map shows the experiments performed at Yachay Tech, maintaining all the parameters constant except for the input velocity using the cell depth b=3mm. The second row shows the simulations for the fluid displacement made with COMSOL Multiphysics. The red part of the simulation is the displaced oil, and the blue one is the water forming the fingers.

For the first three cases (a, b, c) at slow velocities, indeed we have stable fronts of the size of $A = W$ as expected. The last two cases are wide fingers. Although they are not of the size of the cell width, they

are larger than $\lambda = 1/2$, as seen in Fig. 6.1 and Table 6.3. This fingers are said to be in a transition region, where the displacement pattern is not of the size of the cell, neither of the size of the half cell width. Furthermore, it is possible that the fingers have not converged to their final width due to the cell length. This will be discussed later on according to the characteristic time.

With respect to the similarity between the simulation and the experimental results, we can see the same patterns. The fingers for the first three cases are of the size of the finger width, while the last two cases, they are already separated from the walls. From the moment that the interface between fluids is no longer attached to the lateral walls, they are considered to be a finger.

Finger width

In this study we will analyze the width of the fingers with respect to the cell width (relative finger width). Using the method described at section 4.4.2, the relative finger width obtained are denoted in Table 6.2. In Fig. 6.3 there is a plot of the relative finger widths with respect to the surface tension parameter for both, experiment and simulation. In Table 6.3, the relative fingers for both, simulation and experiment can be compared. The **Plot case** column, each case is filled with the color of the region in the stability map that the given point hits. This will avoid us to go back to the stability maps. The yellow region is stable $A < W$, the blue region is a half width finger $A < W/2$, the orange region is a tip splitting $A < W/3$, the red region is a tip splitting of smaller amplitude $A < W/4$.

Table 6.3: Finger width comparison between experimental and computational approaches at b=3mm.

Cell Height [m]	Front Velocity [m/s]	d0	Rel. Finger Width (Simulation)	Rel. Finger Width (Experiment)	Rel. Finger Difference	Plot Case
	0.000109171	20.3305	0.984237	0.999593	0.015356	a
	0.000142381	15.5885	0.982082	0.964052	0.01803	b
b=0.003	0.000208848	10.6274	0.953019	0.958838	0.005819	c
	0.000468718	4.73528	0.797528	0.811205	0.013677	d
	0.00094541	2.34767	0.716249	0.746632	0.030383	e

In Fig. 6.2 we can see that both, simulation and experiment are very close to each other, being in an acceptable range with respect to the error bars. This leads us to assume that the simulation corresponds very accurately to the experiment for this aspect ratio. This can also be confirmed in Tab. 6.3, where the absolute difference between both approaches ranges around 0.005 and 0.03. This absolute error is regarding the relative finger widths. Given that this is a *relative* quantity with respect to the cell width, the error in our finger widths is basically 0.005 or 0.03 times the cell width smaller or larger than the experimental finger width. Then, this error is not really representative. Actually, in the same figure we can see that the points hit values very close to each other in terms of the propagation errors related to them.
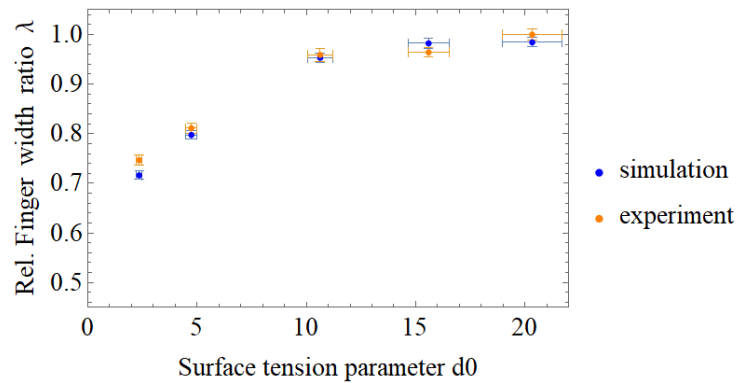
Figure 6.2: Relative finger width at b=3mm. This graph is the comparison between the experimental and computational results for the displacement of a more viscous fluid with a less viscous one at the aspect ratio W/b=35/3. The blue dots represent the experimental results, while the orange ones represent the simulation.

Also, it is remarkable to note that actually the relative finger widths measured correspond to values of fingers that have not converged yet, meaning that they could still grow or decrease in amplitude according to its location in the stability map. To verify this behavior, the complementary experiment seen in Appendix D, shows the development of some fingers under the same conditions of our experiments through longer times. There, we see that the plot case (c) finally converges at λ =0.988, which is wider than the relative finger width measured for this case in Tab. 6.3. The same happens for the plot case (d). In Fig. D.2 we see that the finger converges at λ=0.87, which is wider than the ones seen in Table 6.2, but thinner than

the cell width. Hence, if we let the system run for longer times until it converges to a stationary width, we will see that our experiments are not in their final shape. Another premise that could be extracted from this behavior is that there is not a strict convergence into a front of size $A = W$ in the stable region, but this means that the fingers could converge to other amplitudes between $A = W$ and $A = W/2$. It would be like a transition regime, where the fingers tend to appear, but they do not converge to the closest instability which in this case is $\lambda=1/2$. The reason for this behavior can be explained from the premise stated in the 2D interface analysis of section 3.2, the systems are allowed to be perturbed by wavelengths $l \leq W \sqrt{d_0}$ or amplitudes $2A \leq W \sqrt{d_0}$. This means that the finger is not restricted to converge at the exact amplitudes studied in our analysis, but they are just the limit or maximum amplitude allowed to appear in a region.

Characteristic Time

The role of the characteristic time was already discussed in Chapter 3, section 3.4. This parameter allows to identify the time that would take an instability to develop. Where the characteristic time:

$$t_{char} = \frac{1}{(1 - d_0 n^2)} \frac{W}{2\pi n U} \tag{6.1}$$

As previously discussed, there are positive and negative values for the characteristic times. The negative values correspond to the points that are stable with respect to the control parameter d_0. Thus, for $d_0 < 1$, where the maximum perturbation amplitude allowed is A=W/2, the values for the characteristic time will be negative if the fingers converge to greater amplitudes. The same for the higher order instabilities studied. The characteristic time is presented with respect to each possible perturbation, let it be amplitudes of $A = W/2, W/3, W/4$. Thus, we will see the time that an instability will take to develop for each point in our experiments.

In Table 6.4, we see that all the characteristic times are negative, meaning that we should not evidence any instability of the size of the perturbations proposed (A=W/2,W/3,W/4). As previously discussed, the structures obtained coincide very well with this analysis since all of the fingers seen are wider than $\lambda = 1/2$. The finger widths are not either of amplitude A=W, but the yellow region of stability only requires the

fingers to be greater than W/2, which agrees with our results.

Table 6.4: Characteristic time b=3mm.

Cell Height [m]	n	Amplitude [m]	Front Velocity [m/s]	Char. time [s]	Plot case
b=0.003	1	W/2	0.000109171	-2.63959	a
			0.000142381	-2.68179	b
			0.000208848	-2.77044	c
			0.000468718	-3.18166	d
			0.00094541	-4.37205	e
	3/2	W/3	0.000109171	-0.760251	a
			0.000142381	-0.765455	b
			0.000208848	-0.776087	c
			0.000468718	-0.820656	d
			0.00094541	-0.917285	e
	4	W/4	0.000109171	-0.317625	a
			0.000142381	-0.318832	b
			0.000208848	-0.321277	c
			0.000468718	-0.331205	d
			0.00094541	-0.351108	e

6.1.2 Results for cell depth b=2mm.

Table 6.5: Experimental conditions for b=2mm.

Cell Height [m]	Screw	Input Velocities [m/s]	Front Velocities [m/s]	Plot Case
b=0.003	1	0.00286575	0.000163757	a
	2	0.0037375	0.000213571	b
		0.00548225	0.000313271	c
	3	0.0123039	0.000703077	d
		0.024817	0.00141811	e

According to Table 6.6, the first four cases shown in Fig. 6.3 hit the yellow zone and correspond to $d_0 > 1$. Here, stable flow patterns are expected. For the last point, where $d_0 < 1$ and a finger that tends to

converge to the half of the cell width is predicted.
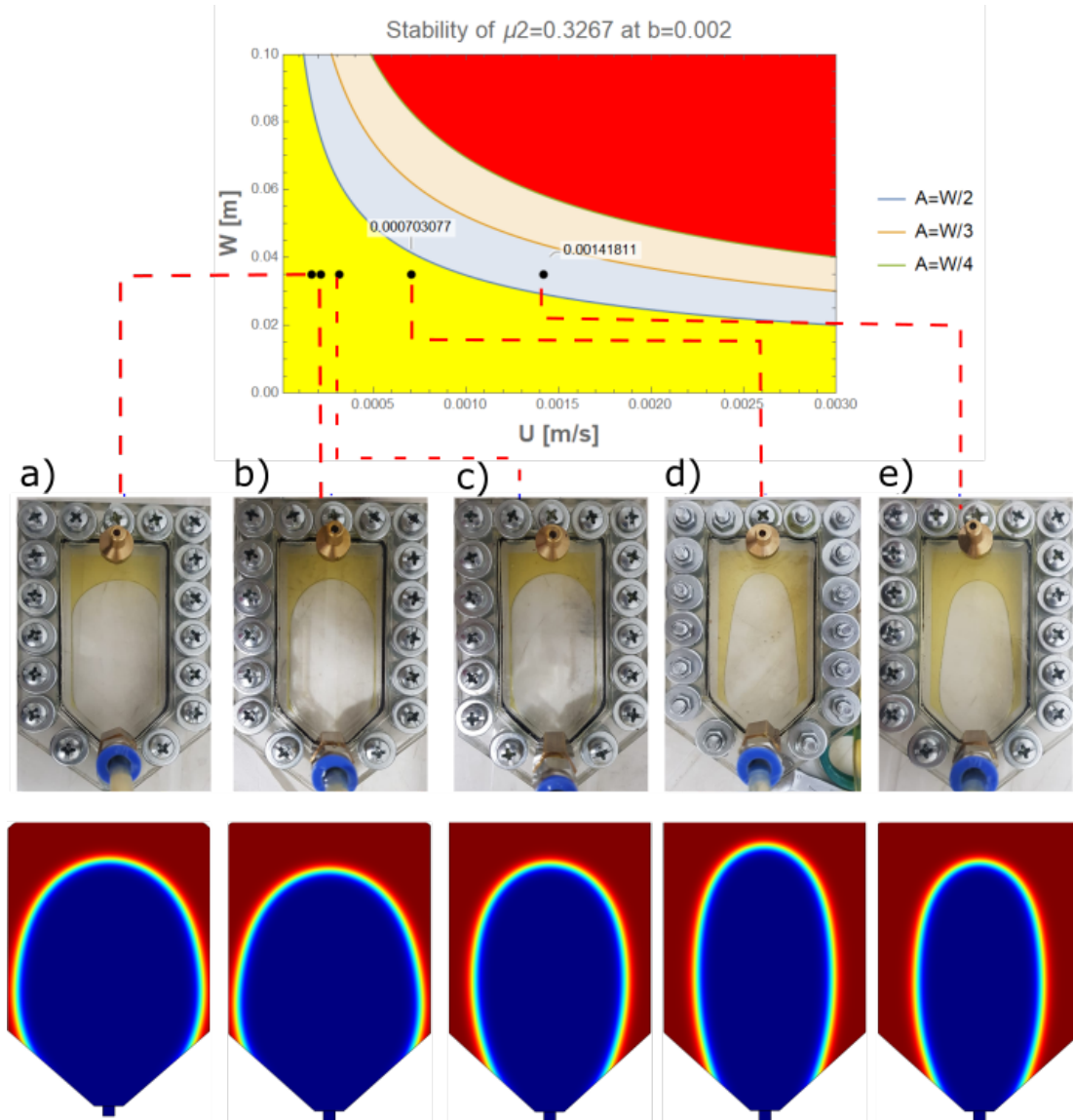
Figure 6.3: Experimental results for b=2mm cell. The dots are the experimental values used, these are mentioned in Tab. 6.5. The graph corresponds to the stability map for b=2mm. The first row under the stability map shows the experiments performed at Yachay Tech, maintaining all the parameters constant except by the input velocity using the cell height b=2mm. The second row shows the simulations of the fluid displacement made with COMSOL Multiphysics. The red part of the simulation is the displaced oil, and the blue one is the water forming the fingers.

In the experiment, the cases a), b), and c) are stable fronts of the size of the cell width, while the cases d) and e) are wide fingers. Again, the fourth case is in the stable region, but does not converge to the cell width, nor to $\lambda = 1/2$. It is possible that because of the length of the cell, the finger has not achieved its final width, which could be wider. Recall that this region allows perturbations between $A = W$ and $A = W/2$, so it still is a good result. The last point (e) hits the blue region. This point is supposed to converge at $\lambda \rightarrow 1/2$, but it seems to be wider. Close to the input, the finger is wider than at the tip. The fluid interaction with the walls makes the interface attach to the walls at the beginning, stabilizing the front. This stabilization geometry may me the reason for the finger to be wider than the expected since the theory does not account for this interaction.

In the simulations, the structures look qualitatively similar to the experiments, but there is a noticeable difference in the case c). In the experiment, we see a very stable front that is even of the size of the cell width. The simulation by the contrast shown a finger which is no longer attached to the walls, leading to a wide finger instead a of stable front. This may be due to wall-interaction effects neglected in the simulation. As mentioned in Chapter 5, we are avoiding to include wetting effects on the walls. The wettablity of the fluids provide an interaction force that maintains the fluids attached to the walls. Apart from this difference, the other structures coincide very accurately between simulation and experiment.

In Appendix D we can see a complementary experiment that shows the actual size that the fingers in the simulation should have in the short term. There, we see that our fingers seen in Fig. 6.3 have not converged yet. Just to figure out some examples, the plot case (c) converges to $\lambda = 0.8247$ if we let it flow for 240s. In the data portrayed at Tab. 6.6, the relative finger width was $\lambda = 0.766$ for the simulation, and $\lambda = 0.963$ for the experiments. Then, the finger obtained from the simulation has not converged to its final width. In the Appendix D, we can also see the plot case (e) left to run for 80 seconds in Fig. D.4, the one that converges at $\lambda = 0.64$, which is more proximate to the experimental value seen in Tab. 6.6 for the same case. Also, the experiment has not converged either. If we let the system to run longer, it would be much more probable that both approaches, simulation and experiment turn out to coincide at similar finger widths.

Finger Width

In Table 6.6 and Fig. 6.4 it is evident that the relative finger width for the simulation is notably smaller than the relative finger width for the experiments. Actually, the absolute difference between both approaches are around 0.1 and 0.2. This error is no longer negligible. It would represent that the simulation results are 0.1 to 0.2 times the cell width smaller than the experimental values. Therefore, for this aspect ratio, our simulation is not so accurate with respect to the experiment, but it is not invalid either. The points do not even coincide within the same range of errors as evidenced in Fig. 6.4, but they do not have to coincide. Lets remember that there are different physical effects that occur in the actual experiment and are not considered in the simulation. One of the most important of these effects are the transverse curvature of the displaced interface and wetting effects. The transverse curvature increases the pressure jump of the system, making the fingers move faster. On the other hand, wetting effects act like a dragging force for the fluid displacement. The fact that the experiments turned out to be more stable than the simulations imply that wetting forces are dominant in this aspect ratio (W/b = 35/2).

Table 6.6: Finger width comparison between experimental and computational approaches at b=2mm.

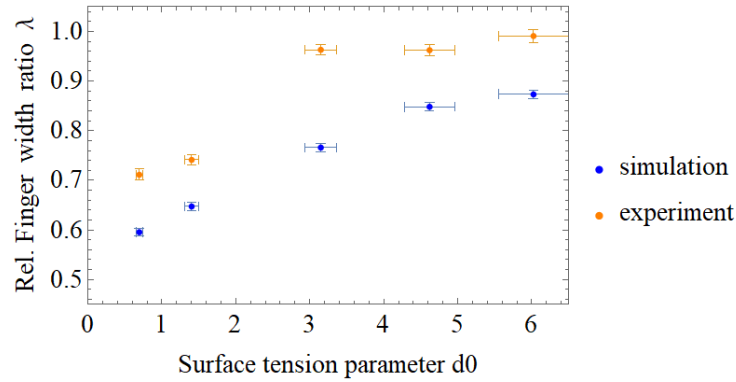| Cell Height [m]	Front Velocity [m/s]	d0	Rel. Finger Width (Simulation)	Rel. Finger Width (Experiment)	Rel. Finger Difference	Plot Case
b=0.002	0.000163757	6.02385	0.873273	0.990783	0.11751	a
	0.000213571	4.61882	0.848242	0.96238	0.114138	b
	0.000313271	3.14886	0.766078	0.963059	0.196981	c
	0.000703077	1.40304	0.6474	0.741264	0.093864	d
	0.00141811	0.695606	0.595548	0.711286	0.115738	e

Figure 6.4: Relative finger width at b=2mm. This graph depicts the comparison between the experimental and computational results for the displacement of a more viscous fluid with a less viscous one at the aspect ratio W/b=35/2. The blue dots represent the experimental results, while the orange ones represent the simulation.

Characteristic time

In Tab. 6.7 we see that the only positive value corresponds to the perturbation of size A=W/2, for the plot case (e). This means that this configuration is the only one that will actually be allowed to grow a finger of relative width $\lambda \rightarrow 1/2$. According to the characteristic time, the instability should be visible after t≈13s. The experiment and the simulation were left to run for approximately 30s. In that time, the fingers did not converged to 1/2. In an attempt to solve this inquiry, in the Appendix D we let the fluids flow developed in a micro-cell of submitted to the same conditions, except by the length, which is much longer than the used in our studies. The finger was left to run by 180s and converged at λ=0.64. Hence, the experiments and simulation agree qualitatively with the analysis, but quantitatively, there are physical assumptions ignored in the analysis that could be affecting the behavior of the systems and we are not considering.

Table 6.7: Characteristic time at b=2mm.

Cell Height [m]	n	Amplitude [m]	Front Velocity [m/s]	Char. time [s]	Plot case
b=0.002	1	W/2	0.000163757	-6.77097	a
			0.000213571	-7.20738	b
			0.000313271	-8.27482	c
			0.000703077	-19.6577	d
			0.00141811	12.9045	e
	3/2	W/3	0.000163757	-1.80645	a
			0.000213571	-1.85131	b
			0.000313271	-1.94814	c
			0.000703077	-2.44892	d
			0.00141811	-4.63394	e
	4	W/4	0.000163757	-0.736431	a
			0.000213571	-0.746261	b
			0.000313271	-0.766743	c
			0.000703077	-0.858913	d
			0.00141811	-1.10188	e

6.1.3 Results for cell depth b=1mm.

Table 6.8: Experimental conditions for b=1mm.

Cell Height [m]	Screw	Input Velocities [m/s]	Front Velocities [m/s]	Plot Case
b=0.003	1	0.0057315	0.000327514	a
	2	0.007475	0.000427143	b
		0.0109645	0.000626543	c
	3	0.0246077	0.00140615	d
		0.049634	0.00283623	e

In Fig. 6.5 we see that all of the experimental values hit at least one instability region. In Tab. 6.9 we see that the values of the surface tension parameter d_0 are all less than 1. This implies that for all the possible cases we should see fingers in the displacements. This is evidenced in both, experiment and

simulation, as shown in Fig. 6.5. For the case (a) and (b), we should visualize at most, a finger that converges to an instability of $\lambda \rightarrow 1/2$. For the case (c), we should evidence the first instability mentioned, but this point hits the orange zone, which means that we could expect to see a bifurcation in the finger that leads to an amplitude of $A = W/3$. For the last cases (d) and (e), given that they are away from all instability frontiers in the map, we should be able to see all the instabilities mentioned. In both, our experiments and simulations, we do not evidence any instability higher than $\lambda \rightarrow 1/2$. The first three cases show a clear finger structure but they do not converge at W/2, neither do we see a bifurcation. According to the stability analysis made in section 3.2, a stability line is the limit where a front can be unstabilized by perturbations of equal or smaller amplitudes than a given amplitude. In this context, once we cross the instability line, in the case (c), structures of amplitudes greater than $A = W/3$ should not be visualized. The same for the last two cases, that are deep into the instability region, crossing the instability line of $A = W/4$. For these points, a perturbation of the size of half cell should not be allowed. In the case of point (c), this behavior can be considered to be due to the fact that the point is almost above the instability line, such that it could be in a transition region, or the flow time has not being enough to let the instability develop. However, the points (d) and specially (e), are far from the instability line, such that the behavior should be evident. The fact that again, the experiments and the simulation are more stable than the predicted by the stability criteria imply that there is a stabilization effect in both approaches that is not considered in the stability analysis.

All of the structures obtained are similar for the experimental and computational model. For this aspect ratio (W/b=35/1), the fingers obtained in the experiment reach the instability faster than the simulations, but in general, both approaches seem to coincide very well.
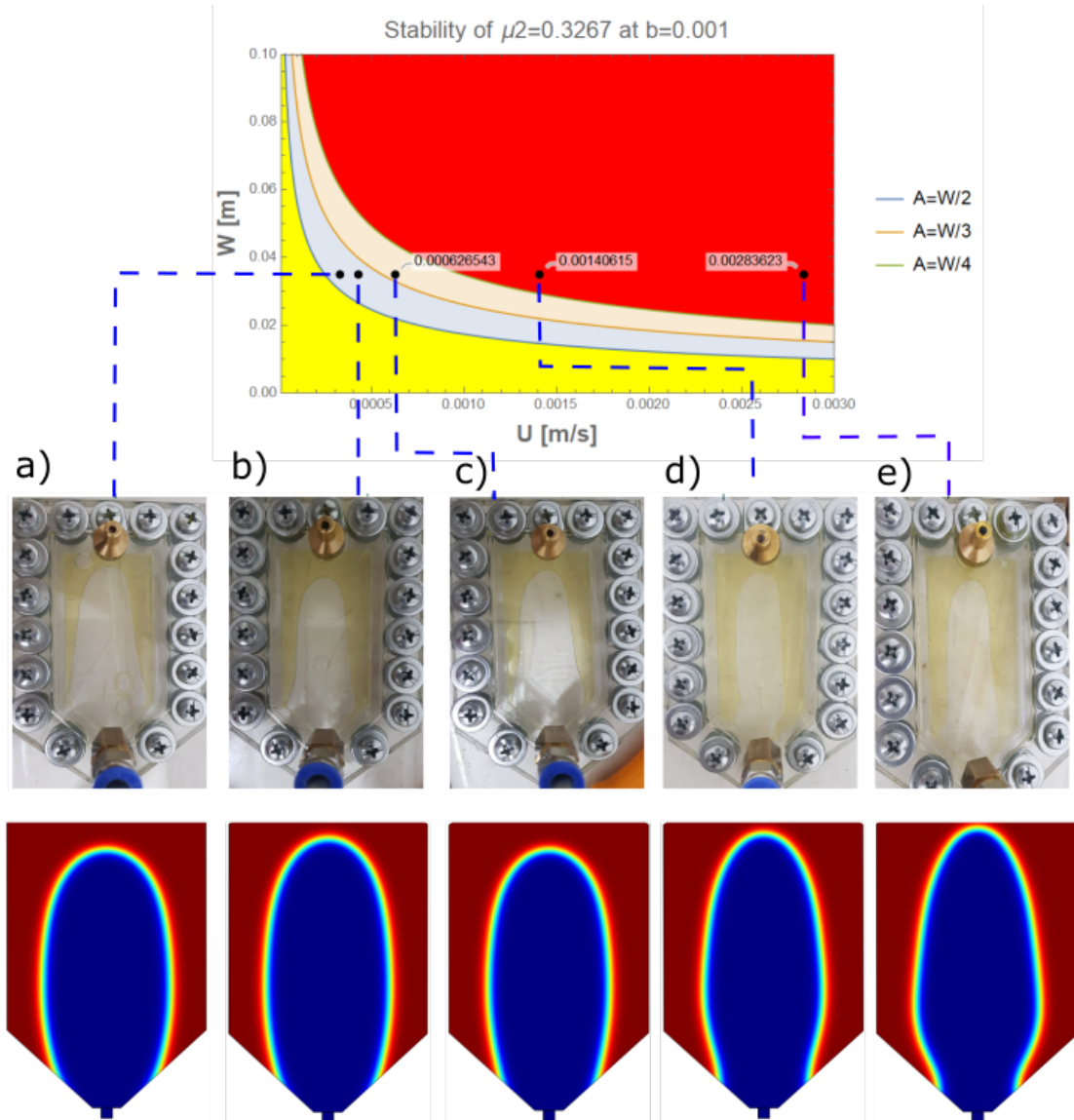
Figure 6.5: Experimental results for b=1mm cell. The dots are the experimental values used, these are mentioned in Tab. 6.8. The graph corresponds to the stability map of b=1mm. The first row under the stability map shows the experiments performed at Yachay Tech, maintaining all the parameters constant except by the input velocity using the cell height b=1mm. The second row shows the simulations of the fluid displacement made with COMSOL Multiphysics. The red part of the simulation is the displaced oil, and the blue one is the water forming the fingers.

Finger width.

The relative finger widths of the simulation are greater than the experimental results. Hence, the simulation takes more time to converge to an unstable behavior than the experiments. Differently from the aspect ratio (W/b=35/2), where the experiments were more stable than the simulations. Due to the shape of the pressure jump equation for three dimensional contributions, 3.74, the smaller the cell depth (b), the higher the pressure jump. This implies that the fingers in the experiment tend to move faster than the ones in the simulation. As previously discussed, the experiment also counts on the contribution of dragging, wetting effects, but as evidenced at this aspect ratio, the contribution of the transverse curvature is higher.

The absolute difference in relative finger widths between both approaches is negligible. They even follow the same general shape. For this aspect ratio, in Fig. 6.6 we clearly evidence the same behavior, which leads us to say that the simulation accurately represents the experiments. Still, as discussed previously, the simulation takes longer to converge at the stable / unstable behavior than the experiments. In this case, it takes longer to get to the unstable behavior, being this the reason for the upward displacement of the simulation points in Fig. 6.6, that seem to show a more stable behavior than the experimental ones.

Once again, following the premise that the simulation and experiment accomplish to be in a good range of agreement, in the Appendix D we show a predictive plot of how the system should behave if we let it run for longer times. In Fig. D.5, we see the simulation for the plot case (e) of this aspect ratio. There, the finger converges at λ =0.55. Hence, as previously noted, due to the extra physical contributions present in the experiment, it will tend to converge faster to an unstable finger of λ =1/2. But the point is that it will eventually converge. The results in the mentioned appendix allow us to say that both, the simulation and the experiments have not been left enough time to let them reach their final width.

Actually, for cases d) and e) we should be able to see up to a tip splitting where each tip converges at the width of λ =1/4. We do not visualize any instability further than single finger formations. The reason for this behavior is no longer linked to the time duration of the experiments, given that we already saw that even at the more unstable case, when letting it run for longer times, it does not split or change the behavior. In both cases, simulation and experiment, we do not evidence higher order instabilities. Thus,

we can neglect the fact that the three dimensional contributions are the ones that are affecting the behavior of the system. In consequence, the difference between the obtained behavior and the expected one relies on the geometry of the system. Recall the fact that our stability analysis was made under the assumption that the initial state is a flat interface, from where we begin to induce perturbations A(t). Our experiments and simulations do not begin at a flat interface, besides, the triangular shape of the input helps to stabilize the front by the interaction with the walls. Still, even if we do not achieve to get to the exact amplitudes desired, the results are qualitatively correct, meaning that at least we were able to predict when a displacement will show finger formations.

Table 6.9: Finger width comparison between experimental and computational approaches at b=1mm.

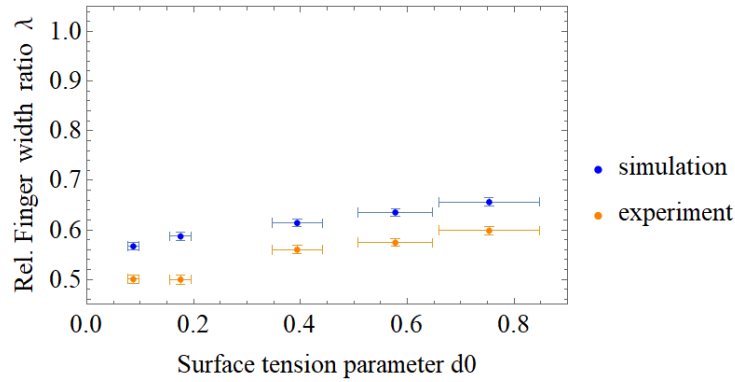| Cell Height [m]	Front Velocity [m/s]	d0	Rel. Finger Width (Simulation)	Rel. Finger Width (Experiment)	Rel. Finger Difference	Plot Case
b=0.001	0.000327514	0.752981	0.656194	0.598545	0.057649	a
	0.000427143	0.577353	0.635324	0.574491	0.060833	b
	0.000626543	0.393608	0.614118	0.560282	0.053836	c
	0.00140615	0.175381	0.587023	0.5	0.087023	d
	0.00283623	0.0869507	0.567036	0.500828	0.066208	e

Figure 6.6: Relative finger width at b=1mm. This graph is the comparison between the experimental and computational results for the displacement of a more viscous fluid with a less viscous one at the aspect ratio W/b =35/1. The blue dots represent the experimental results, while the orange ones represent the simulation.

Characteristic time

In Tab. 6.10 we see many positive values, which indicate that many instabilities are allowed to exist for this aspect ratio. Even so, in our experiments and simulation we are only able to visualize first order instabilities (A=W/2). For cases (a) and (b), only first order perturbations are allowed to occur, meaning that we should see a finger that converges to $\lambda \rightarrow 1/2$ in 69s for case (a), and 30.1s for case (b). In our experiments and simulation we only left the system to flow for 30s in case (a), and 25s in case (b). In both cases it is actually evident that the fingers have not converged to their final width, which can now be confirmed that the cells need to be longer by means of having more time for the instabilities to develop. The characteristic times indicate that the closer a point is to the instability line, the longer it will take to develop the instability. Consequently, the first cases submitted to lower velocities take longer to show the instabilities. As previously discussed, this study was made under the assumption that a flat front is perturbed by the described amplitudes, the fact that we do not evidence the other higher order instabilities could be related to the stabilization of the front by the triangular shape of the input, the one that could be flattening small amplitudes due to the interaction of the liquids with the walls. Furthermore, it is important to consider that our initial front is not flat, but it is curved.

Table 6.10: Characteristic time b=1mm.

Cell Height [m]	n	Amplitude [m]	Front Velocity [m/s]	Char. time [s]	Plot case
b=0.001	1	W/2	0.000327514	68.8539	a
			0.000427143	30.8558	b
			0.000626543	14.6617	c
			0.00140615	4.80399	d
			0.00283623	2.15106	e
	3/2	W/3	0.000327514	-16.3334	a
			0.000427143	-29.0729	b
			0.000626543	51.8188	c
			0.00140615	4.36241	d
			0.00283623	1.62781	e
	4	W/4	0.000327514	-4.22684	a
			0.000427143	-4.97976	b
			0.000626543	-7.73872	c
			0.00140615	6.63611	d
			0.00283623	1.5057	e

6.1.4   Finger Width comparison

In this section we will analyze the width of the fingers with respect to the cell width. Using the method described at section 4.4.2, we determined the desired data for each aspect ratio. Then, we will plot the relative finger widths for each data available for both, experiment and simulation. Our interest is to compare this results to the surface tension parameter d_0. Remember that this parameter is the one that tells us about the behavior of the system. Not only that, but more specifically, this parameter tells us about the amplitudes of the perturbation to which the system could converge according its conditions. In the section 4.5 we already mentioned that fingers where $d_0 < 1$, tend to converge to relative fingers smaller than $\lambda = 1/2$. For $d_0 < 4/9$ will be perturbed by amplitudes equal or smaller than $A = W/3$ (it could appear a finger splitting). For $d_0 < 1/4$, perturbations of amplitude $A = W/4$ could appear, meaning that we could expect tip splitting, where each tip is of size $\lambda = 1/4$.

In Fig. 6.7, there is the whole picture of the results obtained by the computational and experimental
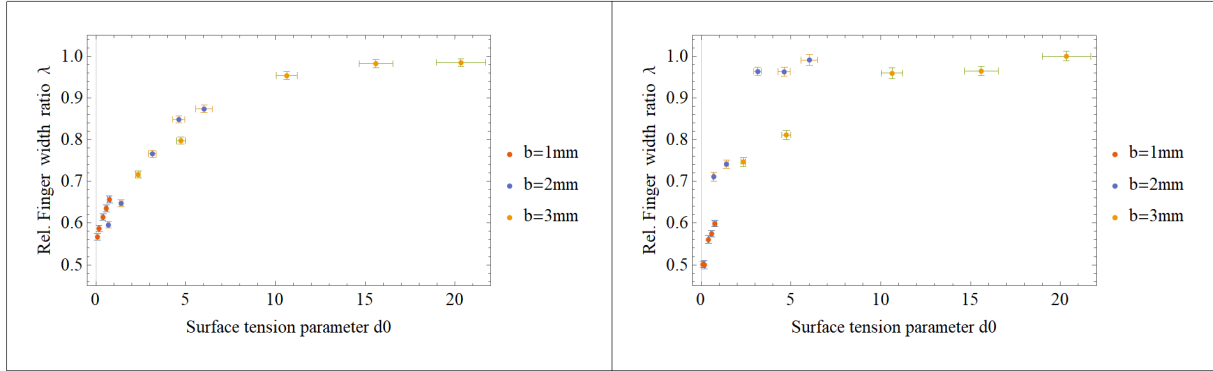
Figure 6.7: Computational vs. experimental relative finger width λ according to the surface tension parameter d_0. The plot on the left corresponds to the behavior of the simulations made on COMSOL Multiphysics. The plot on the right corresponds to the experimental data obtained.

approach. In the case of the simulation, the results are very well arranged in an approximately square-root-like behaviour as depicted by McLean and Saffman[20], and Tabeling[44]. In the case of the experiment, as expected, it is not so well arranged, but we can still evidence a similar relationship between the finger width and the surface tension parameter. In terms of stability, it seems to be that the simulation is more stable than the experiment. Here, we mean that the rate of change between a stable and an unstable regime occurs faster for the experiments. The experimental curve is flat at values close to λ=1 (stable regime), and then it rapidly drops to smaller relative finger widths as $d_0 \rightarrow 0$. Instead, in the simulation, the relative finger width decreases smoothly as the surface tension parameter decreases as well. As discussed in the previous sections, it seems to be like there is an interplay between wetting and pressure jump in the experimental approach. Wetting effects tends to stabilize the displacement, while the increase of the pressure jump unstabilize the front due to the increase in velocity. In the experiments, one can not neglect the contribution of the transverse radii of curvature of the interface (b/2)[12]. The smaller the cell depth (b), the higher the pressure jump in a real system[20]. The contribution of the pressure jump predominates over the wetting effects as the cell depth decreases. In other words, the system tends to unstabilize faster as the cell depth decrease, making the curve more pronounced. By the contrast, the simulations do not count on

any of these physical contributions.

It is said that the simulation is more stable than the experiment not just because of the shape of the curve, but because of the size of the fingers. In the simulation, the fingers at the most unstable point does not reach $\lambda = 1/2$, but it stays around $\lambda = 0.65$. In contrast, the most unstable point of our experiments actually reached $\lambda = 1/2$. This is another argument to say the experiment converges faster than the simulation to the expected behavior. The last statement agrees accurately with the theoretical analysis. In section 3.5, our three dimensional surface tension parameter d_1 is greater than the 2D surface tension parameter d_0, meaning that it is easier to reach an instability under the effect of a transverse curvature in the fingers. This behavior is also evidenced in the Appendix C, where we see a graphical comparison between the behavior of the system under the 2D and 3D stability analysis, and the curves for the 3D analysis are displaced downwards with respect to the 2D analysis, meaning that the points affected by a transverse curvature will tend to reach faster to the studied instabilities.

6.2 Predicted displacement of a flat interface

In the previous results it was evidenced the correspondence between the experiments and the simulation. The computational model showed to reproduce very well the experiments with great accuracy. Even when both approaches failed to show the instabilities proposed by the stability analysis, there was high concordance in the behavior between the approaches. Using the fact that the computational model could very accurately represent an experimental situation, we can be confident to simulate the same two-phase flow system under different geometries. The results may present a slight difference in the stability, where the experiments tend to converge faster into an unstable behavior. Still, these results will allow to have a close idea of the behavior of the fluid interactions before proceeding to build an experimental set-up.

In the past sections, the main discussion lead to the conclusion that the difference between the behavior of the computational-experimental approach with the theoretical analysis could be closely related to the shape of the initial interface and the shape of the input walls. Hence, in this section a new geometry is proposed. In the stability analysis developed in section 3.2, the first assumption comes from the fact that

there is a flat interface flowing at a constant velocity, and then a small bump or perturbation A(t) grows. Thus, here it is presented a new geometry, the one that departs from a flat interface as seen in Fig. 6.8. Also, the micro-model has been extended to L=20cm to led the fluids interact for longer time periods, such that they can reach the convergence at a fixed amplitudes.

Figure 6.8: Flat interface geometry. The blue portion corresponds to water, the red portion is oil. The flow goes from left to right.

Using the exact same experimental conditions than in the previous study, in the following section it is found the result of the simulations for this new geometry in terms of the stability maps, finger shapes and characteristic times.

Results for b=3mm.

In Fig. 6.9 we see the resulting displacement patterns for the same experimental conditions previously discussed. Thus **plot cases** also correspond to the same conditions, but now they show different patterns because of the change in geometry. This result is much more accurate with respect to the stability map than the ones made with the last geometry. Here, again we see that all the experimental points hit the yellow region, where it is expected to obtain very stable displacement fronts, meaning flat fronts or wide fingers. That is exactly what we observe from the simulations performed. The first two plot cases (a) and (b) are very stable flat fronts, the third one is curved but is still of the size of the cell width, and the last two already show finger formation.

In Tab. 6.11 we see that these cases actually converge at $\lambda \rightarrow 0.853$ and $\lambda \rightarrow 0.749$ respectively. The surface tension parameter d_0 is greater than 1 for all the cases, which implies an stable front of an amplitude greater than A=W/2. Thus, it coincides very well with the theoretical analysis because all the patterns

Table 6.11: Relative finger width for b=3mm.

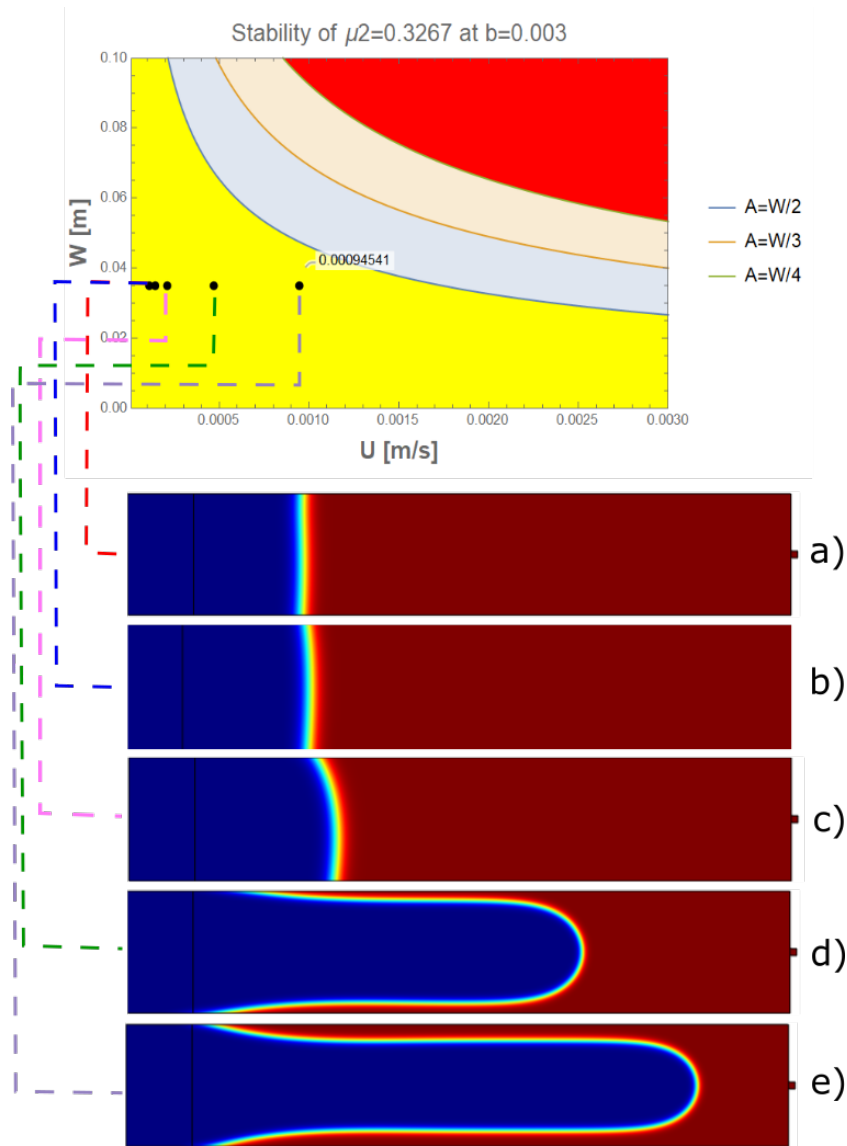| Cell depth [m]	Front Velocity [m/s]	d0	Rel. Finger Width (Simulation)	Plot case
b=0.003	0.000109171	20.3305	1	a
	0.000142381	15.5885	1	b
	0.000208848	10.6274	1	c
	0.000468718	4.73528	0.853	d
	0.00094541	2.34767	0.749	e

observed are greater than $\lambda = 1/2$.

Figure 6.9: Results for simulation of fluids interacting through flat interface at b=3mm. The graph corresponds to the stability map of b=3mm. The flow patterns shown bellow correspond to each experimental condition stated by the black dots in the stability map.

Results for b=2mm

For this aspect ratio (W/b = 35/2), the stability map suggests that the first four cases of slower velocities hit the stability region, meaning that flat fronts, fingers of size of the cell width, or fingers of amplitudes greater

than $\lambda = 1/2$. Instead, the last point, meaning plot case (e), hits the blue region of the stability map, which should lead to the formation of finger that converges at $\lambda \to 1/2$. In the results for the simulations evidenced at the same Fig. 6.10, we see that the fingers coincide very accurately with the stability map. Indeed, all the cases coincide to the behavior described by the stability map and the surface tension parameters d_0 shown in Tab. 6.12. Given that $d_0 < 1$ for the case (e), we should expect to evidence a finger of half of the cell width. In the simulation, we see a very pronounced finger that converges at $\lambda = 0.619$. We should expect to see an even thinner finger, but considering the fact that the point (e) is very close to the instability line, it may be required to be deeper into the instability region to actually evidence a finger of width closer to $\lambda = 1/2$.

Table 6.12: Relative finger width for b=2mm.

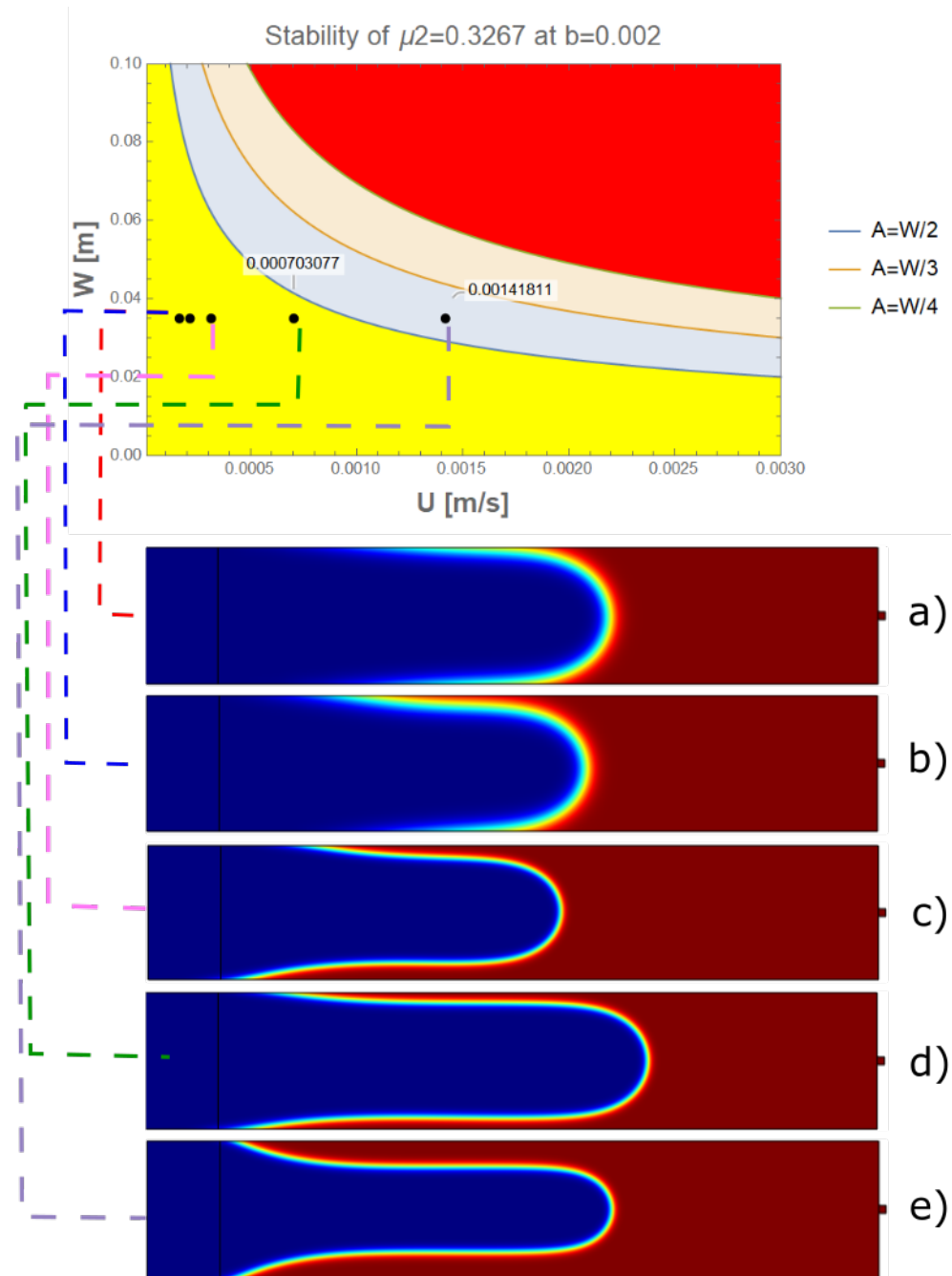| Cell depth [m]	Front Velocity [m/s]	d0	Rel. Finger Width (Simulation)	Plot case
b=0.002	0.000163757	6.02385	1	a
	0.000213571	4.61882	0.923	b
	0.000313271	3.14886	0.779	c
	0.000703077	1.40304	0.849	d
	0.00141811	0.695606	0.619	e

Figure 6.10: Results for simulation of fluids interacting through flat interface at b=2mm. The graph corresponds to the stability map of b=2mm. The flow patterns shown bellow correspond to each experimental condition stated by the black dots in the stability map.

Results for b=1mm.

For this aspect ratio (W/b=35/1), the points hit different instability regions and the surface tension parameters d_0 is less than 1 for all the experiments. Therefore, we should be able to evidence all the studied instabilities, A=W/2, W/3, W/4, where the last two imply finger splitting. In Fig. 6.11, the points (a) and (b) for this aspect ratio hit the zone where we should expect a finger of width that converges at $\lambda \rightarrow 1/2$. In the same way that seen in the case (e) of the aspect ratio W/b=35/1, the fingers seen are thin but they do not converge at 1/2, but they converge at 0.633 and 0.6213 respectively. In the case of the case (c), the point hit the region from where it should begin to split and converge into A=W/3. We do not see the splitting, but we evidence a single finger that converges at 0.5976, but we have to consider that the point is almost above the instability line, so we may need it to be deeper into the instability zone in order to actually evidence this behavior. Finally, the cases (d) and (e) qualitatively correspond very well to the stability map. For these last cases we expect the displacement to be split into two fingers that converge at $\lambda = 1/4$ each. The results for the simulation seen in Fig. 6.11, show that we the behavior of the fingers agree with the stability map, in both cases the interface is divided in two fingers. In Tab. 6.13, for cases (d) and (e) there are two values at the correspondent cell of the *relative finger width*, these values are the relative width of each finger grown in the displacement. For the case (d), the fingers have a relative width of 0.275 and 0.3, meaning that this is actually a kind of transition regime between the instability caused by a perturbation of amplitude A=W/3 and A=W/4. Finally, for the case (e), the relative finger widths are 0.265 and 0.268, which are very approximate values to $\lambda \rightarrow 1/4$.

Table 6.13: Relative finger width for b=1mm.

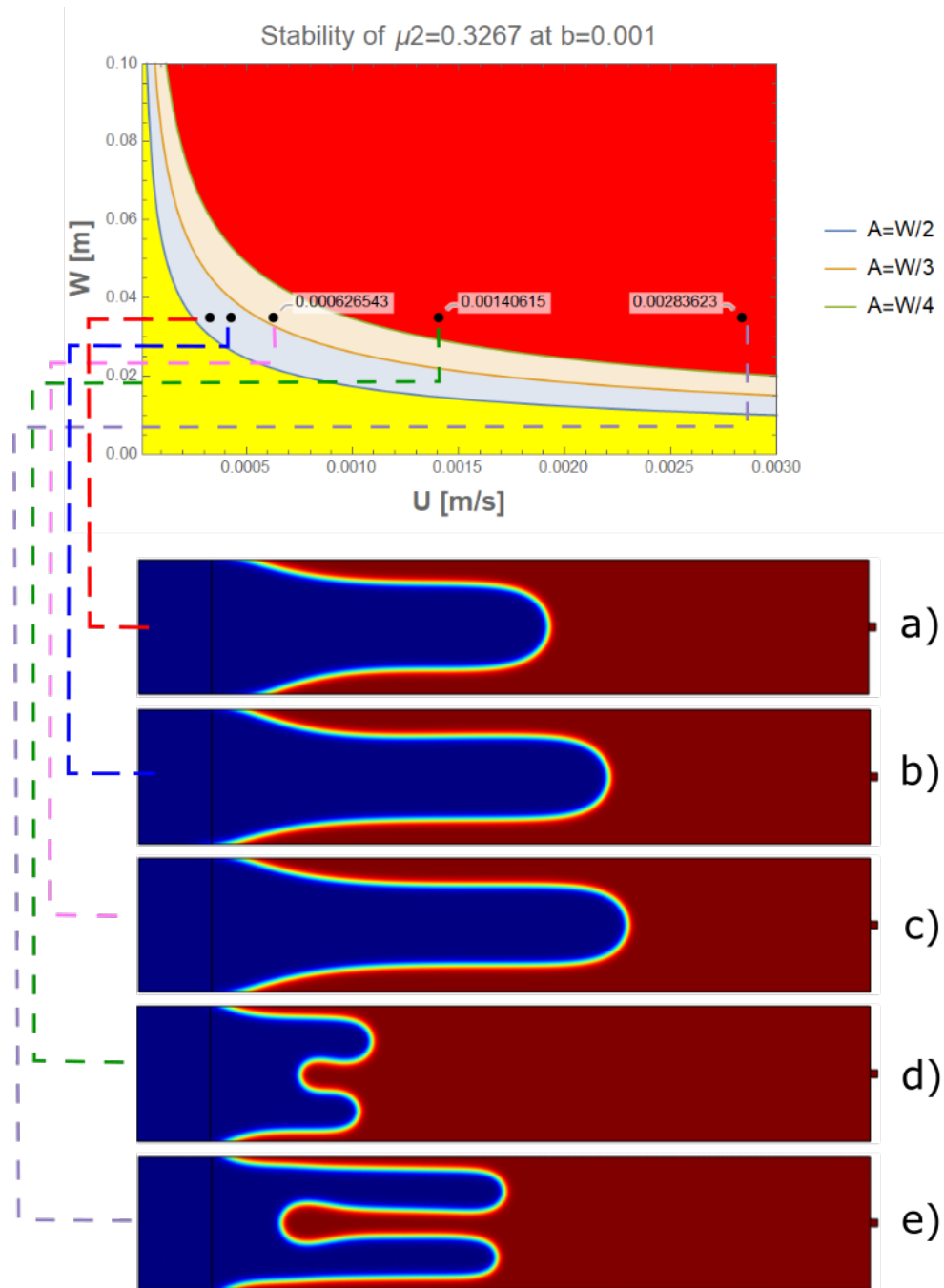| Cell depth [m]	Front Velocity [m/s]	d0	Rel. Finger Width (Simulation)	Plot case
	0.000327514	0.752981	0.633	a
	0.000427143	0.577353	0.6213	b
b=0.001	0.000626543	0.393608	0.5976	c
	0.00140615	0.175381	0.275 - 0.3	d
	0.00283623	0.0869507	0.265 - 0.268	e

Figure 6.11: Results for simulation of fluids interacting through flat interface at b=1mm. The graph corresponds to the stability map of b=1mm. The flow patterns shown bellow correspond to each experimental condition stated by the black dots in the stability map.

6.3 Summary

Summarizing the results:

- The stability criteria developed analytically requires the initial interface to be strictly flat in order to accurately predict instability regions.

- The initial geometry proposed for the micro-models provide stabilizing effects to the fluid flow.

- The initial geometry is not long enough to let the displacement structures to develop completely.

- In the experimental flows there is an interplay between wettability and pressure jump. The smaller the cell depth, the higher the contribution of pressure jump. This makes the system reach faster to an unstable behavior in comparison to simulations under the same condition.

- In the simulations, the pressure jump is independent of the cell height, maintaining the rate at which the instabilities tend to form.

- Under the studied conditions, the computational model has proved to be accurate enough to reproduce and predict experimental fluid flows.

Chapter 7

Conclusions & Outlook

The goal of this research project was to propose a stability criteria to predict the behavior of Saffman - Taylor instabilities in a system of a less viscous fluid pushing a more viscous one. Furthermore, to develop a computational model that allows to simulate the expected behavior of this systems in order to use it in further works.

These objectives were accomplished by the use of the surface tension parameter d_0 as a control parameter to construct stability maps. The stability maps define the regions where different perturbations could show-up according to the experimental conditions. In order to complement the stability analysis, the finger width relation to the surface tension parameter and the characteristic time were used to explain the behavior of the flow patterns in deeper detail than just a qualitative description of the finger formation.

The experiments and simulations performed were proven to coincide with high accuracy, bearing in mind the fact that the experiments still tend to reach unstable patterns faster that the simulations. The stability criteria fails to describe the behavior of a displacement where the input flow has a curved interface.

The accuracy of the proposed computational model was confirmed through the comparison with the experiments performed. The model was used to simulate a set-up where the initial interface is flat and the input is uniform along the whole cell width. The theoretical stability analysis turned out to precisely predict the behavior of the interaction between viscous fluids under the strict condition that the initial

interface must be flat.

Hence, we achieved to establish a stability criteria that allows to play with the main parameters of the cell shape and the fluid properties in order to find the most suitable conditions where we could expect to see stable or unstable behaviors as desired.

More than a concluding research project, this thesis has achieved to settle the theoretical, experimental and computational foundations to open a new research field at Yachay Tech University. The stability criteria and the computational model are time and resource saving features of high relevance for future works. The stability criteria will allow to settle the conditions for the experiments or simulations to be developed according to the desired behavior. The computational model can be used to simulate the flow under new conditions or a new geometry proposed, as long as the initial interface is flat. Also, we could simulate good approximations to flow patterns that are not necessarily a flat interface, but in this case we can not guide our results on the expected behavior proposed by the stability criteria. In general, these studies can be easily performed to suggest new stabilization conditions before building experimental set-ups.

Now that we have understood the problem, for *future works* we expect not only to understand the system, but to suggest new stabilization criterion to change behavior of the flow in order to stabilize the displacement fronts. In that way, by damping viscous finger formations, techniques for improving oil extraction processes through water-flooding can be developed.

Furthermore, we would like to keep improving the stability analysis. By now, the analysis is based on simple assumptions of the fluid flow, but it has still shown to give an approximate idea of the behavior of the system. For *future works* we would like to introduce three-dimensional contributions as briefly introduced in the thesis, contributions like wetting interactions, transverse front curvature between other effects, not only to the analysis but also to the computational model. The next step to improve the stability analysis is to study the behavior of fluids interacting under the presence of a curved interface instead of a flat one.

Appendix A

Crude oil data.

The following table shows a compilation of different crude oils, their properties differ according to their location. Here we can find the viscosity in cp and the interfacial tension (IFT) between water and the correspondent crude oil.

Field	Oil Formation	Location	Oil Viscosity (cp)	IFT (dynes/cm)
West Delta	Offshore	Louisiana	30.4	17.9
Cayuga	Woodbine	Texas	82.9	17.9
Fairport	Lansing	Kansas	5.3	20.8
Bayou	Choctaw	Louisiana	16.1	15.6
Chase-Silica	Kansas City	Kansas	6.7	19.6
Hofra	Paleocene	Libva	6.1	27.1
Black Bay	Miocene	Louisiana	90.8	17.7
Bar-Dew	Bartlesville	Oklahoma	9.0	21.4
Bar-Dew	Bartlesville	Oklahoma	6.8	21.4
Eugene Island	Offshore	Louisiana	7.4	16.2
Cambridge	Second Berea	Ohio	15.3	14.7
Grand Isle	Offshore	Louisiana	10.3	16.1
Bastian Bay	Uvigerina	Louisiana	112.2	24.8

Table A.1: Interfacial tension between water and several crude oil types[1]

Field	Oil Formation	Location	Oil Viscosity (cp)	IFT (dynes/cm)
Oklahoma City	Wilcox	Oklahoma	6.7	20.1
Glenpool	Glen	Oklahoma	5.1	24.7
Cumberland	McLish	Oklahoma	5.8	18.5
Allen District	Allen	Oklahoma	22.0	25.9
Squirrel	Squirrel	Oklahoma	33.0	22.3
Berclair	Vicksberg	Texas	44.5	10.3
Greenwood-Waskom	Wacatoch	Louisiana	5.9	11.9
Ship Shoal	Miocene	Louisiana	22.2	17.3
Gilliand	-	Oklahoma	12.8	17.8
Clear Creek	Upper Bearhead	Louisiana	2.4	17.3
Ray	Arbuckle	Kansas	21.9	25.3
Wheeler	Ellenburger	Texas	4.5	18.2
Ray	Arbuckle	Kansas	21.9	25.3
Wheeler	Ellenburger	Texas	4.5	18.2
Rio Bravo	Rio Bravo	California	3.8	17.8
Tatums	Tatums	Oklahoma	133.7	28.8
Saturday Island	Miocene	Louisiana	22.4	31.5
North Shongaloo-Red	Takio	Louisiana	5.2	17.7
Elk Hills	Shallow Zone	Califonia	99.2	12.6
Eugene Island	Miocene	Louisiana	27.7	15.3
Fairport	Reagan	Kansas	31.8	23.4
Long Beach	Alamitos	Califomia	114.0	30.5
Colgrade	Wilcox	Louisiana	360.0	19.9
Spivey Grabs	Mississippi	Kansas	26.4	24.5
Elk Hills	Shallow Zone	Califonia	213.0	14.2
Trix-Liz	Woodbine A	Texas	693.8	10.6
St. Teresa	Cypress	Illinois	121.7	21.6
Bradford	Devonian	Pennsylvania	2.8	9.9
Huntington Beach	South Main Area	Califomia	86.2	16.4
Bartlesville	Bartlesville	Oklahoma	180.0	13.0
Rhodes Pool	Mississippi Chat	Kansas	43.4	30.5
Toborg	-	Texas	153.6	18.0

Table A.2: Interfacial tension between water and several crude oil types [1]

Appendix B

Error Propagation

In this appendix we will find the error propagation for the measurement of Finger Widths and the calculation of the surface tension parameters in the experiments and simulations.

According to Lindberg[58], the error propagation formula is given by

$$dz = \left(\frac{\partial f}{\partial w}\right)dw + \left(\frac{\partial f}{\partial x}\right)dx + \left(\frac{\partial f}{\partial y}\right)dy + \ldots \tag{B.1}$$

Where $z = f(w, x, y, \ldots)$. For multiplication operations, this expression can be simplified into

$$\frac{\Delta z}{z} = \sqrt{\left(\frac{m\Delta x}{x}\right)^2 + \left(\frac{n\Delta y}{y}\right)^2 + \cdots} \tag{B.2}$$

Where $z = x^m y^n$.

First, the relative finger width λ depends on the finger width and the cell width of each simulation or experiment performed. We will not get into details related to the errors that could show up in the development of the fingers, but we will just focus on the errors related to their measurement. The procedure for the measurement is described in sec. 4.4.2. The error propagation for the relative finger width will be given by

$$\Delta\lambda = \lambda \sqrt{\left(\frac{\Delta W_f}{W_f}\right)^2 + \left(\frac{\Delta W_c}{W_c}\right)^2} \tag{B.3}$$

Where W_f is the finger width, and W_c is the cell width, both measured in pixels from the images taken from the resulting experiments. The uncertainty of both variables is set at $\Delta W_f = \Delta W_f = 2px$ because that is the approximate pixel size of the interface's line in the images.

Regarding the surface tension parameter, the calculus brings higher implications. The surface tension parameter d_0 depends on the front velocity (U), surface tension (T), cell width (W), cell depth (b) and viscosity (μ). The surface tension and viscosity values were extracted from the literature, where no error of measurement was provided, so we will not take them into account. Then, the error propagation for this variable is given by

$$\Delta d_0 = d_0 \sqrt{\left(\frac{\Delta U}{U}\right)^2 + \left(\frac{2\Delta W}{W}\right)^2 + \left(\frac{2\Delta b}{b}\right)^2} \tag{B.4}$$

The uncertainty of the cell width is $\Delta W = 0.0005m$ given that it was measured with a ruler, while the uncertainty of the cell depth is $\Delta b = 0.00005m$ because it was measured with a vernier. The front velocity was calculated from other variables, as described in section 4.3. Thus, we need to calculate its error propagation through

$$\Delta U = U \sqrt{\left(\frac{\Delta v_{screw}}{v_{screw}}\right)^2 + \left(\frac{2\Delta r}{r}\right)^2 + \left(\frac{\Delta W}{W}\right)^2 + \left(\frac{\Delta b}{b}\right)^2} \tag{B.5}$$

Where r is the radius of the piston that contains the fluids, which was measured with a vernier, then $\Delta r = 0.00005m$. The error of W and b were already discussed, and the error of the velocity of the displacement screws must also be calculated through

$$\Delta v_{screw} = v_{screw} \sqrt{\left(\frac{\Delta D}{D}\right)^2 + \left(\frac{\Delta t}{t}\right)^2} \tag{B.6}$$

Where D is the displacement of the movement platform that pushes the content within the cylinder, and

t is the time measured for the displacement. Then $\Delta D=0.00005m$ because it was measured with a vernier, and $\Delta t=0.5s$ because of the approximate time reaction. Once that we have all these calculations done, we can find the total error propagation to be seen in section 6.1.4.

Appendix C

Stability map 2D - 3D

In the same way that we did the stability maps for the quasi-2D analysis, we can use the three dimensional surface tension parameter d_1 to visualize the stability maps under this condition. This last parameter differs from the quasi-2D because because now we consider the contribution of the transverse curvature of the displacing finger. In Fig.C.1 we can see the comparison between the behaviors of the stability maps under different aspect ratios. In general, it is evident that the instability lines slightly displace downwards in the stability map for the 3D case. According to Bensimon *et al.*[12], the transverse curvature has a higher contribution than the in-plane curvature of the finger. Then, it makes the system more unstable, as evidenced in the figure. Hence, for the three dimensional case, the system will tend to converge faster to the desired instabilities.
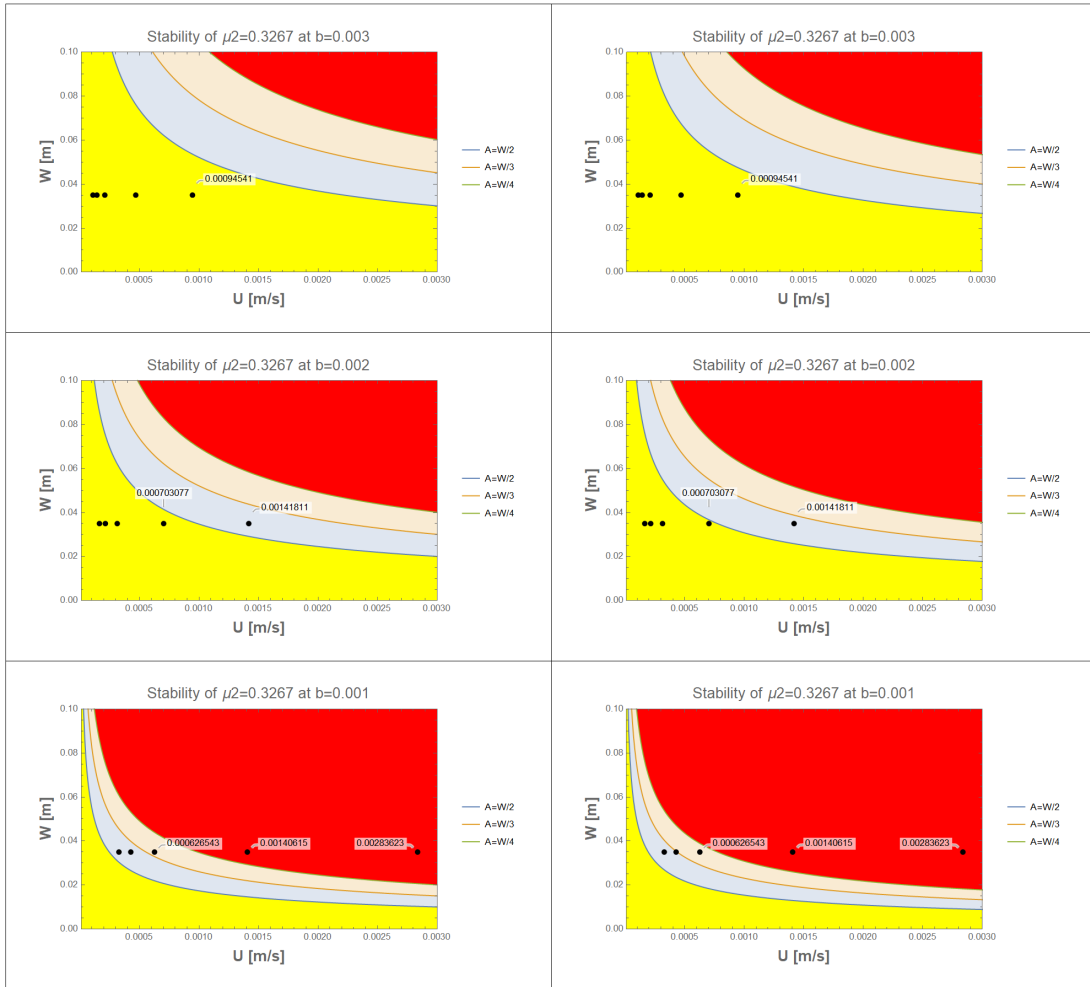
Figure C.1: Stability map 2D - 3D. In the left column we find the stability maps under quasi 2D considerations for b=0.003m, b=0.002m, b= 0.001m. In the right column we find the stability maps under 3D considerations for b=0.003m, b=0.002m, b= 0.001m.

Appendix D

Simulating convergent fingers

In this appendix we will find some complementary results that help us to understand the flow patterns described in Chapter 6. In the mentioned chapter, we saw that the fingers appeared to have ambiguous behaviors, like being in a stable regime but showing a finger-like structure, or being in an unstable regime, but not being of the expected size. Here, we performed longer simulations that give the systems enough time to converge into a constant finger width. The simulation conditions are all the same than the ones described in Chapter 5. The difference relies on the geometry, given that now the cell length is L=0.2m instead of L=0.09m.

Convergence of fingers for b=3mm.

The first case we will see is the plot case c) of the aspect ratio W/b=35/3, visible in section 6.1. In our results, we saw that the experimental conditions for point (c) suggested the flow pattern to be stable (no fingers). In Fig. D.1 we see a finger-like displacement of the size of the cell width. This displacement corresponds very well with the expected behavior described in 6.1, which implies that we have a stable front. The finger converged at λ=0.988.
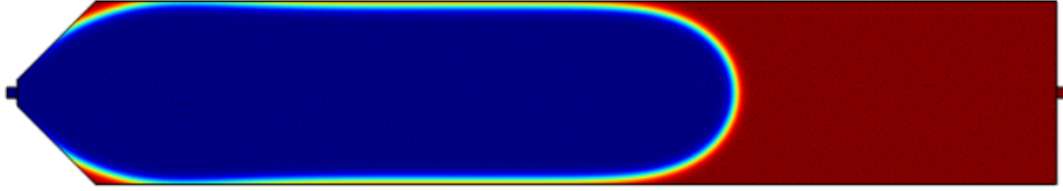
Figure D.1: Simulation of finger structure at b=3mm, plot case c. The blue region is the portion of water in the displacement, the red region is the oil displaced.

The following figure corresponds to the plot case d) of the aspect ratio W/b=35/3. In our results, we saw that the experimental conditions for this points suggested the flow pattern to be stable (no fingers). In Fig. D.2 we see a clear finger that is not of the size of the cell width, but is not either smaller than W/2, which means that it has not crossed to the first instability, meaning that we are still in the stability region (yellow zone of Fig. 6.1). The finger converged at λ=0.87.

Figure D.2: Simulation of finger structure at b=3mm, plot case d. The blue region is the portion of water in the displacement, the red region is the oil displaced.

Convergence of fingers for b=2mm.

The following case corresponds to the finger structure evidenced in the plot case c) at b=2mm evidenced in Fig. 6.3. In Fig. D.3, we see a stable finger that converges to λ =0.8257.

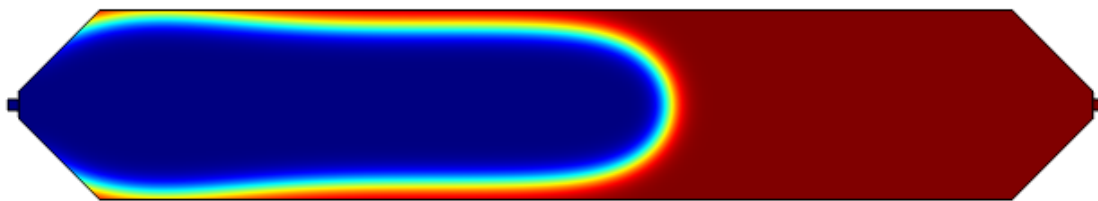Figure D.3: Simulation of finger structure at b=2mm, plot case (c). The blue region is the portion of water in the displacement, the red region is the oil displaced.

The following case corresponds to the finger structure evidenced in the plot case e) at b=2mm evidenced in Fig. 6.3. This point is the highest velocity setting of this aspect ratio (W/b=35/2). In the stability map we were expecting to evidence an instability of first order that converges at λ=1/2. In Fig. D.4 we see that the finger converges at λ=0.64. This does not correspond to the expected instability yet, but given the fact that the stability analysis is made with respect to a flat initial front, the triangular shape of the walls near to the input in our system could be stabilizing the front.
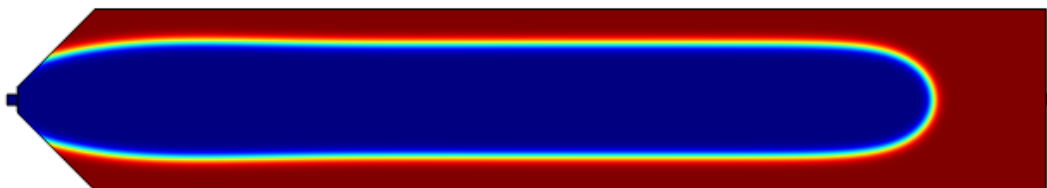

Figure D.4: Simulation of finger structure at b=2mm, plot case e. The blue region is the portion of water in the displacement, the red region is the oil displaced.

Convergence of fingers for b=1mm.

In Fig. D.5 we see the finger of the plot case e) (maximum velocity available) of the micro-model of cell depth b=1mm. In the stability map of this aspect ratio seen at Fig. 6.5, the conditions of this experiments show that we should be able to at least see an instability of first order $\lambda \rightarrow 1/2$, up to a finger splitting of amplitude A=W/4. After leaving the system to run for 35s, the finger converged at λ=0.55.
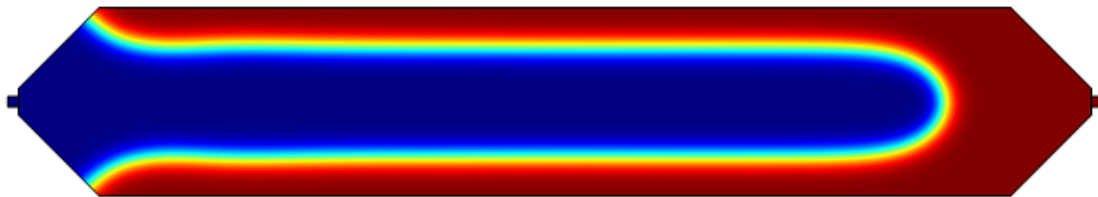
Figure D.5: Simulation of finger structure at b=1mm, plot case e. The blue region is the portion of water in the displacement, the red region is the oil displaced.

Bibliography

[1] Donaldson, E. C.; Thomas, R. D.; Lorenz, P. B. Wettability determination and its effect on recovery efficiency. *Society of Petroleum Engineers Journal* **1969**, *9*, 13–20.

[2] Baghdadi, A. *The numerical modelling of two-phase flows*; Luleå tekniska universitet, 1980.

[3] Alvarado V., M. E. *Enhanced Oil Recovery: Field Planning and Developement Strategies*; Gulf Professional Publishing, 2010.

[4] Millemann, R. E.; Haynes, R. J.; Boggs, T. A.; Hildebrand, S. G. Enhanced oil recovery: environmental issues and state regulatory programs. *Environment International* **1982**, *7*, 165–177.

[5] U.S. Government Energy Information Administration, Petroleum Supply Monthly. 2020.

[6] British Petroleum, Oil: Energy economics: Home. `https://www.bp.com/en/global/corporate/energy-economics/statistical-review-of-world-energy/oil.html`.

[7] Manasseh, C. O. Analysis of oil price oscillations, exchange rate dynamics and economic performance. **2019**,

[8] Institute for Energy Research, Cost of Transitioning to 100-Percent Renewable Energy. 2019; `https://www.instituteforenergyresearch.org/renewable/cost-of-transitioning-to-100-percent-renewable-energy/`.

[9] Droege, P. *Urban Energy Transition: From Fossil Fuels to Renewable Power*, 1st ed.; Elsevier Science, 2008.

[10] Canada's Oil and Natural Gas Producers, Uses For Oil. 2020; `https://www.capp.ca/oil/uses-for-oil/`.

[11] Green, G. P., Don W.; Willhite *Enhanced oil recovery*, second edition ed.; SPE International textbook series; Society of Petroleum Engineers, 2018.

[12] Bensimon, K. L. P. L. S. S. B. I. . T. C., D. Viscous flows in two dimensions. *Reviews of Modern Physics* **1986**, *58*, 977–999.

[13] Ruspini, L. C. Experimental and numerical investigation on two-phase flow instabilities. **2013**,

[14] Guillen, C. M. S. . A. V., V. R. Pore scale and macroscopic displacement mechanisms in emulsion flooding. *Transport in Porous Media* **2012**, *94*, 197–206.

[15] Than, P.; Rosso, F.; Joseph, D. Instability of Poiseuille flow of two immiscible liquids with different viscosities in a channel. *International journal of engineering science* **1987**, *25*, 189–204.

[16] Al-Housseiny, T. T.; Tsai, P. A.; Stone, H. A. Control of interfacial instabilities using flow geometry. *Nature Physics* **2012**, *8*, 747–750.

[17] Gao, T.; Mirzadeh, M.; Bai, P.; Conforti, K. M.; Bazant, M. Z. Active control of viscous fingering using electric fields. *Nature communications* **2019**, *10*, 1–8.

[18] Rabbani, H. S.; Or, D.; Liu, Y.; Lai, C.-Y.; Lu, N. B.; Datta, S. S.; Stone, H. A.; Shokri, N. Suppressing viscous fingering in structured porous media. *Proceedings of the National Academy of Sciences* **2018**, *115*, 4833–4838.

[19] Saffman, P. G.; Taylor, G. I. The penetration of a fluid into a porous medium or Hele-Shaw cell containing a more viscous liquid. *Proceedings of the Royal Society of London. Series A. Mathematical and Physical Sciences* **1958**, *245*, 312–329.

[20] McLean, J.; Saffman, P. The effect of surface tension on the shape of fingers in a Hele Shaw cell. *Journal of Fluid Mechanics* **1981**, *102*, 455–469.

[21] Awad, M. *Two-phase flow*; InTech Rijeka, Croatia, 2012.

[22] Wade, L. G. *Organic Chemistry*, 9th ed.; Pearson, 2016.

[23] Zhang, D.; Montanés, F.; Srinivas, K.; Fornari, T.; Ibánez, E.; King, J. W. Measurement and correlation of the solubility of carbohydrates in subcritical water. *Industrial & engineering chemistry research* **2010**, *49*, 6691–6698.

[24] Verma, M. K. *Fundamentals of carbon dioxide-enhanced oil recovery (CO2-EOR): A supporting document of the assessment methodology for hydrocarbon recovery using CO2-EOR associated with carbon sequestration*; US Department of the Interior, US Geological Survey Washington, DC, 2015.

[25] Molnar, P. Rayleigh-Taylor and Convective Instability of Mantle Lithosphere. 2015; `https://cires1.colorado.edu/science/groups/molnar/projects/rayleightaylor/`.

[26] Blunt, M. J. *Multiphase flow in permeable media: A pore-scale perspective*; Cambridge University Press, 2017.

[27] Brennen, C. Fundamentals of multiphase flow. **2005**,

[28] Xahuentitla P., Arturo et. al, Comportamiento de la tensión superficial en la interfase agua-aceite y su influencia sobre la estabilidad de emulsiones. B.S. thesis, 2015.

[29] Constantino de llano, *Fisica*; Editorial Progreso S.A., 2007.

[30] Teh, S.-Y.; Lin, R.; Hung, L.-H.; Lee, A. P. Droplet microfluidics. *Lab on a Chip* **2008**, *8*, 198–220.

[31] Levanichev, V. Study of multi-layer flow in coextrusion processes. *Teka Komisji Motoryzacji i Energetyki Rolnictwa* **2014**, *14*.

[32] Homsy, G. M. Viscous fingering in porous media. *Annual review of fluid mechanics* **1987**, *19*, 271–311.

[33] Wool, R. P. In *Bio-Based Polymers and Composites*; Wool, R. P., Sun, X. S., Eds.; Academic Press: Burlington, 2005; pp 448–482.

[34] Dullien, F. A. *Porous media: fluid transport and pore structure*; Academic press, 2012.

[35] Zhang, Z.-X. In *Rock Fracture and Blasting*; Zhang, Z.-X., Ed.; Butterworth-Heinemann, 2016; pp 111–133.

[36] Guan, X.; Pitchumani, R. Viscous fingering in a Hele-Shaw cell with finite viscosity ratio and interfacial tension. *J. Fluids Eng.* **2003**, *125*, 354–364.

[37] Liang, S. Random-walk simulations of flow in Hele Shaw cells. *Physical Review A* **1986**, *33*, 2663.

[38] Schön, J. H. *Developments in Petroleum Science*; Elsevier, 2015; Vol. 65; pp 21–84.

[39] Kantzas, A.; Bryan, J.; Taheri, S. Fundamentals of fluid flow in porous media. *Pore size distribution* **2012**,

[40] J. Valenzuela, E. Saletan, *Classical dynamics. A contemporary approach*, first edition ed.; Cambridge University Press, 1998.

[41] Højgaard Jensen, J. Introducing fluid dynamics using dimensional analysis. *American Journal of Physics* **2013**, *81*, 688–694.

[42] Lemons, D. *A Student's Guide to Dimensional Analysis*, illustrated ed.; Student's Guides; Cambridge University Press, 2017.

[43] White, F. M. Lecture notes in Bukingham Pi theorem in dimensional analysis. 2020.

[44] Tabeling, P.; Zocchi, G.; Libchaber, A. An experimental study of the Saffman-Taylor instability. *Journal of Fluid Mechanics* **1987**, *177*, 67–82.

[45] Wijnen, B.; Hunt, E. J.; Anzalone, G. C.; Pearce, J. M. Open-source syringe pump library. *PloS one* **2014**, *9*.

[46] Guillen, V.; Carvalho, M.; Alvarado, V. Pore scale and macroscopic displacement mechanisms in emulsion flooding. *Transport in Porous Media* **2012**, *94*, 197–206.

[47] Khan Academy, What is volume flow rate? `https://www.khanacademy.org/science/physics/fluids/fluid-dynamics/a/what-is-volume-flow-rate`.

[48] Soares, C. In *Gas Turbines (Second Edition)*, second edition ed.; Soares, C., Ed.; Butterworth-Heinemann: Oxford, 2015; pp 317–411.

[49] Van Velzen, D.; Lopes Cardozo, R.; Langenkamp, H. Liquid Viscosity and Chemical Constitution of Organic Compounds: A New Correlation and a Compilation of Literature Data. EUR 4735. **1972**,

[50] Amalie Imperial Turbo Formula Engine Oil data sheet. Amalie Oil Co., 2020; 05-01-20 edition.

[51] Gulf TEC Plus data sheet. Gulf Oil International, 2015; May 2015 edition.

[52] Mineev-Weinstein, M. Selection of the Saffman-Taylor finger width in the absence of surface tension: an exact result. *Physical review letters* **1998**, *80*, 2113.

[53] COMSOL INC., The COMSOL Software Product Suite. `https://www.comsol.com/products`, Accessed: 2021-02-19.

[54] Introduction to CFD Module. version Version COMSOL 5.6, COMSOL INC.

[55] COMSOL INC., Building the mesh for a model geometry in COMSOL Multiphysics. 2020; `https://www.comsol.com/video/building-the-mesh-for-a-model-geometry-in-comsol-multiphysics`.

[56] COMSOL INC., Introduction to COMSOL Multiphysics. 2020; `https://doc.comsol.com/5.6/docserver/#!/com.comsol.help.comsol/helpdesk/helpdesk.html`.

[57] CFD Module Users Guide. version Version COMSOL 5.6, COMSOL INC.

[58] Lindberg, V. Uncertainties and Error Propagation Part I of a manual on Uncertainties, Graph-
     ing, and the Vernier Caliper. 2000; `https://www.geol.lsu.edu/jlorenzo/geophysics/`
     `uncertainties/Uncertaintiespart2.html`.